

1983

An Interferometric Study Of Coupled Convective Heat Transfer In A Horizontal Flat Plate Enclosure

Noori Nick Saidi

Follow this and additional works at: <https://ir.lib.uwo.ca/digitizedtheses>

Recommended Citation

Saidi, Noori Nick, "An Interferometric Study Of Coupled Convective Heat Transfer In A Horizontal Flat Plate Enclosure" (1983). *Digitized Theses*. 1254.
<https://ir.lib.uwo.ca/digitizedtheses/1254>

This Dissertation is brought to you for free and open access by the Digitized Special Collections at Scholarship@Western. It has been accepted for inclusion in Digitized Theses by an authorized administrator of Scholarship@Western. For more information, please contact tadam@uwo.ca, wlsadmin@uwo.ca.

The author of this thesis has granted The University of Western Ontario a non-exclusive license to reproduce and distribute copies of this thesis to users of Western Libraries. Copyright remains with the author.

Electronic theses and dissertations available in The University of Western Ontario's institutional repository (Scholarship@Western) are solely for the purpose of private study and research. They may not be copied or reproduced, except as permitted by copyright laws, without written authority of the copyright owner. Any commercial use or publication is strictly prohibited.

The original copyright license attesting to these terms and signed by the author of this thesis may be found in the original print version of the thesis, held by Western Libraries.

The thesis approval page signed by the examining committee may also be found in the original print version of the thesis held in Western Libraries.

Please contact Western Libraries for further information:

E-mail: libadmin@uwo.ca

Telephone: (519) 661-2111 Ext. 84796

Web site: <http://www.lib.uwo.ca/>

CANADIAN THESES ON MICROFICHE

I.S.B.N.

THÈSES CANADIENNES SUR MICROFICHE



National Library of Canada
Collections Development Branch

Canadian Theses on
Microfiche Service

Ottawa, Canada
K1A 0N4

Bibliothèque nationale du Canada
Direction du développement des collections

Service des thèses canadiennes
sur microfiche

NOTICE

The quality of this microfiche is heavily dependent upon the quality of the original thesis submitted for microfilming. Every effort has been made to ensure the highest quality of reproduction possible.

If pages are missing, contact the university which granted the degree.

Some pages may have indistinct print especially if the original pages were typed with a poor typewriter ribbon or if the university sent us a poor photocopy.

Previously copyrighted materials (journal articles, published tests, etc.) are not filmed.

Reproduction in full or in part of this film is governed by the Canadian Copyright Act, R.S.C. 1970, c. C-30. Please read the authorization forms which accompany this thesis.

**THIS DISSERTATION
HAS BEEN MICROFILMED
EXACTLY AS RECEIVED**

AVIS

La qualité de cette microfiche dépend grandement de la qualité de la thèse soumise au microfilmage. Nous avons tout fait pour assurer une qualité supérieure de reproduction.

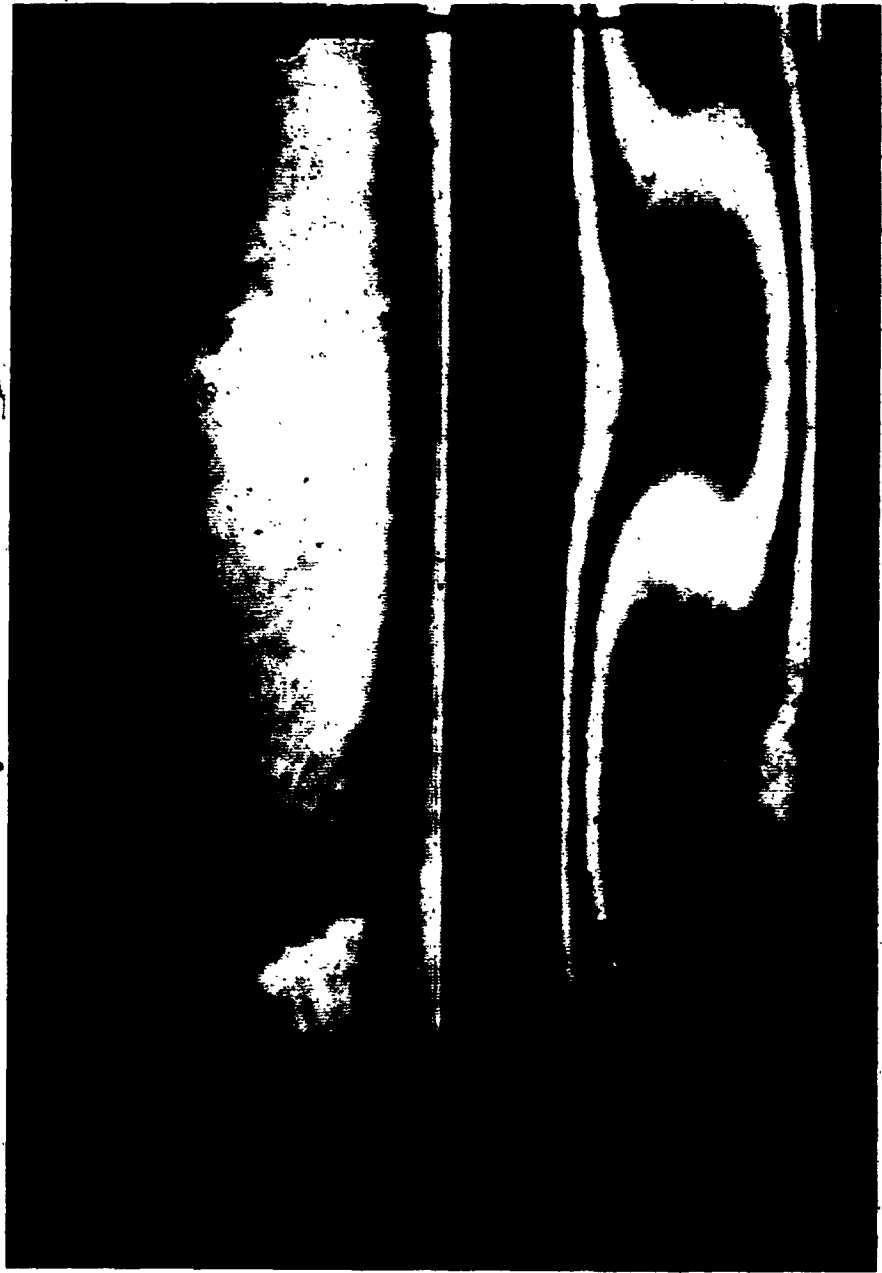
S'il manque des pages, veuillez communiquer avec l'université qui a conféré le grade.

La qualité d'impression de certaines pages peut laisser à désirer, surtout si les pages originales ont été dactylographiées à l'aide d'un ruban usé ou si l'université nous a fait parvenir une photocopie de mauvaise qualité.

Les documents qui font déjà l'objet d'un droit d'auteur (articles de revue, examens publiés, etc.) ne sont pas microfilmés.

La reproduction, même partielle, de ce microfilm est soumise à la Loi canadienne sur le droit d'auteur, SRC 1970, c. C-30. Veuillez prendre connaissance des formules d'autorisation qui accompagnent cette thèse.

**LA THÈSE A ÉTÉ
MICROFILMÉE TELLE QUE
NOUS L'AVONS REÇUE**



AN INTERFEROMETRIC STUDY OF COUPLED
CONVECTIVE HEAT TRANSFER IN A HORIZONTAL
FLAT PLATE ENCLOSURE

by

Noori N. Saidi

Faculty of Engineering Science

Submitted in partial fulfillment
of the requirements for the degree of
Doctor of Philosophy

1

Faculty of Graduate Studies
The University of Western Ontario
London, Ontario
January, 1983

© Noori N. Saidi 1983

ABSTRACT

A long path Mach-Zehnder interferometer was combined with a low speed wind tunnel in order to study the coupling effect between natural heat convection inside the enclosure of a simulated solar collector and external natural and forced convection. This technique permitted qualitative as well as quantitative temperature field visualization of the fluid layers within the enclosure between the hot bottom plate and cold top plate boundaries of the collector, and the coupling effect of natural and forced convection on the cold plate.

The horizontal rectangular enclosure of the simulated solar collector was heated isothermally at the bottom surface and cooled at the top surface. Both plates had a dimension of 45.72 cm by 44.96 cm, and the height of the enclosure was adjustable.

Horizontal and vertical temperature profiles, as well as local and overall heat transfer coefficients were determined for Reynolds number from 0.0 to 6.6×10^4 , Rayleigh number from 10^3 to 4.0×10^5 , and aspect ratio (length/height) from 8.85 to 35.46.

A technique was developed by which finite and infinite fringe field interferograms with the same

boundary conditions could be produced on the same film negative. The finite fringe field interferogram made possible the calculation of the temperature fields, while the isotherm patterns of the infinite fringe field interferograms allowed the study of convective heat transfer, the vertical structure of the convection cell and the circulation pattern.

For low Rayleigh number in the enclosure ($Ra < 1717$) conduction was the predominant mode of heat transfer. As Rayleigh number was increased, the Bénard cell height - to - width ratio was decreased. This increase in Rayleigh number resulted in an observation of convection heat transfer in the central region and conduction heat transfer near the horizontal boundaries. A reversal of the temperature profile occurred for $Ra > 12,000$.

The heat transfer coefficient in the enclosure was found to be strongly dependent on the heating rate and the Rayleigh number, and moderately dependent on the external forced convection. The magnitudes of the local and average Nusselt numbers near the horizontal boundaries in the enclosure were determined, and the results presented in the form of heat transfer correlations for natural convection within the enclosure and external forced convection. These results were found to have close agreement with those of previous investigators.

ACKNOWLEDGEMENTS

I wish to express my deepest gratitude to my advisors, Professor J.D. Tarasuk and Professor T.E. Base, for their continued guidance and encouragement throughout the entire course of this project. Their willingness to discuss any problem at any moment is greatly appreciated.

I am also indebted to Professor P.J. Sullivan for offering guidance during the early part of this study, to Dr. E. Roumi for statistical analysis and to my fellow graduate students Dr. John McKeen and Hani Alnakeeb for their help and friendship.

I am grateful to Dean Chess and the Engineering Faculty for the guidance and the financial support of this project.

I am also grateful to Ms. Joanne Lemon for her meticulous typing of the thesis.

Finally, I wish to thank my parents, my brother Dr. M. Bahadori and my family for their constant encouragement and support. Above all, thanks are due to my wife and my two sons, whose sacrifices made the completion of this thesis possible. It is to my father that this thesis is dedicated, whose constant dedication and encouragement initiated the program.

DEDICATION

TO MY FATHER

FOR HIS FAMILY DEDICATION AND ENCOURAGEMENT

TABLE OF CONTENTS

	Page
CERTIFICATE OF EXAMINATION.....	i
ABSTRACT.....	iii
ACKNOWLEDGEMENTS.....	v
DEDICATION.....	vi
TABLE OF CONTENTS.....	viii
LIST OF TABLES.....	ix
LIST OF FIGURES.....	x
NOMENCLATURE.....	xiv
CHAPTER I - GENERAL REVIEW.....	
1.1 Introduction.....	1
1.2 The Scope of This Study.....	4
CHAPTER II - THE GOVERNING MATHEMATICAL EQUATIONS.....	
2.1 The Governing Mathematical Equations In the Enclosure.....	10
2.2 The Governing Mathematical Equations For the Flow Over the Glazing Plate..	17
CHAPTER III - LITERATURE SURVEY ON CONVECTIVE HEAT TRANSFER APPLIED TO SOLAR COLLECTOR..	
3.1 Introduction.....	26
3.1.1 Concept of Thermal Instability.....	27
3.2 Theoretical Studies of Benard Cells..	28
3.2.1 Experimental Studies of Benard Cells.....	32
3.3 Inclined and Horizontal Fluid Layers - Studies Related to Solar Collector.	38
3.4 Forced Convection On the Glazing of Solar Collector.....	44
CHAPTER IV - LONG PATH DIFFERENCE INTERFEROMETER..	
4.1 Introduction.....	50
4.2 Long Path Difference Mach-Zehnder Interferometer.....	51
CHAPTER V - EXPERIMENTAL APPARATUS.....	59
5.1 Introduction.....	59
5.2 Wind Tunnel Description.....	62
5.2.1 Velocity Distribution Measurement In the Wind Tunnel Test Section....	67
5.3 Long Path Mach-Zehnder Difference Interferometer.....	71
5.4 Design and Construction of the Model.	73
5.4.1 Hot Plate Assembly.....	77
5.4.2 Cold Plate Assembly.....	79

	Page
CHAPTER VI - EXPERIMENTAL METHODS AND PROCEDURES..	
6.1 Operating Procedure and Measurements.	81
6.1.1 The Wind Tunnel.....	81
6.1.2 The Interferometer Alignment.....	83
6.1.3 Positioning the Test Model.....	87
6.2 Data Recording Procedures.....	89
CHAPTER VII- PRESENTATION AND DISCUSSION OF EXPERIMENTAL RESULTS.....	
7.1 Introduction.....	95
7.2 Cellular Convective Motion - Benard Cells.....	97
7.2.1 Non-Dimensional Temperature Profile for the Benard Cell.....	105
7.3 Heat Transfer by Natural Convection In the Entire Enclosure:.....	113
7.3.1 Conduction Regime.....	113
7.3.2 Convection Regime.....	120
7.3.3 Cavity Data Correlation.....	135
7.4 Forced Convection On the Surface of Glazing Plate.....	139
7.4.1 Forced Convection Data Correlation.....	141
CHAPTER VIII- CONCLUSIONS AND RECOMMENDATIONS.....	144
REFERENCES.....	
APPENDIX A - AIR PROPERTIES.....	150
APPENDIX B - INTERFEROGRAM ANALYSIS.....	153
APPENDIX C - DATA REDUCTION.....	186
APPENDIX D - SAMPLE CALCULATIONS.....	189
APPENDIX E - EXPERIMENTAL ERRORS.....	194
REFERENCES.....	198
VITA.....	208

LIST OF TABLES

Table	Description	Page
3.1	Experimental Correlations (Bernard Cells).....	40
3.2	Existing Correlations for Horizontal and Tilted Collector Models.....	42
3.3	Wind Related Heat Losses Correlations....	49
5.1	Hourly Wind Statistics for Diurnal Variation by Month, Based on 26.01 Years of Data.....	63
7.1	Range of Nominal Values of Parameters....	96

LIST OF FIGURES

Figure	Description	Page
1.1	Forced Convection Over a Flat Plate.....	5
1.2	Natural Convection in a Cavity.....	5
1.3	Two-Dimensional Schematic of the Model:..	5
2.1	Two-Dimensional Schematic of the Model...	18
4.1	The Long Path Mach-Zehnder Interferometer Integrated With the Wind Tunnel....	53
4.2	Interferograms With Infinite Fringe Fields; AR=17.7, Re=63350, Ra=8300, $T_{HC}=30.1^{\circ}C$, $T_{CB}=29.9^{\circ}C$	
4.3	Interferograms With Finite Fringe Fields; AR=17.7, Re=63350, Ra=8300, $T_{HC}=30.1^{\circ}C$, $T_{CB}=29.9^{\circ}C$	55
5.1	Wind Streamlines Passing Over Buildings..	60
5.2	Stages in the Development of Flow (From Rest) Past a Model of a House (After Nokkentved, 1932).....	61
5.3	Modified Schematic Diagram of the Wind Tunnel and the Model.....	66
5.4	Multiple Tap Rake.....	68
5.5	Pressure Tubes for the Rake.....	68
5.6	Contour Plot of Typical Velocity Distribution Within the Wind Tunnel.....	70
5.7	Experimental Layout.....	72
5.8	Two-Dimensional Schematic Diagram of the Model.....	75
5.9	The Model With Adjustable Supporting Legs.....	75
5.10	Exploded View of the Hot Plate.....	78

Figure	Description	Page
5.11	Exploded View of the Cold Plate.....	
6.1	Temperature Distributions in the Hot Plate.....	
6.2	The Average Cold Plate Temperature Drop Profile for the Top of the Cold Plate Due to Forced Convection Thermal Boundary Layer Effect.....	
6.3	The Average Cold Plate Temperature Drop Profile for the Bottom of the Cold Plate Due to Forced Convection Thermal Boundary Layer Effect.....	
7.1	Two-Dimensional Convective Current Interferogram (Benard Cell); AR=35.4, Re=0, Ra=2167.....	
7.2	Sequence of Interferograms With Finite Fringes for Analysis, and Infinite Fringes Showing Isotherms in the Test Section; for a & b Re=0, Ra=0; for c & d Re=0, Ra=1390; for e & f Re=50680, Ra=1543.....	
7.3	Sequence of Interferograms With Finite Fringes for Analysis, and Infinite Fringes Showing Isotherms in the Test Section; for a & b Re=0, Ra=1882; for c & d Re=0, Ra=2167; for e & f Re=0, Ra=2676.....	
7.4	Sequence of Interferograms With Finite Fringes for Analysis, and Infinite Fringes Showing Isotherms in the Test Section; for a & b Re=0, Ra=3521; for c & d Re=32709, Ra=4332; for e & f Re=65054, Ra=23789.....	
7.5	Experimental Vertical Temperature Profile in the Cavity; AR=35.4, Re=0, Ra=1390....	
7.6	Experimental Vertical Temperature Profile in the Cavity; AR=35.4, Re=0, Ra=1882....	

Figure	Description	Page
7.7	Experimental Vertical Temperature Profile in the Cavity; AR=35.4, Re=32709, Ra=4332.....	109
7.8	Experimental Vertical Temperature Profile in the Cavity; AR=23.6, Re=0, Ra=12786....	110
7.9	Experimental Vertical Temperature Profile in the Cavity, Showing Upflow, Mid-Cell & Downflow in a Benard Cell, As Well As Temperature Gradients At Hot And Cold Walls; AR=35.4, Re=0, Ra=4367.....	111
7.10	Determination of the Critical Rayleigh Number.....	114
7.11	Finite Interferograms Illustrating the Conduction Regime; AR=35.4, Re=17600, Ra=1100, THC=30.2°C, TCB=24.0°C.....	116
7.12	Experimental Vertical Temperature Profile in the Cavity; AR=35.4, Re=17600, Ra=1100.....	117
7.13	Experimental Horizontal Temperature Profile in the Cavity; AR=35.4, Re=17660, Ra=1100.....	119
7.14	Local Characteristic of Nusselt Number; AR=35.4, Re=17660, Ra=1100.....	121
7.15	Infinite Fringe Interferograms for Free Convection; AR=17.7, Re=0.0, Raave=8357, THCave=30.24, TCBave=24.41....	122
7.16	Finite Fringe Interferograms for Free Convection; AR=17.7, Re=0.0, Raave=8357, THCave=30.24, TCBave=24.41....	123
7.17	Infinite Fringe Interferograms for Forced Convection; AR=17.7, Reave=16973, Raave=9103, THCave=30.15, TCBave=23.83....	125
7.18	Finite Fringe Interferograms for Forced Convection; AR=17.7, Reave=16973, Raave=9103, THCave=30.15, TCBave=23.83....	126

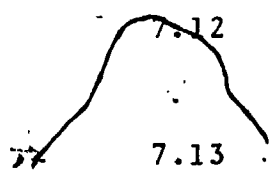


Figure	Description	Page
7.19	Experimental Vertical Temperature Profile in the Cavity; AR=17.7, Re=0.0, Ra=8357..	127
7.20	Experimental Vertical Temperature Profile in the Cavity; AR=17.7, Re=17700, Ra=9100.....	128
7.21	Experimental Horizontal Temperature Profile in the Cavity; AR=35.4, Re=37000; Ra=4800.....	130
7.22	Plot of Isotherms in the Cavity.....	131
7.23	Cavity Nusselt Number as a Function of Distance; AR=35.4, Re=50000, Ra=4050.....	132
7.24	Infinite Fringe Interferograms for Forced Convection; AR=11.8, Re _{ave} =17701, Ra _{ave} =75560, THC _{ave} =50.33, TCB _{ave} =31.47..	133
7.25	Finite Fringe Interferograms.....	134
7.26	Experimental Vertical Temperature Profile; AR=11.8, Re=17700, Ra=75560.....	136
7.27	Experimental Horizontal Temperature Profile; AR=11.8, Re=17700, Ra=75560.....	137
7.28	Local Characteristic of Nusselt Number; AR=11.8, Re=17700, Ra=75560.....	138
7.29	Comparison of Previous Correlations With the Result of the Present Investigation..	140
7.30	Plot of Reynolds Number as a Function of Heat Transfer Coefficient.....	143

NOMENCLATURE

A	=	surface area of plate
AR	=	aspect ratio (H/L)
A, B, C, D, E	=	constants used in polynomial expression for average temperature profile in Appendix D
C_p	=	specific heat at constant pressure
d	=	thickness of glazing plate
F	=	body forces
F_{SH}	=	fringe shift
g	=	gravitational acceleration
G	=	Gladstone-Dale constant
Gr	=	Grashof number
H	=	plate length
h	=	local heat transfer coefficient
\bar{h}	=	average heat transfer coefficient
K	=	thermal conductivity of air
L	=	plate separation
L_c	=	characteristic length
n	=	refractive index
Nu	=	local Nusselt number (hL/K)
\bar{Nu}	=	average Nusselt number ($\bar{h}L/K$)
P	=	circumference of plate
p	=	pressure
Pr	=	Prandtl number ($\mu C_p/K$)
q'	=	local heat flux

Ra, RA = Rayleigh number
 Re, RE = Reynolds number
 ΔS = difference between two optical path lengths
 t = time
 T = temperature
 T' = temperature inside boundary layer
 U = velocity in x-direction
 U' = velocity in x-direction inside boundary layer
 V = velocity in y-direction
 W = velocity in z-direction
 x = coordinate along plate length H
 y = coordinate along plate separation L
 z = coordinate along plate width
 α = thermal diffusivity
 β = coefficient of volumetric expansion
 δ = momentum boundary layer thickness
 δ_T = thermal boundary layer thickness
 ΔT = temperature difference between plates
 θ = non-dimensional temperature $\left(\frac{T-T_{CB}}{T_H-T_{CB}}\right)$
 λ = wavelength of light source
 μ = dynamic viscosity
 ν = kinematic viscosity
 ρ = density
 ϕ = angle of tilt of solar collector with respect to the horizontal

ψ = stream function

Subscripts

CB = bottom of cold plate

CT = top of cold plate

H = hot plate

L = based on length L

W = based on wind speed

∞ = based on wind tunnel speed

CHAPTER I

GENERAL REVIEW

1.1 INTRODUCTION

Convective heat transfer phenomena have captured the attention of scientists for more than a century. Meteorologists for years have been concerned with the effects of the buoyancy forces when adverse stratified horizontal layers of air play a dominant role in determining the atmospheric conditions. At one time, meteorologists believed that even a small temperature difference would initiate an unstable convective motion to alter the atmospheric conditions. It has now been shown theoretically, as well as experimentally, that the air or the fluid can indeed remain stationary until the temperature difference between the top and bottom layers of air exceeds a critical value. Beyond this critical value convective motion starts due to the buoyancy forces becoming greater than the viscous forces. The point at which this instability occurs depends on the fluid properties, the temperature difference between the top and bottom layers and the thickness of the air layers.

In the past few decades, engineers have been concerned with practical aspects of free and forced convection. Understanding of these phenomena is necessary

2

for estimating the transfer of heat in various heat exchangers and heating or cooling of structures. There are many practical problems in which convective heat transfer is important. Examples are: air layers within the building insulation, in the walls of furnaces and heat exchangers, nuclear reactor cores, double or triple glazed windows, skylights and attic space.

With an increased interest in solar energy in recent years, engineers have been particularly concerned with minimizing the convective heat losses of solar collectors to a cooler environment by natural or forced convection. The understanding of thermally induced natural convection of air inside of a cavity of a solar collector, where air is heated from below by an absorber plate and cooled on the glazing plate by combined natural and forced convection, is essential to the designers of solar collectors where interest in performance and efficiency is important. Decisions such as the choice of single, double or triple glazing, the spacing distance between the absorber and the glazing plates, flat or corrugated plates, types of plates and selective or non-selective coatings can maximize the efficiency and thus minimize the size and the cost of solar collectors.

By far, the most important feature of any thermal

convective problem is the recognition that the temperature and the velocity distributions of the fluid or gases involved are coupled. The velocity of the fluid is caused by the buoyancy forces which consequently arise from a temperature variation. Thus, one cannot consider each of the parameters independent of the other. The temperature and the velocity must be considered together. Indeed, this consideration, combined with the nonlinearity of the governing equations for motion and heat transfer of the fluid flow, makes the problem of the thermal convective phenomenon very difficult to solve analytically. Analytical models have been developed for only several special geometries; most studies have been experimental. Regardless of experimental or theoretical approaches, the complexity of the problem dictates that simplifying assumptions must be made with regard to the boundary conditions.

Related studies, both theoretical and experimental, have been presented in this area with the intention of developing correlation equations as "tools" to enable the design engineers to estimate the heat transfer coefficient inside and outside of a solar collector cavity. Most of the investigators, to the author's best knowledge, when studying solar collectors assumed that both the absorber and the glazing surfaces were isothermal. In several studies, found in the literature, some researchers assumed

constant heat flux for the top plate. They also have considered either forced flow over an isothermal plate to calculate the wind related heat losses as shown in Figure 1.1, or flow inside two differentially heated and cooled isothermal plates in a cavity, shown in Figure 1.2. The proposed heat transfer correlations included parameters such as: Reynolds and Prandtl numbers for the forced convection; aspect ratios (H/L), physical properties of the fluid, tilt angle, the temperature difference between the plates and the height of the cavity for the natural convection inside the enclosure.

1.2 THE SCOPE OF THIS STUDY

Solar collectors are usually exposed to unfavorable external conditions. External convective forces on the outside glazing enhance thermal heat losses resulting from the boundary layer effect on the surface of the glazing. The temperature distribution of the glazing plate depends on parameters such as the temperature of the absorber plate, the cavity height, the radiation exchange and the exterior forced convection.

The present investigation, Figure 1.3, is an attempt to combine the above mentioned problems into one; with the intention of better simulating the heat transfer characteristics of a horizontal solar collector. Parameters

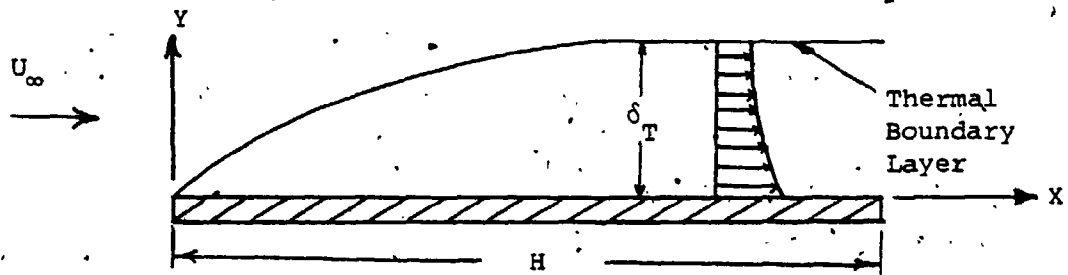


FIGURE 1.1 Forced Convection Over a Flat Plate

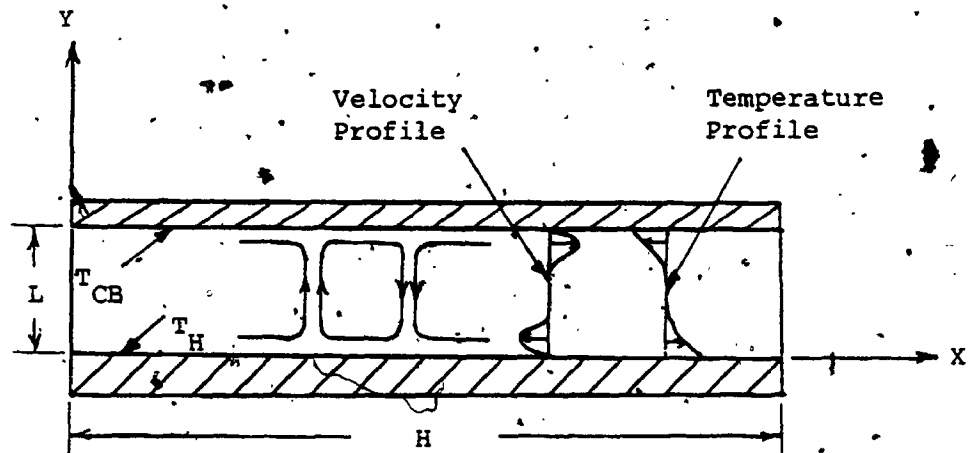


FIGURE 1.2 Natural Convection in a Cavity

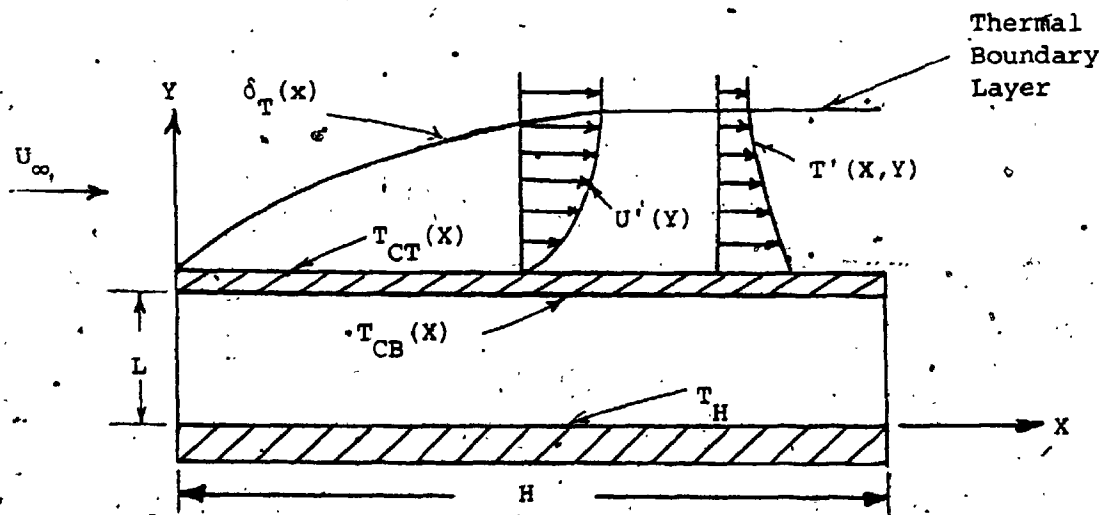


FIGURE 1.3 Two-Dimensional Schematic Diagram of the Model

such as external wind effects, variable glazing temperatures, absorber surface temperatures, and aspect ratios will be considered. Consideration will also be given to the formation of the Beñard cell convective motion inside the cavity.

An experimental method which might achieve these objectives is an interferometric technique combined with a low speed wind tunnel. A model of a solar collector is placed in an open low speed wind tunnel which is integrated with a long path differential Mach-Zehnder interferometer. The interferometer is perpendicularly positioned to the wind tunnel working section which provides a method for qualitative as well as quantitative study of thermal heat transfer, both in the cavity and on the top of the glazing. The unique contribution of this investigation would be the study and comparison of natural convection in the cavity with and without forced cooling convective effects on the top of the glazing.

It is intended that this investigation will encompass:

1. The feasibility of combining an interferometer with a wind tunnel for the study of coupling natural and forced convection heat transfer.

2. The establishment of an easy method for obtaining interferograms with both finite and infinite fringe fields.
3. A better understanding of the formation of Benard cells.
4. The influence of the Rayleigh number on the dimensions of the Benard cells.
5. An examination of the temperature reversal in the horizontal solar cavity.
6. The description of horizontal and vertical temperature profiles in the enclosure.
7. The influence of the aspect ratio on the convective coefficients.
8. A study of the Rayleigh number influence on the convective coefficient as the flow changes from no flow to laminar flow and possibly to turbulent flow conditions.
9. A study of the effect of the thermal boundary layer on the temperature distribution of the cold plate.
10. The calculation of the local and average Nusselt numbers from the temperature profiles.
11. The correlation of the most relevant dimensionless groups affecting the heat convection coefficients in the enclosure.

8

12. The correlation of the most relevant dimensionless groups on the external wind-related heat transfer.

Finally, the proposed model and apparatus presented in this investigation involves two very complex aspects of thermal convective heat transfer problems. One aspect is the coupled thermal heat flow, and the other is the thermal interaction between two isothermal and non-isothermal plates of different temperatures separated by a fluid or gas.

The specific sections for the wind tunnel were designed and constructed to enable the model to be tilted from zero to sixty degrees from the horizontal position. Further investigation for the tilted solar collector model is underway, utilizing the same model and apparatus.

The remainder of this thesis is organized as follows: the governing mathematical equations for free convection in the enclosure and forced convection on the top of the glazing plate are presented in Chapter II. Here emphasis is placed on the necessary boundary conditions to the solution of the governing equation. The pertinent literature survey is discussed in Chapter III. This chapter is divided into three separate sections. First, studies related to the Benard cells, second, studies related to the natural convection in an enclosure, followed by studies

related to the forced convection on the glazing of a flat plate solar collector.

Chapter IV discusses the optical method long path difference interferometer and advantages and disadvantages of finite and infinite fringe fields. A detailed description of the experimental apparatus is presented in Chapter V while the experimental methods and procedures are outlined in Chapter VI. The presentation and discussion of the experimental results are given in Chapter VII. Finally, conclusions and recommendations are set forth in the last chapter, Chapter VIII.

CHAPTER II

THE GOVERNING MATHEMATICAL EQUATIONS

2.1 THE GOVERNING MATHEMATICAL EQUATIONS IN THE ENCLOSURE

In this chapter an attempt will be made to establish a mathematical model which will describe the fluid flow and heat transfer for a fluid element as described in Figure 2.1. Clearly, conservation of mass, momentum and energy must be satisfied. Simplification of the general form of these equations is essential for establishing the dependency of non-dimensional parameters for the rate of convective heat transfer.

Two initial assumptions must be made.

1. The fluid is incompressible and Newtonian.
2. The flow has constant physical and thermal properties except for the temperature effect on the density which produces a buoyancy force. This effect will be considered using the Boussinesque approximation.

The governing equations in three dimensions can be written as follows [1,2]:

Continuity equation:

$$\frac{\partial \rho}{\partial t} + \rho \left(\frac{\partial U}{\partial X} + \frac{\partial V}{\partial Y} + \frac{\partial W}{\partial Z} \right) = 0 \quad (2.1.1)$$

Momentum equations:

X-Component

$$\begin{aligned} \rho \left(\frac{\partial U}{\partial t} + U \frac{\partial U}{\partial X} + V \frac{\partial U}{\partial Y} + W \frac{\partial U}{\partial Z} \right) &= - \frac{\partial P}{\partial X} \\ + F_X + \mu \left(\frac{\partial^2 U}{\partial X^2} + \frac{\partial^2 U}{\partial Y^2} + \frac{\partial^2 U}{\partial Z^2} \right) & \end{aligned} \quad (2.1.2)$$

Y-Component

$$\begin{aligned} \rho \left(\frac{\partial V}{\partial t} + U \frac{\partial V}{\partial X} + V \frac{\partial V}{\partial Y} + W \frac{\partial V}{\partial Z} \right) &= - \frac{\partial P}{\partial Y} \\ + F_Y + \mu \left(\frac{\partial^2 V}{\partial X^2} + \frac{\partial^2 V}{\partial Y^2} + \frac{\partial^2 V}{\partial Z^2} \right) & \end{aligned} \quad (2.1.3)$$

Z-Component

$$\begin{aligned} \rho \left(\frac{\partial W}{\partial t} + U \frac{\partial W}{\partial X} + V \frac{\partial W}{\partial Y} + W \frac{\partial W}{\partial Z} \right) &= - \frac{\partial P}{\partial Z} \\ + F_Z + \mu \left(\frac{\partial^2 W}{\partial X^2} + \frac{\partial^2 W}{\partial Y^2} + \frac{\partial^2 W}{\partial Z^2} \right) & \end{aligned} \quad (2.1.4)$$

Energy equation:

$$\begin{aligned} \rho C_p \left(\frac{\partial T}{\partial t} + U \frac{\partial T}{\partial X} + V \frac{\partial T}{\partial Y} + W \frac{\partial T}{\partial Z} \right) &= K \left(\frac{\partial^2 T}{\partial X^2} + \frac{\partial^2 T}{\partial Y^2} + \frac{\partial^2 T}{\partial Z^2} \right) \\ + 2\mu \left[\left(\frac{\partial U}{\partial X} \right)^2 + \left(\frac{\partial V}{\partial Y} \right)^2 + \left(\frac{\partial W}{\partial Z} \right)^2 \right] \\ + \mu \left[\left(\frac{\partial U}{\partial Y} + \frac{\partial V}{\partial X} \right)^2 + \left(\frac{\partial U}{\partial Z} + \frac{\partial W}{\partial X} \right)^2 + \left(\frac{\partial V}{\partial Z} + \frac{\partial W}{\partial Y} \right)^2 \right] & \end{aligned} \quad (2.1.5)$$

where U , V and W are, respectively; the X , Y and Z components of velocity.

The following simplifying assumptions are further introduced:

1. Viscous heat dissipation is negligible;
2. The flow is two-dimensional;
3. The flow is steady;
4. The pressure changes are moderate, thus compression work is negligible.

Therefore, the equations (2.1.2) to (2.1.5) can be reduced as follows:

Continuity equation becomes:

$$\frac{\partial U}{\partial X} + \frac{\partial V}{\partial Y} = 0 \quad (2.1.6)$$

Momentum equations become:

X -Component

$$\rho \left(U \frac{\partial U}{\partial X} + V \frac{\partial U}{\partial Y} \right) = - \frac{\partial P}{\partial X} + F_X + \mu \left(\frac{\partial^2 U}{\partial X^2} + \frac{\partial^2 U}{\partial Y^2} \right) \quad (2.1.7)$$

Y -Component

$$\rho \left(U \frac{\partial V}{\partial X} + V \frac{\partial V}{\partial Y} \right) = - \frac{\partial P}{\partial Y} + F_Y + \mu \left(\frac{\partial^2 V}{\partial X^2} + \frac{\partial^2 V}{\partial Y^2} \right) \quad (2.1.8)$$

Energy equation becomes:

$$\rho C_p \left(U \frac{\partial T}{\partial X} + V \frac{\partial T}{\partial Y} \right) = K \left(\frac{\partial^2 T}{\partial X^2} + \frac{\partial^2 T}{\partial Y^2} \right) \quad (2.1.9)$$

The variation of density due to temperature can be expressed by Taylor series about a reference temperature T_0 . Neglecting the higher terms we have

$$\rho = \rho_0 + \left(\frac{\partial \rho}{\partial T}\right)_P (T - T_0) + \dots \quad (2.1.10)$$

But, by definition

$$\left(\frac{\partial \rho}{\partial T}\right)_P = -\rho \beta \quad (2.1.11)$$

where β is the coefficient of volumetric expansion. By substituting Eq. 2.1.11 into Eq. 2.1.10 we obtain

$$\rho = \rho_0 - \rho \beta (T - T_0) \quad (2.1.12)$$

The body forces can be written as follows:

$$F_X = 0 \quad (2.1.13)$$

$$F_Y = -\rho g \quad (2.1.14)$$

$$F_Z = 0 \quad (2.1.15)$$

Substitution of Eq. 2.1.12 into Eq. 2.1.14 yields

$$F_Y = -\rho g + \rho_0 g \beta (T - T_0) \quad (2.1.16)$$

By taking the temperature of the bottom of the cold plate T_{CB} , as reference temperature and substituting Eqs. 2.1.13, 2.1.15 and 2.1.16 into the momentum equations (2.1.7) and (2.1.8) we have:

$$\rho \left(U \frac{\partial U}{\partial X} + V \frac{\partial U}{\partial Y} \right) = - \frac{\partial P}{\partial X} + \mu \left(\frac{\partial^2 U}{\partial X^2} + \frac{\partial^2 U}{\partial Y^2} \right) \quad (2.1.17)$$

$$\rho \left(V \frac{\partial V}{\partial X} + V \frac{\partial V}{\partial Y} \right) = - \frac{\partial P}{\partial Y} - \rho_0 g + \rho g \beta (T - T_{CB}) + \mu \left(\frac{\partial^2 V}{\partial X^2} + \frac{\partial^2 V}{\partial Y^2} \right) \quad (2.1.18)$$

Since constant properties were assumed, the choice of the reference temperature becomes arbitrary. A convenient choice is the bottom of the cold plate temperature T_{CB} . A combined pressure term can be introduced as

$$P' = P + \rho_0 g Y \quad (2.1.19)$$

By differentiating Eq. 2.1.19 with respect to X and Y, the governing equations can be written as:

Continuity equations:

$$\frac{\partial U}{\partial X} + \frac{\partial V}{\partial Y} = 0 \quad (2.1.20)$$

Momentum equations:

X-Component:

$$\rho \left(U \frac{\partial U}{\partial X} + V \frac{\partial U}{\partial Y} \right) = - \frac{\partial P'}{\partial X} + \mu \left(\frac{\partial^2 U}{\partial X^2} + \frac{\partial^2 U}{\partial Y^2} \right) \quad (2.1.21)$$

Y-Component:

$$\rho \left(U \frac{\partial V}{\partial X} + V \frac{\partial V}{\partial Y} \right) = - \frac{\partial P'}{\partial Y} + \rho g \beta (T - T_{CB}) + \mu \left(\frac{\partial^2 V}{\partial X^2} + \frac{\partial^2 V}{\partial Y^2} \right) \quad (2.1.22)$$

Energy equation:

$$\rho C_P \left(U \frac{\partial T}{\partial X} + V \frac{\partial T}{\partial Y} \right) = K \left(\frac{\partial^2 T}{\partial X^2} + \frac{\partial^2 T}{\partial Y^2} \right) \quad (2.1.23)$$

The governing differential equations (2.1.20) to (2.1.23) can be made non-dimensional by letting

$$X^* = \frac{X}{L} \quad \therefore \quad Y^* = \frac{Y}{L}$$

$$U^* = \frac{\rho U C_P L}{K} \quad \therefore \quad V^* = \frac{\rho V C_P L}{K} \quad (2.1.24)$$

$$\theta = \frac{T - T_{CB}}{T_H - T_{CB}} \quad \therefore \quad P^* = \frac{\rho L^2 C_P P}{\mu K}$$

By substituting Eqs. 2.1.24 into Eqs. 2.1.20 to 2.1.23, the governing non-dimensional differential equation can be written as:

Continuity equation becomes

$$\frac{\partial U^*}{\partial X^*} + \frac{\partial V^*}{\partial Y^*} = 0 \quad (2.1.25)$$

Momentum equations become

X-Direction

$$U^* \frac{\partial U^*}{\partial X^*} + V^* \frac{\partial U^*}{\partial Y^*} = -Pr \frac{\partial P^*}{\partial X^*} + Pr \left(\frac{\partial^2 U^*}{\partial X^{*2}} + \frac{\partial^2 U^*}{\partial Y^{*2}} \right) \quad (2.1.26)$$

Y-Direction

$$U^* \frac{\partial V^*}{\partial X^*} + V^* \frac{\partial V^*}{\partial Y^*} = -Pr \frac{\partial P^*}{\partial Y^*} + Ra_L Pr (T - T_{CB})$$

$$+ Pr \left(\frac{\partial^2 V^*}{\partial X^{*2}} + \frac{\partial^2 V^*}{\partial Y^{*2}} \right) \quad (2.1.27)$$

Energy equation becomes

$$U^* \frac{\partial \theta}{\partial X^*} + V^* \frac{\partial \theta}{\partial Y^*} = \frac{1}{\alpha} \left(\frac{\partial^2 \theta}{\partial X^{*2}} + \frac{\partial^2 \theta}{\partial Y^{*2}} \right) \quad (2.1.28)$$

where, $Pr = \frac{C_p \mu}{K}$ is the Prandtl number and

$$Ra_L = Gr \cdot Pr \text{ or}$$

$$Ra_L = \frac{\rho^2 g \beta L^3 (T - T_{CB})}{\mu^2} \cdot \frac{g \mu}{K} \text{ is the Rayleigh number}$$

and $\alpha = \frac{K}{\rho C_p}$ is thermal diffusivity.

The boundary conditions for the cavity are as follows:

1. for $0 \leq X^* \leq \frac{H}{L}$, $Y^* = 0$
 $U^* = V^* = 0$, $\theta = 1$
2. for $0 \leq X^* \leq \frac{H}{L}$, $Y^* = 1$
 $U^* = V^* = 0$, $\theta = \theta(X^*)$
3. for $0 \leq Y^* \leq 1$, $X^* = 0$
 $U^* = V^* = 0$, $\theta = \theta(Y^*)$
4. for $0 \leq Y^* \leq 1$, $X^* = \frac{H}{L}$
 $U^* = V^* = 0$, $\theta = \theta(Y^*)$

where, $AR = \frac{H}{L}$ is the aspect ratio.

The governing differential equations in non-dimensional form indicate that the temperature distribution in the enclosure might be a strong function of Grashof number, Prandtl number and Aspect ratio.

The boundary conditions clearly indicate that an advanced knowledge of the temperature distributions at the vertical walls and the bottom of the glazing plate is needed for solving the problem analytically. To simplify the problem, most researchers have assumed isothermal condition for the lower surface of the glazing plate. In this investigation, the validity of the above approximation will be investigated.

2.2 THE GOVERNING MATHEMATICAL EQUATIONS FOR THE FLOW OVER THE GLAZING PLATE

To formulate the problem for the flow over the glazing plate covering the cavity we consider an element above the glazing plate in the boundary layer, as shown in Figure 2.1. Introducing a new set of coordinates such as

$$X' = X$$

(2.2.1)

$$Y = L + d + Y'$$

where L is the height of the cavity and d is the thickness of the glazing plate. Writing the governing differential equations of Eqs. 2.1.20 to 2.1.23 and using the new set of coordinates, we have that;

Continuity equation becomes:

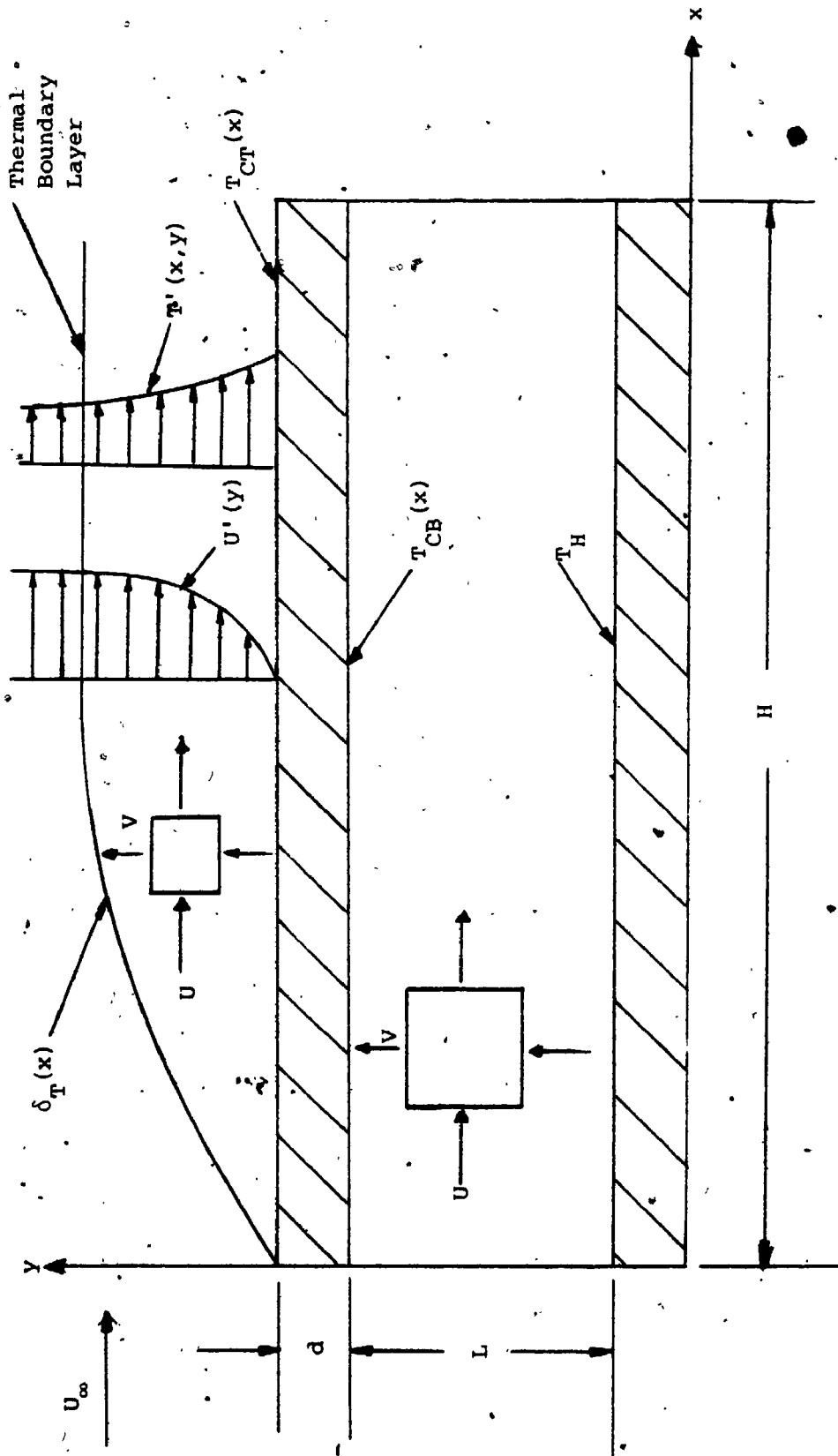


FIGURE 2.1 Two-Dimensional Schematic Diagram of the Model

$$\frac{\partial U'}{\partial X'} + \frac{\partial V'}{\partial Y'} = 0 \quad (2.2.2)$$

Momentum equations become:

X'-Direction:

$$\rho' (U' \frac{\partial U'}{\partial X'} + V' \frac{\partial U'}{\partial Y'}) = - \frac{\partial P'}{\partial X'} + U' (\frac{\partial^2 U'}{\partial X'^2} + \frac{\partial^2 U'}{\partial Y'^2}) \quad (2.2.3)$$

Y'-Direction:

$$\rho' (U' \frac{\partial V'}{\partial X'} + V' \frac{\partial V'}{\partial Y'}) = - \frac{\partial P'}{\partial Y'} + \rho' g \beta (T - T_{\infty}) + \mu' (\frac{\partial^2 V'}{\partial X'^2} + \frac{\partial^2 V'}{\partial Y'^2}) \quad (2.2.4)$$

Energy equation becomes:

$$\rho' C_P (U' \frac{\partial T'}{\partial X'} + V' \frac{\partial T'}{\partial Y'}) = K' (\frac{\partial^2 T'}{\partial X'^2} + \frac{\partial^2 T'}{\partial Y'^2}) \quad (2.2.5)$$

where (') indicates conditions above the glazing plate but inside the boundary layer.

To write the boundary conditions, there are two different cases which must be considered separately.

1. There is no forced flow on top of the glazing plate. Thus, natural convection is the dominant force.
2. There is forced flow on top of the glazing plate. Thus, forced convection plays the dominant role.

1. Boundary Conditions For No Forced Flow Case

$$\text{at } Y' = d+L, U' = V' = 0$$

$$T' = T_{CT}'(X')$$

(2.2.6)

$$\text{at } Y' \rightarrow \infty \quad U' = V' = 0$$

(2.2.7)

$$T' = T_{\infty} \text{ and } P' \rightarrow P_{\infty}$$

By introducing a new set of dimensionless variables

$$\bar{X} = \frac{X'}{L_c} \quad \bar{Y} = \frac{Y'}{L_c}$$

(2.2.8)

$$\bar{U} = \frac{\rho' L_c U'}{\mu' Gr'_{L_c}} \quad \bar{V} = \frac{\rho' L_c V'}{\mu' Gr'_{L_c}}$$

$$\bar{\theta} = \frac{T' - T_{\infty}}{T_{CT} - T_{\infty}} \quad \bar{P} = \frac{\rho' L_c^2 P'}{\mu'^2 Gr'}$$

where T_{CT} is the temperature of the top of the glazing plate, L_c is the characteristic length, defined as four times the area of the glazing plate divided by its wetted perimeter, and Gr'_{L_c} is the Grashof number based on the characteristic length

$$Gr'_{L_c} = \frac{\rho'^2 g \beta (T_{CT} - T_{\infty}) L_c^3}{\mu'^2}$$

By substituting Eq. 2.2.8 into Eqs. 2.2.2 to 2.2.5 it follows:

For the continuity equation:

$$\frac{\partial \bar{U}}{\partial \bar{X}} + \frac{\partial \bar{V}}{\partial \bar{Y}} = 0 \quad (2.2.9)$$

For the momentum equations:

\bar{X} -Direction:

$$\text{Gr}'_{L_c} \left(\bar{U} \frac{\partial \bar{U}}{\partial \bar{X}} + \bar{V} \frac{\partial \bar{U}}{\partial \bar{Y}} \right) = - \frac{\partial \bar{P}}{\partial \bar{X}} + \left(\frac{\partial^2 \bar{U}}{\partial \bar{X}^2} + \frac{\partial^2 \bar{U}}{\partial \bar{Y}^2} \right) \quad (2.2.10)$$

\bar{Y} -Direction

$$\text{Gr}'_{L_c} \left(\bar{U} \frac{\partial \bar{V}}{\partial \bar{X}} + \bar{V} \frac{\partial \bar{V}}{\partial \bar{Y}} \right) = - \frac{\partial \bar{P}}{\partial \bar{Y}} + \bar{\theta} + \left(\frac{\partial^2 \bar{V}}{\partial \bar{X}^2} + \frac{\partial^2 \bar{V}}{\partial \bar{Y}^2} \right) \quad (2.2.11)$$

and for the energy equations:

$$\text{Gr}'_{L_c} \left(\bar{U} \frac{\partial \bar{\theta}}{\partial \bar{X}} + \bar{V} \frac{\partial \bar{\theta}}{\partial \bar{Y}} \right) = \frac{1}{\text{Pr}'} \left(\frac{\partial^2 \bar{\theta}}{\partial \bar{X}^2} + \frac{\partial^2 \bar{\theta}}{\partial \bar{Y}^2} \right) \quad (2.2.12)$$

By defining the stream function as follows:

$$\bar{U} = \frac{\partial \psi}{\partial \bar{Y}} \quad \text{and} \quad \bar{V} = - \frac{\partial \psi}{\partial \bar{X}} \quad (2.2.13)$$

and substituting the stream functions into Eqs. 2.2.9 to 2.2.12, the continuity equation will be immediately satisfied and the governing equations now become

Momentum Equation:

For the X-Direction:

$$\text{Gr}'_{L_c} \left(\frac{\partial \psi}{\partial \bar{Y}} - \frac{\partial^2 \psi}{\partial \bar{X} \partial \bar{Y}} - \frac{\partial \psi}{\partial \bar{X}} \frac{\partial^2 \psi}{\partial \bar{Y}^2} \right) = - \frac{\partial \bar{P}}{\partial \bar{X}} + \left(\frac{\partial^3 \psi}{\partial \bar{X}^2 \partial \bar{Y}} + \frac{\partial^3 \psi}{\partial \bar{Y}^3} \right) \quad (2.2.14)$$

For the Y-Direction:

$$\text{Gr}'_{L_c} \left(- \frac{\partial \psi}{\partial \bar{Y}} \frac{\partial^2 \psi}{\partial \bar{X}^2} + \frac{\partial \psi}{\partial \bar{X}} \frac{\partial^2 \psi}{\partial \bar{X} \partial \bar{Y}} \right) = - \frac{\partial \bar{P}}{\partial \bar{Y}} + \left(\frac{\partial^3 \psi}{\partial \bar{X}^3} + \frac{\partial^3 \psi}{\partial \bar{X} \partial \bar{Y}^2} \right) + \bar{\theta} \quad (2.2.15)$$

Energy Equation:

$$\text{Gr}'_{L_c} \left(\frac{\partial \psi}{\partial Y'} \frac{\partial \bar{\theta}}{\partial X'} - \frac{\partial \psi}{\partial X'} \frac{\partial \bar{\theta}}{\partial Y'} \right) = - \frac{1}{\text{Pr}'} \left(\frac{\partial^2 \bar{\theta}}{\partial X'^2} + \frac{\partial^2 \bar{\theta}}{\partial Y'^2} \right) \quad (2.2.16)$$

These governing equations in non-dimensional form indicate that the temperature distribution above the cavity when there is no forced convection on top of the glazing plate might be strongly a function of the Grashof and the Prandtl numbers.

Again, the information with regard to the boundary condition, Eq. 2.2.6, for the temperature distribution on top of the glazing would be required for the analytical solutions of the governing equations.

2. Boundary Conditions For Forced Flow Case

$$\begin{aligned} \text{at } Y' = 0, \quad U' = V' = 0 \\ \text{and } T' = T_{CT}(X') \end{aligned} \quad (2.2.17)$$

$$\begin{aligned} \text{at } Y' = \infty, \quad U' = U_{\infty}; \quad V' = 0 \\ T' = T^{\infty} \text{ and } P' = P_{\infty} \end{aligned} \quad (2.2.18)$$

If the Reynolds number is assumed to be sufficiently large, the following variables can be introduced according to the boundary layer theory:

$$U' = \frac{U}{U_{\infty}}; \quad V' = \frac{V}{U_{\infty}}; \quad X' = \frac{X}{L_c}; \quad Y' = \frac{Y}{L_c} \text{Re}_L^{1/2}$$

$$X' = \frac{\bar{X}}{L_C} \quad Y' = \frac{\bar{Y} \text{Re}_{L_C}^{1/2}}{L_C} \quad (2.2.19)$$

$$\bar{\theta} = \frac{T' - T_\infty}{T_{CT} - T_\infty} \quad \bar{P} = \frac{P'}{\rho' U_\infty^2}$$

where L_C and T_{CT} are as defined before and the Reynolds number is defined as

$$\text{Re}_{L_C} = \frac{\rho' U_\infty L_C}{\mu'}$$

Thus, by substituting Eq. 2.2.19 into Eqs. 2.2.2 to 2.2.5, the governing equations become:

Continuity:

$$\frac{\partial \bar{U}}{\partial \bar{X}} + \frac{\partial \bar{V}}{\partial \bar{Y}} = 0 \quad (2.2.20)$$

Momentum:

\bar{X} -Direction:

$$\bar{U} \frac{\partial \bar{U}}{\partial \bar{X}} + \bar{V} \frac{\partial \bar{U}}{\partial \bar{Y}} = - \frac{\partial \bar{P}}{\partial \bar{X}} + \left(\frac{1}{\text{Re}_{L_C}} \frac{\partial^2 \bar{U}}{\partial \bar{X}^2} + \frac{\partial^2 \bar{U}}{\partial \bar{Y}^2} \right) \quad (2.2.21)$$

\bar{Y} -Direction:

$$\frac{1}{\text{Re}_{L_C}^{1/2}} (\bar{U} \frac{\partial \bar{U}}{\partial \bar{X}} + \bar{V} \frac{\partial \bar{U}}{\partial \bar{Y}}) = \text{Re}_{L_C}^{1/2} \frac{\partial \bar{P}}{\partial \bar{Y}} + \frac{\text{Gr}'_{L_C}}{\text{Re}_{L_C}^2} \bar{\theta}'$$

$$+ \frac{1}{\text{Re}_{L_C}^{1/2}} \left(\frac{1}{\text{Re}_{L_C}} \frac{\partial^2 \bar{V}}{\partial \bar{X}^2} + \frac{\partial^2 \bar{V}}{\partial \bar{Y}^2} \right) \quad (2.2.22)$$

Energy:

$$\bar{U} \frac{\partial \bar{\theta}}{\partial \bar{X}} + \bar{V} \frac{\partial \bar{\theta}}{\partial \bar{Y}} = \frac{1}{\text{PrRe}_{Lc}} \left(\frac{\partial^2 \bar{\theta}}{\partial \bar{X}^2} + \text{Re}_{Lc} \frac{\partial^2 \bar{\theta}}{\partial \bar{Y}^2} \right) \quad (2.2.23)$$

Applying the stream function as defined earlier

$$\bar{U} = \frac{\partial \psi}{\partial \bar{Y}}, \quad \bar{V} = -\frac{\partial \psi}{\partial \bar{X}}$$

The continuity equation is automatically satisfied and Eqs. 2.2.21 to 2.2.23 now become

Momentum:

\bar{X} -Direction:

$$\left(\frac{\partial \psi}{\partial \bar{Y}} \frac{\partial^2 \psi}{\partial \bar{X} \partial \bar{Y}} - \frac{\partial \psi}{\partial \bar{X}} \frac{\partial^2 \psi}{\partial \bar{Y}^2} \right) = -\frac{\partial \bar{P}}{\partial \bar{X}} + \left(\frac{1}{\text{Re}_{Lc}} \frac{\partial^3 \psi}{\partial \bar{X}^2 \partial \bar{Y}} + \frac{\partial^3 \psi}{\partial \bar{Y}^3} \right) \quad (2.2.24)$$

\bar{Y} -Direction:

$$\begin{aligned} \frac{1}{\text{Re}_{Lc}^{1/2}} \left(-\frac{\partial \psi}{\partial \bar{Y}} \frac{\partial^2 \psi}{\partial \bar{X}^2} + \frac{\partial \psi}{\partial \bar{X}} \frac{\partial^2 \psi}{\partial \bar{X} \partial \bar{Y}} \right) &= -\text{Re}_{Lc}^{1/2} \frac{\partial \bar{P}}{\partial \bar{Y}} \\ &+ \frac{\text{Gr}_{Lc}}{\text{Re}_{Lc}^2} \bar{\theta} + \frac{1}{\text{Re}_{Lc}^{1/2}} \left(\text{Re}_{Lc} \frac{\partial^3 \psi}{\partial \bar{X}^3} + \frac{\partial^3 \psi}{\partial \bar{X} \partial \bar{Y}^2} \right) \end{aligned} \quad (2.2.25)$$

Energy Equation:

$$\left(\frac{\partial \psi}{\partial \bar{Y}} \frac{\partial \bar{\theta}}{\partial \bar{X}} - \frac{\partial \psi}{\partial \bar{X}} \frac{\partial \bar{\theta}}{\partial \bar{Y}} \right) = \frac{1}{\text{PrRe}_{Lc}} \left(\frac{\partial^2 \bar{\theta}}{\partial \bar{X}^2} + \text{Re}_{Lc} \frac{\partial^2 \bar{\theta}}{\partial \bar{Y}^2} \right) \quad (2.2.26)$$

Again, the governing equations in the non-dimensional form indicate that the temperature distribution above the cavity when forced convection is the dominant force is a

strong function of the Prandtl number, the Reynolds number and the characteristic length. From the boundary condition, Eq. 2.2.17, it is obvious that the temperature distribution on top of the glazing plate must be verified experimentally before any analytical attempt can be made. This investigation is an attempt to study the temperature distribution of the glazing plate which may then be incorporated with an analytical approach.

CHAPTER III
LITERATURE SURVEY ON CONVECTIVE HEAT
TRANSFER APPLIED TO SOLAR COLLECTORS

3.1 INTRODUCTION

Since the published works of Thompson [3], Benard [4] and Lord Rayleigh [5], a compendium of research reports, both theoretical and experimental, is available on the nature of natural and forced convection for various geometries and applications. Most of the investigations have been carried out with either isothermal or with constant heat flux boundaries. It is generally recognized that the rate of heat transfer by natural convection depends on parameters such as the physical properties of the fluid, geometry, orientation with respect to the horizontal plane, boundary conditions and the aspect ratio. The effect of some of these parameters such as geometry, orientation and aspect ratio are still not well understood. Frequently, in the published literature, there are several different correlations for a given geometry and flow situation.

A literature survey failed to identify any work directly related to the present research objectives. However, in this chapter, indirectly related investigations to the present study will be reviewed. These

investigations can be categorized as follows:

1. studies related to the Benard cell regime;
2. studies related to the natural convection in the cavity of a solar collector; and,
3. studies related to the forced convection heat transfer on top of the glazing of a flat plate solar collector.

It should be noted that the above subjects in the past have been investigated separately and it is the intention of this study to combine them together. Each of these categories will be discussed respectively in the sections following thermal instability.

3.1.1 Concept of Thermal Instability

In the literature, thermal instability is often referred to as the onset of natural convection. When a fluid in a cavity is subjected to thermally induced buoyancy forces, convection currents or thermal instability occurs in a layer of horizontal viscous fluid. The temperature gradient is the main driving potential. It causes a density change in the vertical direction which leads to a buoyancy force and hence to the fluid motion. Consequently, the velocity and temperature distributions are dependent and must be considered together.

For a sufficiently small temperature gradient and cavity height, the fluid remains at rest, even though a thermally induced adverse stratified temperature gradient exists. In this case, heat is transferred by conduction and the Nusselt number has a value of unity. When the temperature difference across the fluid and the height of the enclosure exceed critical values, the Nusselt number is greater than one and the fluid becomes unstable. This indicates a transition from the conduction regime to the convection regime which occurs through either infinitesimal or finite amplitude disturbances. The motion of the fluid is primarily due to the buoyant release of the potential energy which is strong enough to overcome the stabilizing effects of viscous forces [6].

3.2 THEORETICAL STUDIES OF BENARD CELLS

The experimental studies of Thompson [3] in 1882 and Benard [4] in 1901 were instrumental in motivating a series of theoretical investigations in free convection in an enclosure. Benard experimentally observed convective currents in the form of "polygonal cells". In his honor, these convective flows have been referred to as "Benard cells".

By linearizing the partial differential equations which describe convective flows, Lord Rayleigh [5] in

1916 established a dimensionless parameter which related the buoyant and the viscous forces. The Rayleigh number, $Ra = PrGr_L = \frac{\beta g \Delta T L^3}{\nu \alpha}$, has since been recognized as an important criterion for study of thermal instability. It predicts the onset of natural convection in an enclosure (called critical Rayleigh number) and in general the transition from one flow pattern to another.

Rayleigh's investigations were followed and confirmed by Jeffrey [7,8] and Pellew et al. [9]. Their studies demonstrated that there was a critical Rayleigh number for various boundary conditions as follows:

1. For the case of two free horizontal boundary surfaces (in an atmosphere) [5]

$$Ra_{crit.} = 657.51$$

2. For the case of two rigid horizontal boundary surfaces heated from below [8]

$$Ra_{crit.} = 1707.76$$

3. For the case of one free (open to an atmosphere) and one rigid horizontal surface heated from below [9]

$$Ra_{crit.} = 1100.65$$

Some investigators have predicted that the heating procedures affect the onset of convection and have identified different critical Rayleigh numbers for various heating rates. Currie [10] found that the critical

Rayleigh number was a function of the initial heating rate. For a low heating rate, he found that $Ra_{crit.} = 1708$, while for a high heating rate the critical Rayleigh number dropped to $Ra_{crit.} = 1340$.

The convection cellular motion observed by Benard was thought by Pearson [11] to be caused by surface tension rather than buoyancy forces. Later, Neild [12] suggested that both surface tension and buoyancy forces were the cause of the instability of the motion.

Since linearized theory failed to distinguish between patterns such as rolls, rectangular, triangular or hexagonal cells, Malkus et al. [13] expanded the governing nonlinear equations into a set of linear non-homogeneous equations for the amplitude of the motion and were able to generate various flow patterns. They concluded that the square cells transported more energy than any other suggested shapes. It was found that when $Ra_{crit.} < Ra < 3Ra_{crit.}$ convective heat transfer was a linear function of the Rayleigh number. However, Schalter et al. [14] by using the same technique concluded that the heat transfer in rolls, the simplest of convection motion, was more than the heat transfer in square cells. They also illustrated that motion in the two-dimensional convection rolls was stable while the three-dimensional convection motion was

unstable. For the case of Prandtl number being equal to infinity, Busse [15] established a stability curve and discovered that the two-dimensional rolls existed up to $Ra < 22600$.

The measurements of convection heat transfer have mostly been calculated by determining Nusselt numbers analytically. The results of the various studies have agreed for Rayleigh number up to 2×10^4 . For example, Chorin [16] obtained a Nusselt number equal to 3.15 when $Ra = 2 \times 10^4$ for a fluid confined between two rigid boundaries with a $Pr = 1.0$, and Schneck et al. [17] calculated a Nusselt number equal to 3.147 for the same value of the Rayleigh number. For Rayleigh numbers equal to 9500, 10800 and 17000, Deardoff [18] presented slightly lower Nusselt numbers than the others. These discrepancies were attributed to the assumptions made by the previous investigators.

When a fluid moves from a stable condition to an unstable condition, the temperature profile changes from a linear to a nonlinear profile. This change becomes much more pronounced as the Rayleigh number increases. As the Rayleigh number increases more heat is transferred by convection and the Nusselt number increases. Several investigators have stated that a temperature reversal

profile can occur for various Rayleigh numbers. Veronis [19] illustrated the temperature profile and streamlines for various Rayleigh numbers. He noticed a slight temperature reversal in his calculation for $Ra = 4Ra_{crit}$ and concluded that there was no dependency of the temperature profile on the Prandtl number. However, Herring [20] discovered a small temperature reversal for large Rayleigh number. Samuels et al. [21] reported the critical Rayleigh number dependency on both the Prandtl number and the aspect ratio for $(1/3 < AR < 2$ and $Pr < 1)$.

3.2.1 Experimental Studies of Benard Cells

The first observation of natural convection in cellular patterns of a fluid, between horizontal rigid boundaries heated from below was credited to Thompson [3]. As a fluid he used soapy water. Benard [4] confirmed the hexagonal cellular convection patterns of Thompson by passing a beam of parallel light through a horizontal layer of parafin oil which he then photographed.

During the last few decades, much effort has been expended attempting to explain the cellular convection cells in order to predict the rates of heat transfer in the presence of natural convection motion. This has been met with only limited success. Many investigators have injected powdered particles into the fluid in an enclosure

for observation and have also measured temperatures using probes. This has resulted in the change of physical properties as well as disturbing the flow of the fluid in the cavity. Very few investigators have used optical instruments such as the Mach-Zehnder interferometer for observation and analysis. Of these few, Farhadieh [6] used the interferometer and has presented an excellent literature survey of the previous investigations, prior to 1974, concerning the Benard cells, in his dissertation. Farhadieh used interferometer for studying the two-dimensional Benard convection cells (rolls) and their effects on formation of ice.

Sorokin [22] experimentally investigated the instability of the natural convection in a long cylinder of circular cross-section with an aspect ratio of near unity and heated from below. He used aluminum particles for flow observation and noticed that there were two modes of convection. First, there was a two-dimensional planar rotation above the critical Rayleigh number and secondly a three-dimensional cellular pattern for high Rayleigh numbers. With water confined between two rigid boundaries, Schmidt et al. [23,24] discovered the onset of natural convection for $Ra_{crit.} = 1770 \pm 140$. At the Rayleigh number equal to 45000 they observed that the cellular pattern broke down and turbulent motion ensued.

Some researchers have been concerned with the cell height-to-width ratio as the Rayleigh number increases. Chandra [25] found that the width of the hexagonal cells extended with the increase in the Rayleigh number. At the same time, De Graaf et al. [26] discovered the cell height-to-width ratio to be equal to $1/3$. This contradicted the original theory, since according to Rayleigh the width of the cell was about twice the height.

Various correlations have been developed for the rate of natural convective heat transfer in a horizontal cavity. Among them are those of Van der Held [27] and Jacob [28]. They both correlated the measurements given by Mull et al. [29] but arrived at different results. De Graaf et al. [26] conducted a similar experiment for air in a model tilted at various angles from 0° to 90° with respect to horizontal axis and another set of correlations was deduced. De Graaf et al. concluded that the convective heat transfer through air layers in an enclosed cavity would depend only on the inclination angle when the flow of air was turbulent. Schmidt et al. [30] chose five different liquids and observed the dependency of the heat transfer on the Prandtl number when Rayleigh number was above 10,000. They categorized their results into four distinct regions:

- (a) The creeping region - with extremely small fluid velocities in the form of honeycomb cells when $1700 < Ra < 3000$;
- (b) The laminar region - flow patterns in the form of uniform stripe cells and in which the Nusselt number was a function of the Rayleigh number to the $1/4$ power;
- (c) The transition region - flow patterns in the form of disintegrated stripe cells when $8000 Pr^{0.2} < Ra < 18000 Pr^{0.2}$;
- (d) The turbulent region - flow patterns with a completely disordered cells and the Nusselt number was a function of the Rayleigh number to the $1/3$ power when $Ra > 18000 Pr^{0.2}$.

O'Toole et al. [31] recognized that the previous correlation had been restricted to a narrow range of data, so they developed their own version of the correlations. They utilized all the available data and divided the flow into three different regions, mainly;

$1700 < Ra < 3500$	initial region
$3500 < Ra < 10^5$	laminar region
$10^5 < Ra < 10^9$	turbulent region

From their correlations it is apparent that the Prandtl number did not affect the heat transfer in the laminar

region and it was important in the turbulent region. The results of all the above correlations are presented in Table 3.2.1.

For observing various patterns, Sommerscale et al. [32] conducted an experiment using oil heated from below with rigid boundaries and in some cases the top boundary was removed. They observed various combinations of the convection currents with rolls and square cells in the laminar region. They also obtained a temperature profile which did not agree with the previous predictions and results.

Occasionally, specific patterns in a cavity are formed because of the types of boundaries used. Koschmieder [33] discovered that the lateral boundaries determined the specific convection patterns. Catton et al. [34] were also concerned with the effect of lateral boundaries on the convective heat transfer. They therefore performed an investigation for small aspect ratio. Their studies confirmed that the boundary effects had caused a 5% difference between their results and those of Silverston [35].

The occurrence of the temperature gradient reversal in a horizontal enclosure, where an inflexion point occurs, has been detected mostly by the investigators who have

used optical methods. Gille [36] using a Michelson interferometer obtained a vertical temperature profile in a horizontal enclosure. The results showed the temperature reversal for $Ra = 16Ra_{crit}$. However, Farhadieh et al. [37] used a Mach-Zehnder interferometer and observed two-dimensional rolls with the Rayleigh numbers as high as 23400. The reversal in the temperature profile was determined for $Ra = 3.8Ra_{crit}$, which disagreed with the results obtained by Gille [36].

One concern has been to discover the Rayleigh number at which the transition from two-dimensional to three-dimensional convection occurs. Rossby [38], employing water as a medium, observed that rolls lost their two-dimensionality at a certain Rayleigh number between 11000 and 26000, to assume a triangular shape. Also, the size of rolls increased when the value of the Rayleigh number increased. Krishnamurti [39] discovered that for water two-dimensional rolls were transformed to three-dimensional ones at $Ra > 13Ra_{crit}$. In the turbulent region, she observed various transition regions. The instability of the two-dimensional rolls was also considered by Busse et al. [40], who marked the transition to the three-dimensional rolls at about $Ra = 22,600$. Willis et al. [41] measured the dependency of the cell height-to-width ratio for Rayleigh numbers between $2000 < Ra < 31,000$.

They concluded that for various fluids the ratio decreased with increasing Rayleigh numbers.

3.3 INCLINED AND HORIZONTAL FLUID LAYERS - STUDIES RELATED TO SOLAR COLLECTORS

With an increasing interest in solar energy utilization, investigators made use of the similarity between a solar collector cavity and the available information in enclosure cavities heated from below. Tabor [42] presented a summary of all the previous experimental studies in natural convective heat transfer in flat plate enclosed cavities bounded by differentially heated isothermal plates. The time period of this review was up to 1958. The studies which were most related to solar collectors were the ones which were presented earlier by De Graaf et al. [26] and Robinson et al. [43]. The purpose of the work by Robinson et al. was to predict heat losses for the home construction industry. The results were adapted by Tabor to the design of the solar collector.

Globe et al. [44] conducted an experiment for water, mercury and silicone oils in a horizontal cavity heated from below with a range of Prandtl numbers between 0.2 and 11560. The authors determined the Prandtl number effects on the average Nusselt number. Their work was extended to an inclined cavity by Dropkin et al. [45].

From their results, given in Table 3.2 it is apparent by their use of the $1/3$ exponent for the Rayleigh number that they assumed the flow was turbulent for all the inclination angles. This assumption was later questioned by MacGregor et al. [46] with regard to the existence of turbulent flow for the Grashof numbers less than 10^6 .

Boundary layer theory suggests that the exponent for the Grashof or the Rayleigh number should be $1/4$ for laminar and $1/3$ for turbulent flow. This also has been questioned by some researchers with regard to solar collectors. Duchberg et al. [47] recommended that for the horizontal cavity the exponent should never exceed 0.29. On the other hand, Tables 3.1 and 3.2 show other possible values for this exponent.

During the 1970s, the bulk of research on heat transfer in the solar collector has occurred at the University of California, Los Angeles, the University of Waterloo and the University of Wisconsin. Excellent reviews of the works for this period have been presented by Randall [2] and Elsherbiny [48]. All of these investigations make one common assumption which is that the bottom and top plates remain isothermal. Also, the cavity of the solar collector has been considered separately from the forced convection on top of the glazing. The majority of

TABLE 3.1 Experimental Correlations (Benard Cells)

Ref.	Laminar Region	Transition Region	Turbulent Region
[26]	$Nu = 1, Gr < 2 \times 10^3$	-	$Nu = 3.8, 5 \times 10^4 Gr < 2 \times 10^5$
	$Nu = 0.0507 Gr^{0.40}$	-	$Nu = 0.0426 Gr^{0.37}$
	$2 \times 10^3 < Gr < 5 \times 10^4$	-	$Gr > 2 \times 10^5$
[27]	$Nu = 1, Gr < 10^3$	-	
	$Nu = 0.0601 Gr^{0.36}$	-	$Nu = 0.0463 Gr^{0.36}$
	$2.5 \times 10^3 < Gr < 6 \times 10^4$	-	$2.5 \times 10^5 < Gr < 10^7$
[28]	$Nu = 1, Gr \rightarrow 0$	-	
	$Nu = 0.195 Gr^{1/4}$	-	$Nu = 0.068 Gr^{1/3}$
	$Gr < 5 \times 10^5$	-	$Gr > 5 \times 10^5$
[30]	$Nu = 0.0012 Ra^{0.9}$		
	$1700 < Ra < 3000$		
	$Nu = 0.24 Ra^{1/4}$	$Nu = 0.30 Ra^{0.16} Pr^{0.21}$	$Nu = 0.10 Ra^{0.31} Pr^{0.36}$
	$3000 < Ra < 8000 Pr^{0.2}$	$8000 Pr^{0.2} Ra^{18000} Pr^{0.2}$	$Ra > 18000 Pr^{0.2}$
[31]	$Nu = 0.00238 Ra^{0.816}$		
	$1700 < Ra < 3500$		
	$Nu = 0.0229 Ra^{0.252}$		$Nu = 0.104 Ra^{0.305} Pr^{0.84}$
	$3500 < Ra < 10^5$		$10^5 < Ra < 10^9$

TABLE 3.2 Existing Correlations for Horizontal and Tilted Collector Models

Ref.	Correlations	Remarks
45	$Nu = C(Ra)^{1/3} (Pr)^{0.074}$ <p>C = 0.069 Horizontal C = 0.049 to Vertical</p>	$5 \times 10^4 < Ra < 7.17 \times 10^8$ $4.41 < AR < 16.56$ For liquids
70	$Nu_L = 0.118 [Gr_L Pr \cos^2(\phi - 45)]^{0.29}$	$4 \times 10^3 < Gr < 3.1 \times 10^5$ $9 < AR < 36$ For air
75	$Nu_L = 1 + 1.44 \left[1 - \frac{1708}{Ra_L \cos \phi} \right]^* \cdot \left[1 - \frac{(\sin 1.8\phi)^{1/6} 1708}{Ra \cos \phi} \right]$ $+ \left\{ \left(\frac{Ra \cos \phi}{5830} \right)^{1/3} - 1 \right\}^*$ <p>where $[X]^* = \frac{X + X }{2}$</p>	$\phi < 60^\circ$ For air

studies deal with the reduction of the heat losses from the top plate. This is accomplished by inseting honeycomb cells inside the cavity [49 to 65], or increasing the absorption area by making the bottom plate corrugated [2,66,67].

The experimental model at the University of Waterloo was designed by Raithby and Hollands [68,69] and was utilized for almost all of the experimental studies there. The model consisted of two copper plates 12.7 mm thick, with dimensions of 635 mm by 635 mm. The model was then placed in a pressure vessel and the heat transfer rate was measured in the central region of the cavity. Various Rayleigh numbers were obtained by changing the vessel air pressure and heating the bottom plate using heater and guard heater arrangements. The results of these studies agreed very well with the previous investigations. Contrary to the model at the University of California which was limited to low and moderate aspect ratio ($AR < 15$) the model at the University of Waterloo was capable of providing results with high aspect ratios ($AR < 110$) and high Rayleigh numbers.

A Mach-Zehnder interferometer was used at the University of Wisconsin for their investigations. This interferometry limited the size of the model to 45.7 cm.

long and 10.2 cm wide copper plates. Randall et al. [70] conducted an experimental study for a tilted cavity between 45 to 90 degrees. The results were correlated by an equation which showed that the heat transfer was independent of the aspect ratio. Interferometry was also used by Brooks et al. [71]. They examined the temperature fields and the heat transfer within vertical, inclined and horizontal enclosure arrangements. It was concluded that some of the thermal boundary conditions which had generally been assumed in numerical studies were unrealistic. In the horizontal air layers, it was also discovered that the turbulent regime existed for $Gr > 9.77 \times 10^4$, with a thick, nearly isothermal central region and continuous thermal boundary layers on both the hot and the cold boundaries.

For an inclined cavity with respect to the horizontal axis, it was suggested by Hart [72] and Clever [73] that the correlation of gravity, g , in Rayleigh numbers can be replaced by $g(\cos\phi)$ and also in the Nusselt number correlation equation for the fluid with an infinite Prandtl number and a very large aspect ratio. However, Buchberg et al. [47] and Arnold et al. [74] suggested that the results were actually valid only for low Prandtl number fluids and aspect ratios greater than 10 and 3, respectively.

Hollands et al. [75] investigated heat transfer in an inclined air enclosure of high aspect ratio, heated from below. The Rayleigh number range covered was from subcritical to 10^5 ; the range of tilt angle from the horizontal axis was between zero to 70 degrees. Although it was anticipated that the results might be identical to the results for the horizontal layer if one had replaced Ra by $Ra \cos\phi$, significant departures from this behaviour were observed, particularly in the range of $1708 < Ra \cos\phi < 10^4$ and $30^\circ \leq \phi \leq 60^\circ$, where ϕ was the tilt angle. A recommended relationship was then given for the Nusselt number as a function of $Ra(\cos\phi)$ and the range of angle of inclination. Their results and the other correlations are presented in Table 3.2. These correlations have been developed by simply heating the enclosure isothermally from below and by cooling the top plate isothermally. They did not consider the effect of wind on the glazing surface.

3.4 FORCED CONVECTION ON THE GLAZING OF SOLAR COLLECTORS

To calculate the wind related heat losses on top of solar collector glazing, most designers and researchers follow Jerges (1934) equation given by McAdams [76] which is

$$\bar{h}_w = a + b V_w^d \quad (3.4.1)$$

For solar collectors, many texts and papers [77 to 80] also recommend the following equation:

$$\bar{h}_w = 5.7 + 3.8 V_w \quad \text{W/m}^2\text{-}^\circ\text{C} \quad (3.4.2)$$

where V_w is the wind speed in m/s and the data were taken for 0.5 m² plate. Since this equation overestimates the wind related heat losses, it is possible that the effects of free convection and radiation are included. Watmuff et al. [81], realizing this overestimation, reported that this equation should be changed to

$$\bar{h}_w = 2.8 + 3.0 V_w \quad \text{W/m}^2\text{-}^\circ\text{C} \quad (3.4.3)$$

However, Duffie and Beckman [82] suggest that since the data for the above equation were taken for the characteristic length of 0.5 m, it is not reasonable to assume that Eq. 3.4.3 is valid at other plate lengths. Mitchell [83] investigated the heat transfer for various shapes and showed that many shapes could be represented by a sphere when the equivalent sphere diameter is the cube root of the volume and suggested that

$$\text{Nu} = 0.42 \text{Re}^{0.6} \quad (3.4.4)$$

In the case of natural convection from a hot flat plate facing upward, Lloyd et al. [84] recommend the following

equations:

$$\text{Nu} = 0.76 \text{ Ra}^{1/4} \quad 2.6 \times 10^4 < \text{Ra} < 10^7 \quad (3.4.5)$$

$$\text{Nu} = 0.15 \text{ Ra}^{1/3} \quad 10^7 < \text{Ra} < 3 \times 10^{10}$$

where the characteristic length is four times the area divided by the wetted perimeter. For vertical plates, McAdams [76] gives

$$\text{Nu} = 0.59 \text{ Ra}^{1/4} \quad 10^4 < \text{Ra} < 10^9 \quad (3.4.6)$$

$$\text{Nu} = 0.13 \text{ Ra}^{1/3} \quad 10^9 < \text{Ra} < 10^{12}$$

where the characteristic length is the plate height.

Duffie and Beckman [82], in their recent book, took the data by Mitchell [83] and recommended the following equation for the convective heat transfer coefficient.

$$h_{\text{wind}} = \max \left[5, \frac{8.6 V_w^{0.6}}{L_c^{0.4}} \right] \quad (3.4.7)$$

where V_w is in meters per second and L_c is the cube root of the house volume in meters. At a wind speed of 5 m/s (which is close to the world average wind speed) and a characteristic length of 8 m, Eq. 3.4.7 yields a heat transfer coefficient of $10 \text{ W/m}^2 \cdot \text{C}$. However, the authors suggest that additional experimental evidence is needed for their recommendations.

Recently, other authors [85 to 88] have recognized the diversity of the problem and have proposed the following equation:

$$\bar{h}_w = 0.86 \frac{K}{L_c} Re_{L_c}^{1/2} Pr^{1/3} \quad W/m^2 \cdot C \quad (3.4.8)$$

where the characteristic dimension length L_c is defined as four times the area divided by the wetted perimeter. Tien [88] performed an experimental study to determine the local and average heat transfer coefficients and the patterns of fluid flow for a square plate positioned at various orientations to the flow direction. A naphthalene sublimated square (76.2 x 76.2 mm) model plate was used at various angles of attack to an oncoming air-flow in the wind tunnel. The Reynolds number range extended from 20,000 to 90,000. The sublimation technique enabled the author to determine the dimensionless heat (mass) transfer coefficient, expressed in terms of the Colburn J-factor. The results were given by Sparrow et al. [87] in the form of a non-dimensional equation (3.4.8). For laminar flow (i.e. Reynolds number less than 10^6) over a very wide flat plate at zero angle of attack, the analysis of Pohlhausen yields, for the same equation, a convective heat transfer coefficient of 0.94 with the same characteristic length. Tien assumed that the flow (wind), rather than passing over the collector, is attacking the collector

glazing at an angle. It was also assumed that the glazing of the collector remained isothermal. All the correlation results on the surface of glazing related to the present investigations are tabulated in Table 3.3.

In the present experimental investigation with the proposed model, all three convective heat transfer problems are considered. First, the formation of two-dimensional convection cells in a horizontal enclosure containing air heated from below and second, the effect of non-dimensional parameters on the rate of convection heat transfer in a simulated horizontal cavity. Finally, the natural and forced convection on the surface glazing of a simulated horizontal collector will be considered.

TABLE 3.3 Wind Related Heat Losses Correlations

Reference	Correlations	Remarks
[77-80]	$\bar{h}_w = 5.7 + 3.8 v_w$	$W/m^2-^{\circ}C$
[81]	$\bar{h}_w = 2.8 + 3 v_w$	$W/m^2-^{\circ}C$
[82]	$h_w = \max\left[5, \frac{8.6 v_w^{0.6}}{L_c^{0.4}}\right]$	$W/m^2-^{\circ}C$
[83]	$Nu = 0.42 Re^{0.6}$	
[85-88]	$\bar{h}_w = 0.86 \frac{K}{L_c} Re_L^{1/2} Pr^{1/3}$	$W/m^2-^{\circ}C$

CHAPTER IV

LONG PATH DIFFERENCE INTERFEROMETER

4.1 INTRODUCTION

Interference phenomenon has had a considerable influence on the development of science in general, fluid flow and heat transfer in particular. Thomas Young's [92] observation and explanation of the interference of the beams through two holes provided the basis for Fresnel's wave theory of light and the same experiment has been used as the foundation of modern coherence theory.

The interferometric technique, derived from the interference phenomenon [93] is now one of the important methods of experimental heat transfer analysis in engineering. The father of visible light interferometry was Michelson, who was awarded the Nobel prize in physics in 1907 for "his optical instruments of precision and the spectroscopic and metrological investigations he has executed with them". Since his discovery, many modifications of interferometers have been developed. Among them, the most popular ones are the Mach-Zehnder, Twyman Green and the long path difference interferometers.

4.2 LONG PATH DIFFERENCE MACH-ZEHNDER INTERFEROMETER

The Mach-Zehnder interferometer, the most common but also the costliest, was utilized for this study for the following reasons:

- 1) Compared with other measurement methods, in the area of natural and forced convective heat transfer, it yields results which have a considerable degree of accuracy.
- 2) The temperature measurements are free from disturbances.
- 3) The rapidly changing processes can be accurately followed since the light beam is considered as essentially inertialess.
- 4) It provides a temperature map which can be recorded on a single interferogram rather than a single point.

Like all other measurement methods, such as calorimetric measurements or thermocouples, the interferometer has disadvantages as well. The medium under consideration must be transparent to radiation. The medium has to be enclosed, with two sides of the enclosure having high quality optical flats. Interferograms record the changes of the medium only in two-dimensional cases [94]. The long path difference Mach-Zehnder interferometer basically yields a refractive index field which requires subsequent

calculations for interpretation as a temperature field. However, the disadvantages did not introduce any restrictions on this investigation since the air was transparent and the flow was considered to be two-dimensional. This last assumption, as mentioned previously, was verified by a visual smoke test.

The long path Mach-Zehnder interferometer, at The University of Western Ontario Engineering Laboratory, was constructed and developed in 1970 by Brown and Tarasuk [95]. It has been adapted extensively [90, 95 to 104]. The instrument was modified to suit the requirements of this particular study.

The components of a Mach-Zehnder, shown in Figure 4.1 consisted of a light source, two beam splitters, two flat mirrors, two optical lenses, two parabolic mirrors, two optical flats and a camera or viewing screen. The point light source was monochromatic and parallel which was divided at the first splitting plate into two identical light beams. These two beams traversed separate paths, one as a reference beam, and the other through a heated test model until they reached the second splitting plate. Depending on the path lengths, the two beams arrived at the camera or screen either in phase or out of phase. This gave rise to an interference pattern at

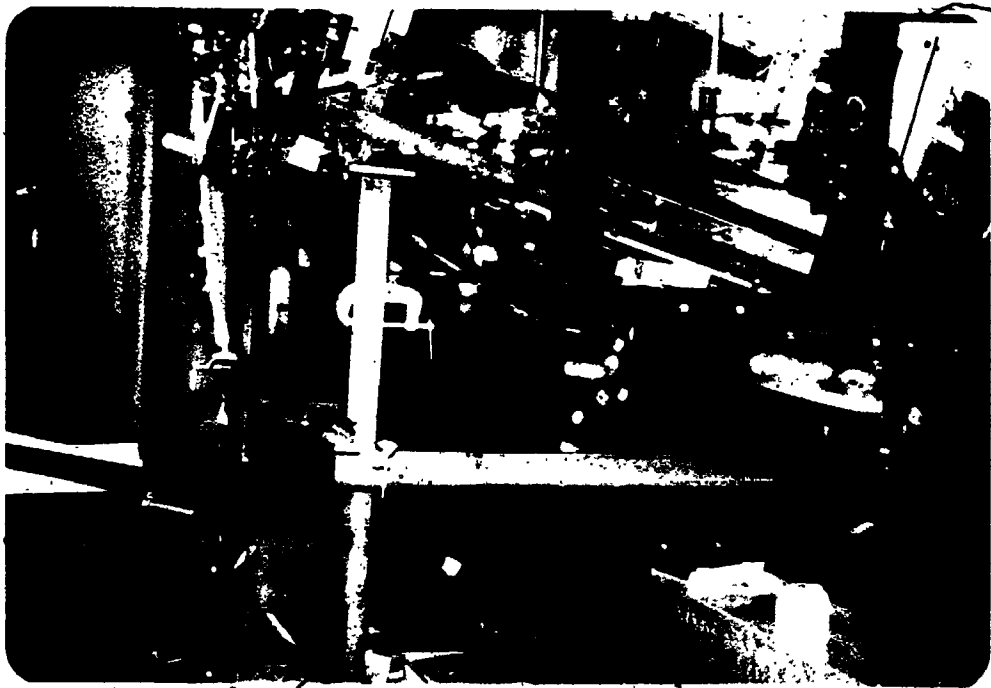


FIGURE 4.1 The Long Path Mach-Zehnder Interferometer
Integrated With the Wind Tunnel

the screen.

Two types of interference patterns were possible.

One type, the infinite fringe field (shown in Figure 4.2), consisted of a uniformly illuminated field and occurred when all the mirrors and splitting plates were parallel. The second type, which is referred to as the finite fringe field, consisted of a series of bright bands separated by dark bands and occurs when one of the plates was rotated slightly (see Figure 4.3).

In this study interferograms with both fringes were taken and utilized. Although each has advantages and disadvantages, by using both methods details of flow visualization and heat transfer analysis were possible.

Advantages of the finite fringe interferogram include the following:

- 1) even small thermal gradients or fringe distortions can be analyzed;
- 2) it is applicable to irregular objects and larger models;
- 3) finite fringe interferograms are easily obtained and a constant monitoring or adjustment of optics is not necessary;
- 4) the fringe patterns are less sensitive to minor

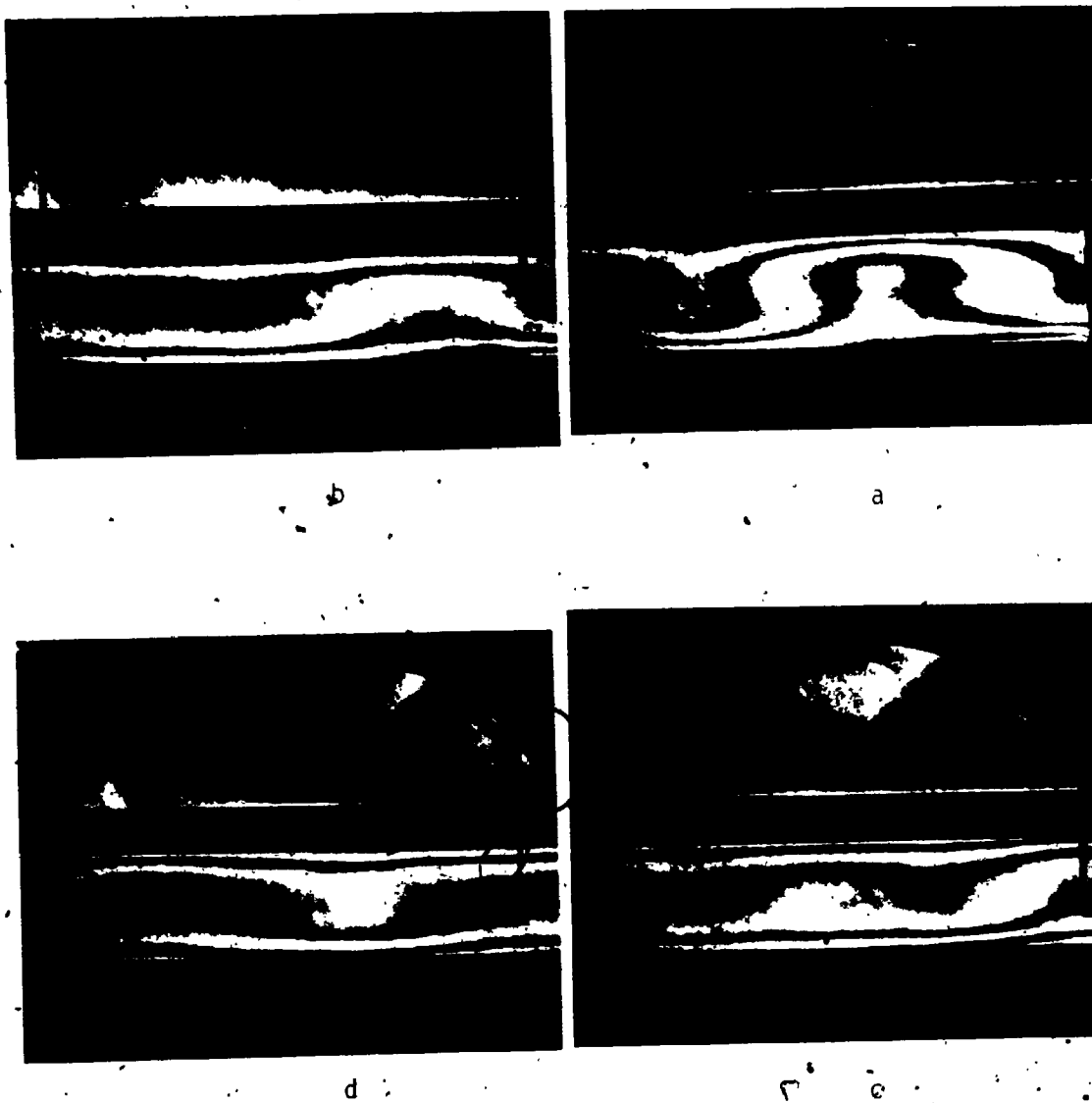


FIGURE 4.2 Interferograms with Infinite Fringe Fields;

$AR=17.7$, $Re=63350$, $Ra=8300$, $T_{HC}=30.1\text{ }^{\circ}\text{C}$, $T_{CB}=24.4\text{ }^{\circ}\text{C}$

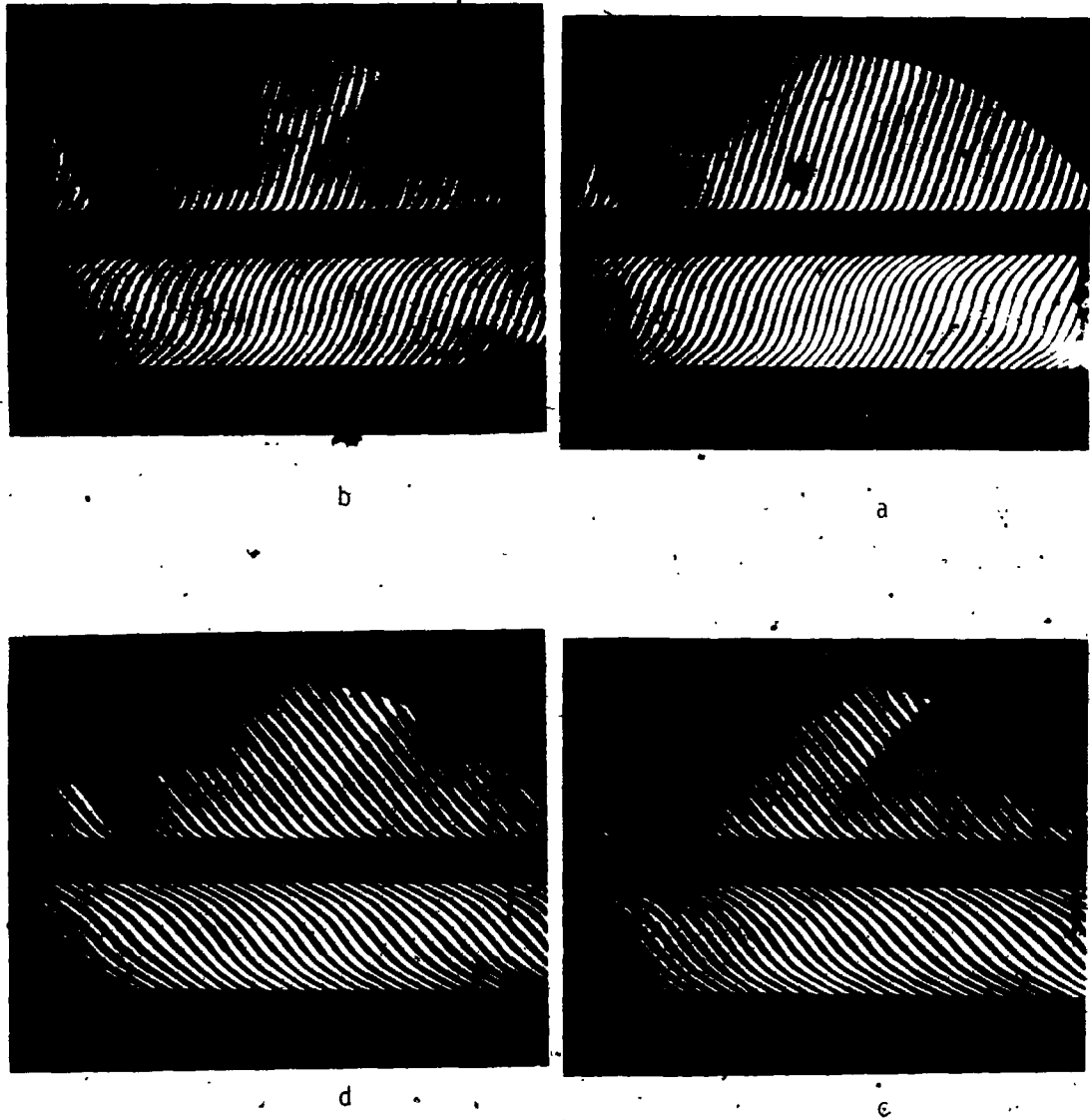


FIGURE 4.3 Interferograms with Fringe Fringe Fields;

$AR=17.7$, $Re=63350$, $Ra=8300$, $T_{HC}=30.1\text{ C}$, $T_{CB}=24.4\text{ C}$

vibrational disturbances;

- 5) there is an overall improvement in the accuracy of results in view of the well defined reference.

Disadvantages of a finite fringe interferogram are as follows:

- 1) The reference fringe shift must be calculated.
- 2) A shifted fringe field does not represent an isotherm, and
- 3) Finite fringes do not in general demonstrate clearly the flow patterns.

Advantages of the infinite fringe field include:

- 1) The shifted fringes in the interferograms represent isotherms or constant temperature map, and
- 2) The flow pattern of the medium can be easily recognized.

A list of the disadvantages of the infinite fringe field includes:

- 1) It cannot be easily obtained.
- 2) It is very sensitive to slight vibrations.
- 3) The number of fringes must be at least more than five.

4) It is not as accurate as finite fringe field.

A technique was developed (discussed in Chapter VI) by which both finite and infinite fringe field interferograms were attainable. The interferograms with infinite fringe fields were utilized for flow visualization and interferograms with finite fringe fields were used for analysis. The mathematical equations related to the interferometry, used for calculations of the temperatures, are given in Appendix B.

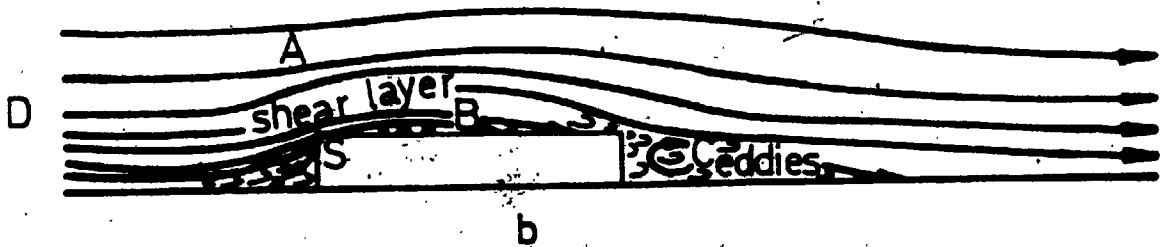
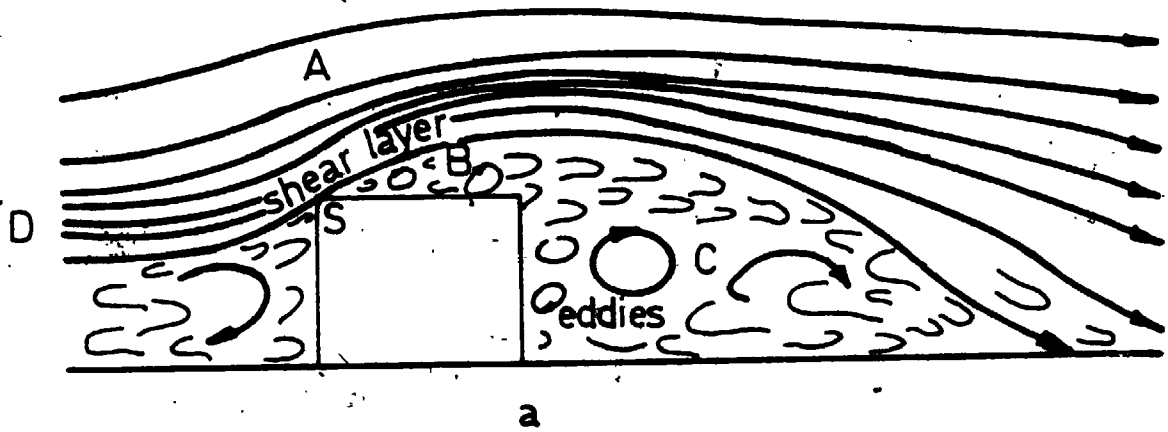
CHAPTER V

EXPERIMENTAL APPARATUS

5.1 INTRODUCTION

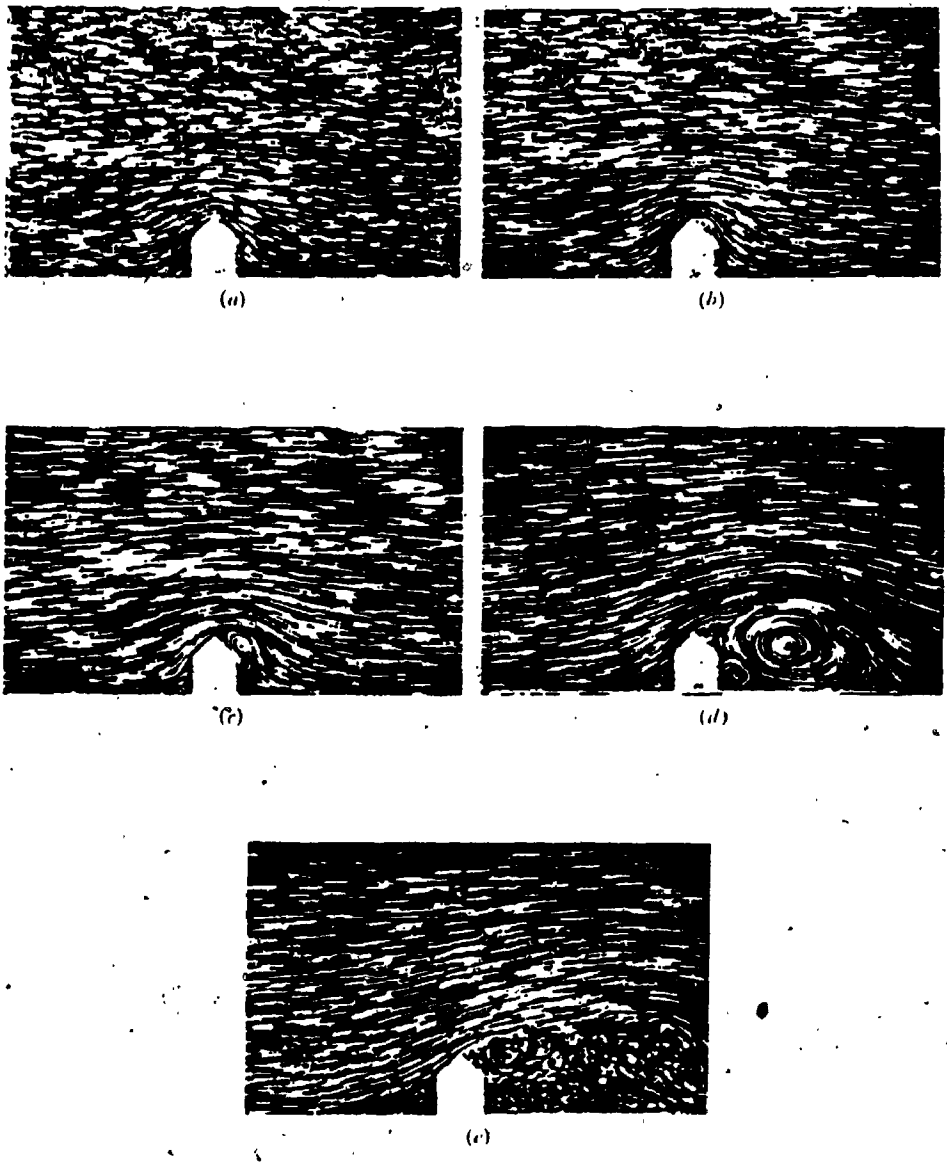
It has been shown that solar collectors are usually exposed to severe atmospheric wind conditions. These conditions impose a boundary layer effect on the removal of heat from the glazing of the solar collectors. Thus, any attempt to simulate the heat losses from the top of a collector would be more realistic if attention was given to the effect of the external flow above the collector cavity. The desired boundary layer flow should simulate the lower portion of the atmospheric conditions. Special attention should be given to the simulation of the temperature changes of the solar collector glazing.

Low speed wind tunnels have been used for the simulation of the boundary layer effects on the roofs where solar collectors are generally mounted. Figures 5.1 and 5.2 [89] show possible boundary layer effects on flat as well as pitched roofs respectively. A variety of angles of attack/pitch are possible. Tien [88] considered a wide range of angles of attack/pitch and yaw for wind on an isothermal sublimated square flat plate. The results were correlated by using mass transfer to heat transfer for solar collectors. However, in this study



- S Separation point
- A Outer region
- B Inner region
- C Wake region
- D Undisturbed free stream

FIGURE 5.1 Wind Streamlines Passing Over Buildings



FLOW DIRECTION 

FIGURE 5.2 Stages in the Development of Flow (From Rest) Past a Model of a House (after Nokkentved, 1932)

the flow was assumed to have the condition similar to that shown in Figure 5.2 namely, parallel to the glazing surface.

In most places, such as Southern Ontario, including the upper Great Lakes, the effect of wind on solar collectors is more pronounced when the wind velocity is strongest in the winter, during the day, when solar collector operation is required. It is weakest in the summer as shown in Table 5.1 when solar collectors are hardly used for space heating.

The above condition requires a closer simulation of a solar collector when atmospheric conditions resulting from the boundary layer effect (wind) on the top surface can be considered as an important parameter.

The remainder of this chapter will first describe the wind tunnel-interferometry arrangement and then the model itself.

5.2 WIND TUNNEL DESCRIPTION

The wind tunnel was designed and constructed by Allen [90] and was modified to meet the specific needs of this investigation. The wind tunnel has a closed working section and closed return section. The wind tunnel has a working section that has a 30.50 cm by 45.70 cm rectangular

TABLE 5.1 Hourly Wind Statistics for Diurnal Variation
 By Month Based on 26.01 Years of Data.*
 (London, Ontario, 43-02N 81-09W E1.912)

H/M	JAN.	FEB.	MAR.	APR.	MAY	JUN.
1-6	5.078	4.652	4.596	4.035	3.297	2.570
7-12	5.295	5.038	5.280	5.182	4.623	3.849
13-18	6.015	5.872	6.201	6.417	5.738	5.155
19-24	5.212	4.906	4.859	4.717	3.955	3.316

* From Atmospheric Canada Report, File 1953 - 1978

cross-section. This cross-section dictates a wind tunnel length of approximately 6 meters. The maximum velocity in the test section, without the insertion of any honeycomb flow straightener, is approximately 18 m/s with no test model in place. Upstream of the test section is a contraction which reduces the cross-sectional area of the tunnel by a factor of four. This reduces the level of turbulence in the working section and decreases the power consumption of the tunnel by permitting a lower velocity in the return circuit of the tunnel for the case of closed circuit arrangement. A 10.2 cm thick section of aluminum honeycomb is located at the entrance to the contraction. The honeycomb serves as a flow straightener and breaks up the large scale eddies that come off the fan. Vanes are mounted in the four corners of the tunnel to ensure a smooth flow at these points. These vanes were designed according to accepted wind tunnel construction principles. The angle of divergence of the diffusing sections is always less than 6 degrees to prevent separation of the flow from the walls of the diffusers.

The tunnel is powered by a 61 cm diameter, tube-axial fan having four blades of aerofoil design. The fan is belt-driven by a hydraulic motor mounted outside the wind tunnel. This was done to avoid the transfer of heat from the motor to the air circulating in the tunnel. Fan

speed is variable from zero to approximately 1200 RPM by adjusting the volume of flow from the pump unit to the hydraulic motor.

The modification of the tunnel included the following:

1. Raising of the working section to allow for the adjustment of the bottom plate of the model. This permitted various changes in the aspect ratio of the cavity.
2. Changing the upstream rigid section which joined to the working section to allow the accommodation of a horizontally oriented solar collector or model. Also, a variety of tunnel sections were constructed to allow the tilt angle to be changed in 15° increments from 0° (horizontal) to 60° as shown in Figure 5.3.
3. Insertion of honeycombs 5.08 cm thick to serve as flow straighteners and to break up the large scale eddies generated by the fan.
4. Changing the tunnel from a closed loop to an open loop system since the temperature of the circulating air in the tunnel was changing constantly because of the heat loss from the top of the model.
5. Installation of two flexible ducts 40.64 cm in diameter which mixed the return and supply air in an

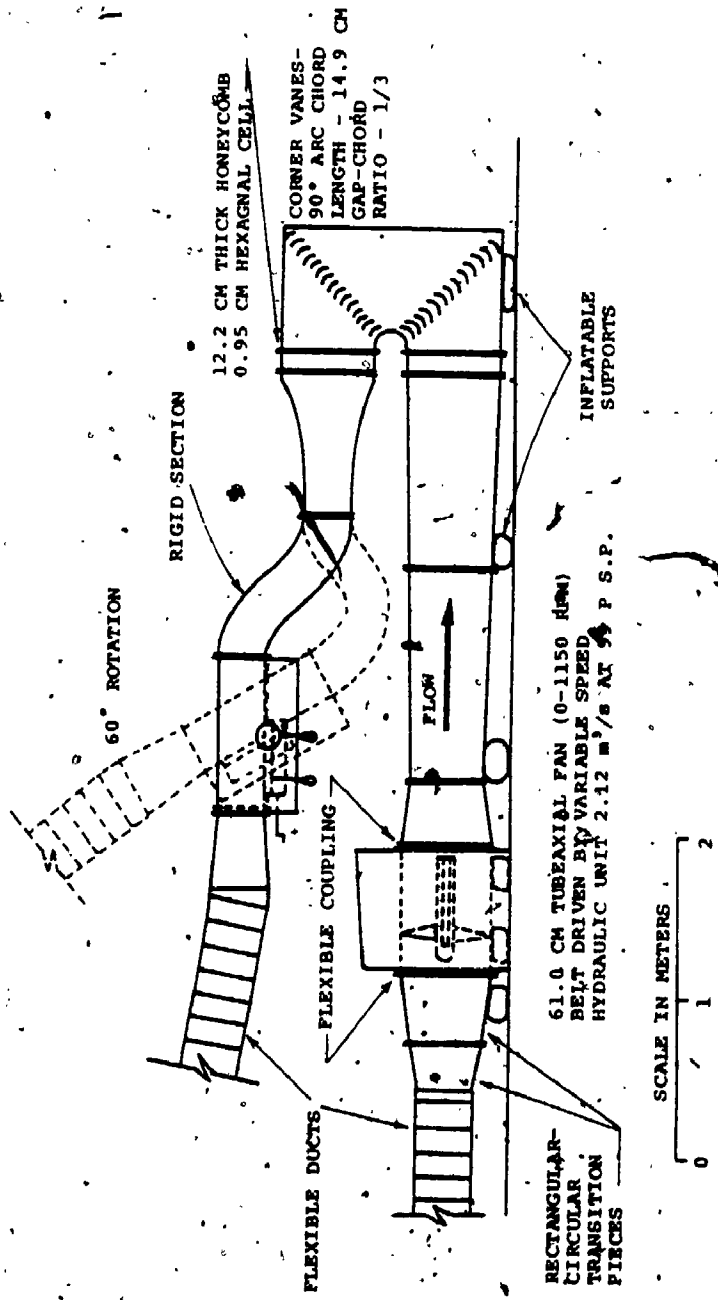


FIGURE 5.3 Modified Schematic Diagram of the Wind Tunnel and the Model

adjacent room. This prevented any large scale turbulence from disturbing the optical system of the interferometer.

6. A minimizing of the vibrations transmitted to the interferometer which were generated by the wind tunnel. This was accomplished by the use of flexible couplings in the wind tunnel and by the installation of pneumatic air sacs for support of the fan housing, the motor and the interferometer.

5.2.1 Velocity Distribution Measurement in the Wind Tunnel Test Section

The honeycombs in the upstream section of the wind tunnel were adjusted to ascertain the uniformity of the flow passing over the cold plate of the model.

The velocity measurements were made using a plane rake. This consisted of a matrix of 48 impact tubes and 6 static pressure tubes, which was designed by Craze [91]. The operating configuration is shown in Figure 5.4 with close-up views of impact tubes in Figure 5.5.

The tubes were made from 16 gauge stainless steel hypodermic tubing and protruded 4.31 cm (25 tube diameters) upstream with respect to their supports. The impact tubes were first filed and polished with emery cloth in a lathe chuck, then electrochemically etched in a bath of

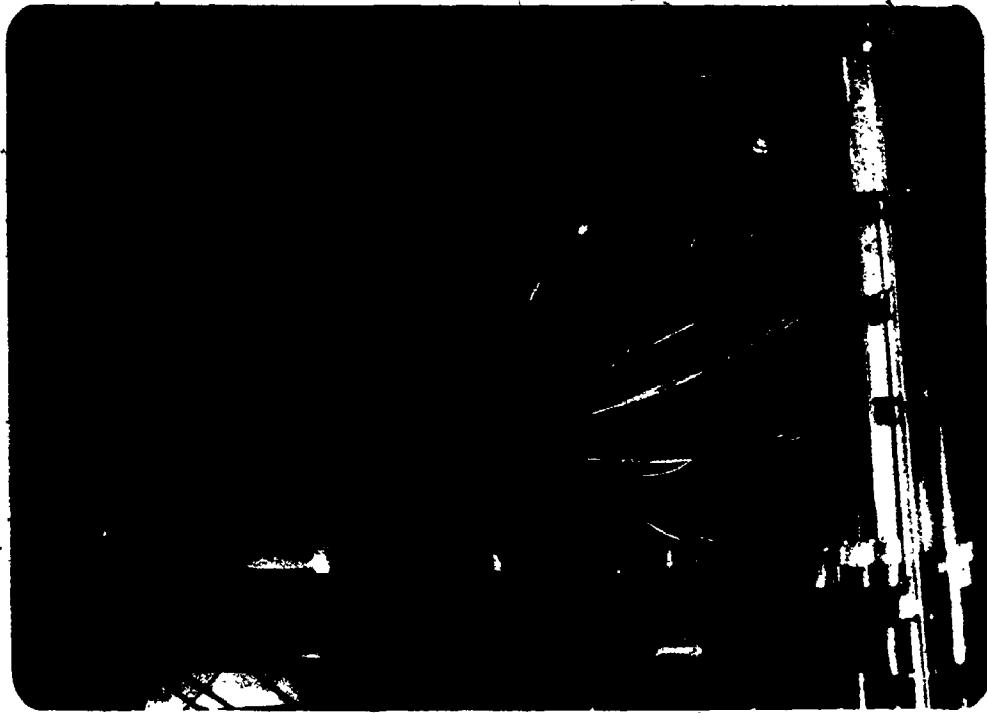
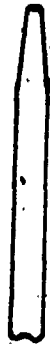


FIGURE 5.4 Multiple Tap Rake



i) Impact



ii) Static

FIGURE 5.5 Pressure Tubes for Rake

concentrated nitric acid to produce a razor sharp entrance lip. The diameter of these tubes was about 1.5 mm. The static pressure tubes were made by first plugging one end with epoxy resin and rounding to a hemispherical shape. Four holes, equispaced circumferentially, were then drilled with a No. 80 drill, about .33 mm, approximately 4 tube diameters from the nose.

The hypodermic tubes were soldered to the brass rake frame with appropriate airfoil sections ensuring consistent orientation of the tubes normal to the plane of the frame. The rake was then positioned on the downstream section of the wind tunnel.

The reference air velocity was chosen to be at the position upstream on the centreline of the working section and was measured by a pitot tube. A Scanivalve multi-pressure transducer and an integrating voltmeter furnished direct readings of the pressure differentials across the two pressure taps from the pitot tube and similarly across the taps from the plane rake. A typical distribution of velocity in the wind tunnel is given in Figure 5.6.

The wind tunnel was positioned so that the air flow in the tunnel test section was perpendicular to the interferometer reference test beam and to the test beam passing through the model. The reference beam was directed

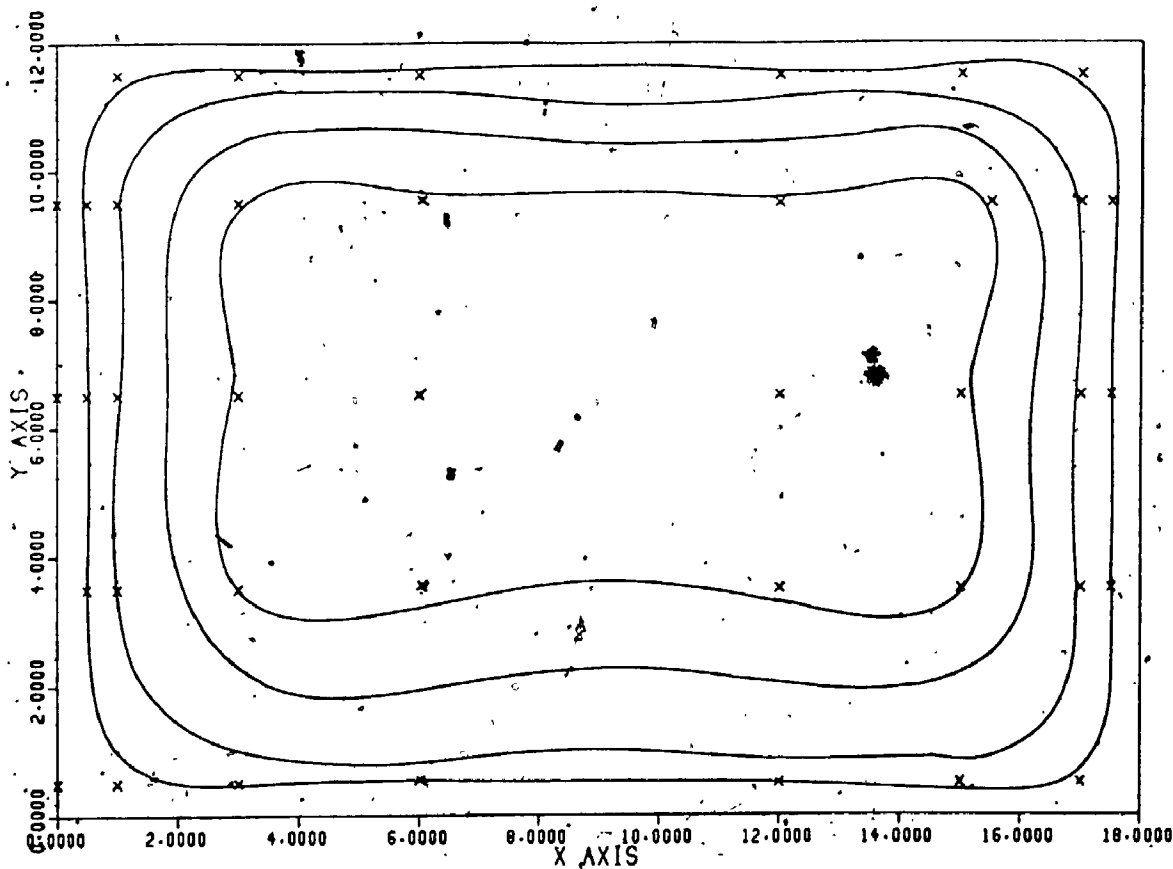


FIGURE 5.6. Contour Plot of Typical Velocity Distribution Within the Wind Tunnel.

through a 0.635 cm diameter aluminum pipe to prevent any disturbance by the air flow. Another important feature of the tunnel test section was the inclusion of two optical flats 15.24 cm diameter, 2.54 cm thick, mounted on the 1.27 cm thick perspex vertical walls which housed the model. The interferometer test beam passed undisturbed through these optically finished flats. The wind tunnel was then set on pneumatic air sacs to isolate the tunnel from any building vibrations.

5.3 LONG PATH MACH-ZEHNDER DIFFERENTIAL INTERFEROMETER

The schematic diagram of the long path Mach-Zehnder differential interferometer used in this investigation is shown in Figure 5.7. Various light source lasers were tested and a 7 mW Helium-Neon laser (A) was used as the light source. This emitted the best uniphase monochromatic wave front light beam required for this study. Because of the single light frequency, the entire laser output could be used without the need for filtration. The laser behaved as an ideal point source, which simplified imaging of the source on the plane of interference. B_1 and B_2 were 92.54 cm diameter semi-silvered beam splitters, mounted in such a way that they rotated about vertical and horizontal axes. D_1 and D_2 were double convex lenses, 6 mm in diameter and 7.6 mm in focal length. E_1 and E_2 were two parabolic mirrors of 31.75 cm diameter

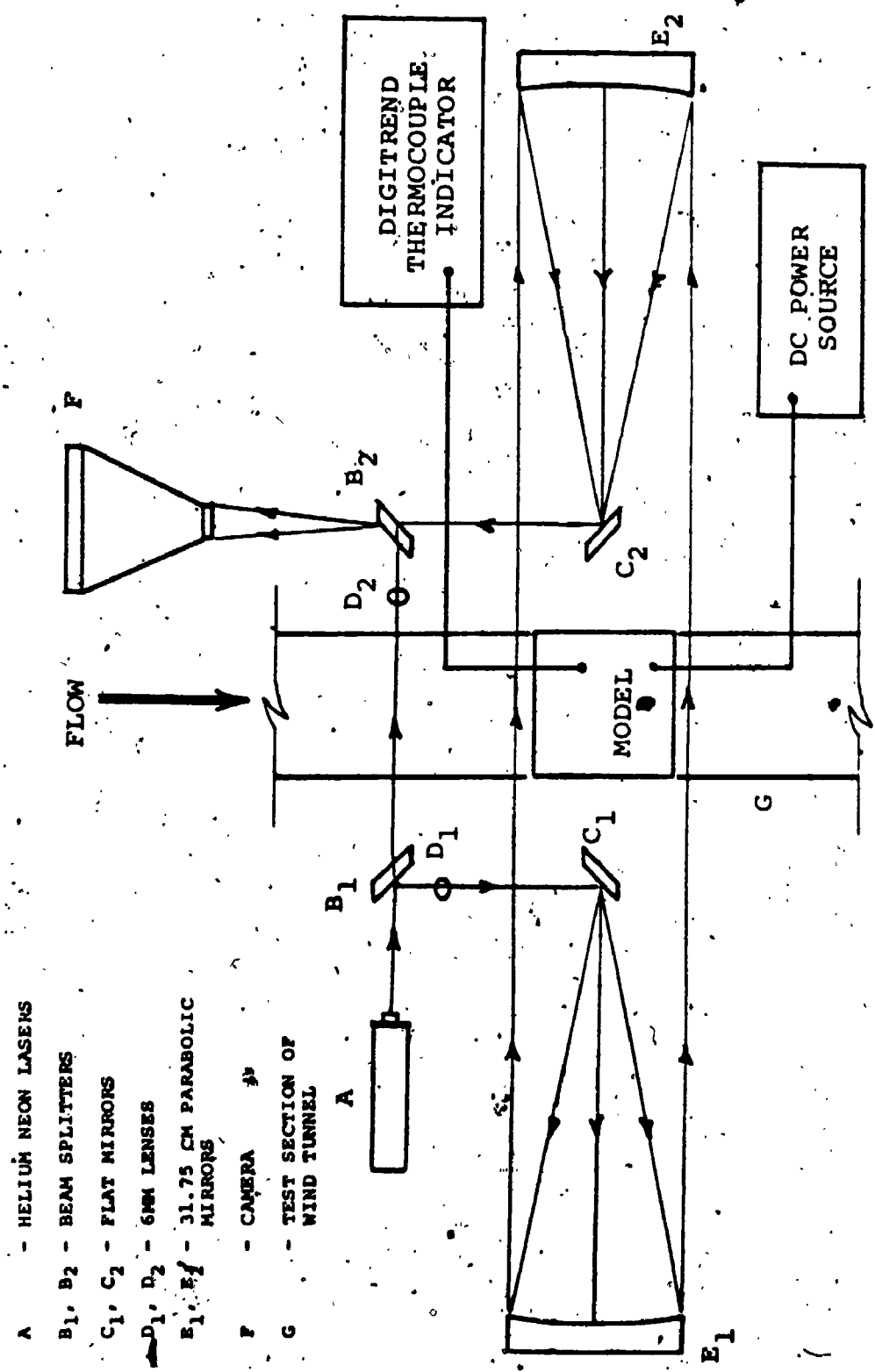


FIGURE 5.7 Experimental layout

and 254 cm focal length, mounted in such a way as to permit rotation about vertical and horizontal axes. C_1 and C_2 were two plane elliptical mirrors.

All the components of this interferometer were mounted on a 640 cm long, 20.32 x 30.32 cm wide flange I-beam. The I-beam was filled with concrete and was supported at four points on concrete pillars in sandboxes. Pneumatic air sacs were used between the I-beam and the concrete pillars to minimize floor and wind tunnel vibrations. Later, another set of these concrete pillars in sand was added. The mounts for mirrors E_1 and E_2 were bolted onto the I-beam. The other optics B_1 , B_2 , D_1 , D_2 , C_1 and C_2 were mounted on an optical support that permitted translation of these individual components. Vertical and horizontal rotations of the laser mount permitted an accurate beam alignment.

5.4 DESIGN AND CONSTRUCTION OF THE MODEL

The design of the experimental set-up had to incorporate the changes of parameters such as Rayleigh number, aspect ratio for plane enclosed gas layers and the Reynolds number in the wind tunnel, all over a suitable range of values. Randall [2], Mull et al. [29] and Arnold et al. [74] have all shown that the width in an enclosure has very little effect on the heat transfer

rates by natural convection. Thus, a variation of the width was not considered necessary.

The test section, as shown in Figure 5.8, consisted essentially of two parallel plates, a hot copper plate and a cold lexan plate with provision for keeping the hot plate at constant isothermal temperatures. The temperature of the cold plate was not controlled. The cold temperature depended on the temperature of the hot plate, the distance between the two plates and the effect of external cooling (the Reynolds number). This provision approximated the actual conditions of a solar collector where the coupling effect between the forced convection outside the glazing and the natural convection inside the cavity dictate the temperature distribution of the cold plate.

The height of the air layer was varied in the experiment obtaining various aspect ratios. This was accomplished by the design of four bolted legs which supported the hot plate. This plate was easily adjusted to various heights to provide a selected aspect ratio. The aspect ratios covered in this investigation were 8.85, 11.80, 17.7 and 35.40. The adjustable supporting legs and the assembly of the model are also shown in Figure 5.9.

This assembly of hot and cold plates was placed in

Gold Plate

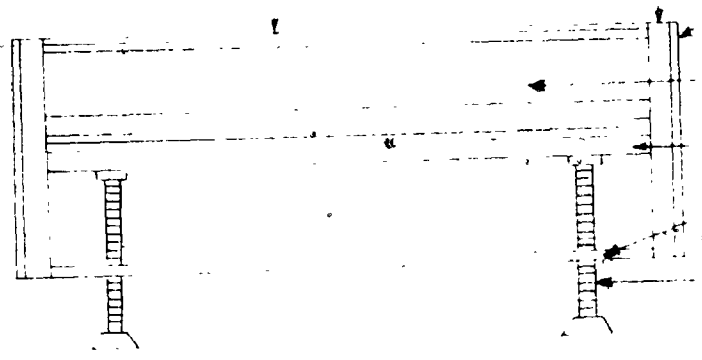


FIGURE 5.8 Two-Dimensional Schematic Diagram of the Model

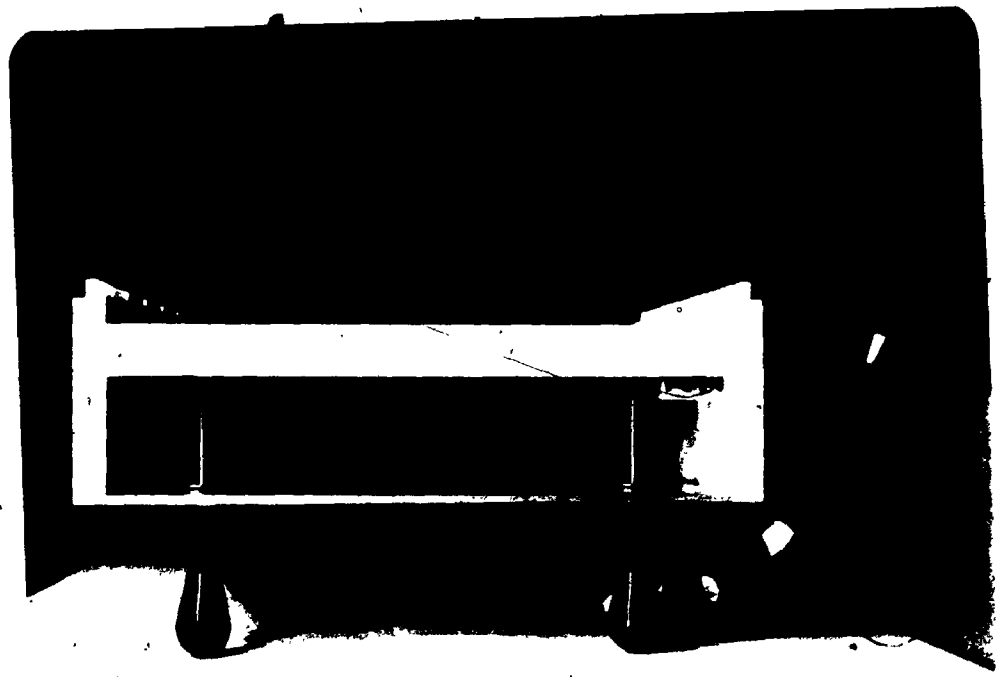


FIGURE 5.9 The Model With Adjustable Supporting Legs

a box made of two opposing opaque vertical walls constructed from two plates, a 1.27 cm thick insulating teflon plate and a 0.635 cm thick aluminum plate for rigidity. The other two opposing vertical walls of the enclosure were constructed from 1.27 cm thick transparent Perspex, onto which were mounted two 15.24 cm diameter, 2.54 cm thick optical flats, with both sides optically ground to within one tenth of one wavelength of visible light. Two strips of Perspex were also fastened perpendicularly to the bottom of the side walls where the box was positioned and could be moved. The Perspex side walls acted as an observation window as well.

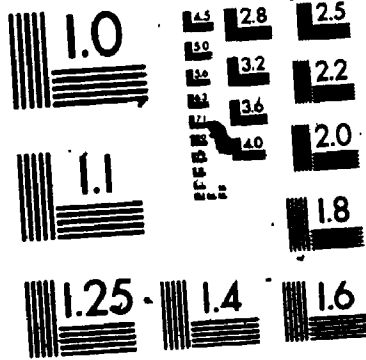
The 15.24 cm diameter optic flats and the 44.96 cm length of the model required that the test apparatus be shifted four times. This was attainable by incorporating an attached crank-shaft to one aluminum side of the vertical wall of the model and attaching three exact dimension acrylic strips to the sides of the cold plate. When the model required shifting, an acrylic strip was removed from one side of the model, the assembly was then relocated by the crank-shaft and the strip was placed on the other side. The top of the cold plate and the three strips of acrylic were flashed into the floor of the wind tunnel. The cavity was mounted below, exterior to the working section floor of the wind tunnel.

5.4.1 Hot Plate Assembly

The hot plate assembly, shown in Figure 5.10, was made of a copper plate, two aluminum plates and a Teflon insulating plate. The copper plate was 45.72 cm wide, 44.96 cm long and 1.27 cm thick. Fastened to the bottom of the copper plate were two 0.635 cm thick aluminum plates with the same dimensions. In the lower aluminum plate, grooves were machined to accept insulated nichrome heating wires of 18.30 m in total length. Provision was made to connect the three wires in parallel for better isothermal heating. The fourth wire was placed close to the four edges of the plate, to act as an edge guard heater. The constancy of temperature of the copper plate was achieved without using the guard heater. Good thermal contact was attained by applying silicon heat sink compound between the grooved aluminum and copper plates. An insulating Teflon plate 1.27 cm thick was fastened to the bottom of the aluminum plates to prevent heat losses. Power was supplied to the heating wires by a variable D.C. power source.

The surface temperatures of the copper plate were measured by means of 29, 28 gauge copper-constantan thermocouples. Each thermocouple was carefully fitted into a copper pipe having an outside diameter of 3.175 mm,

2



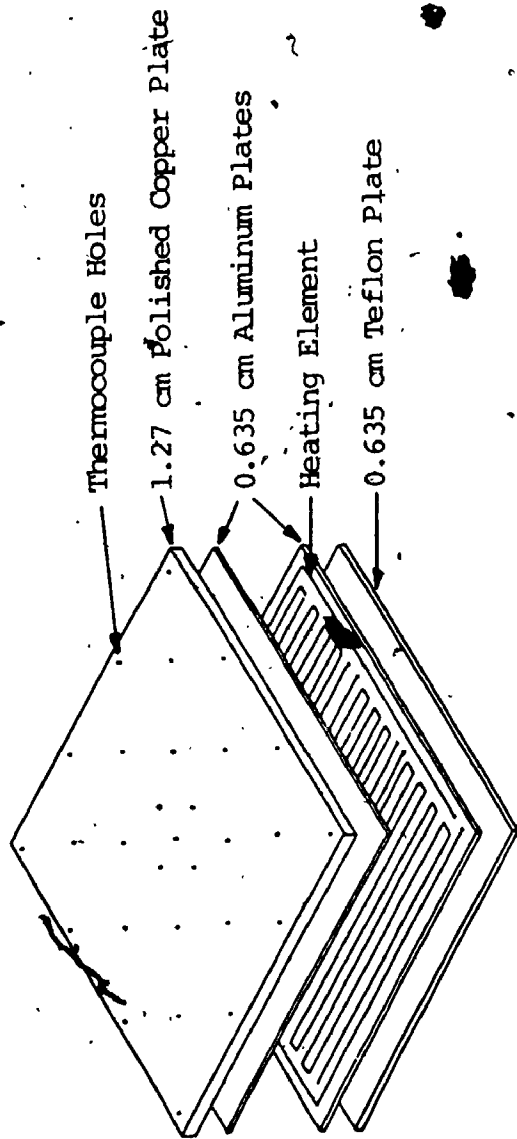


FIGURE 5.10 Exploded view of the Hot Plate

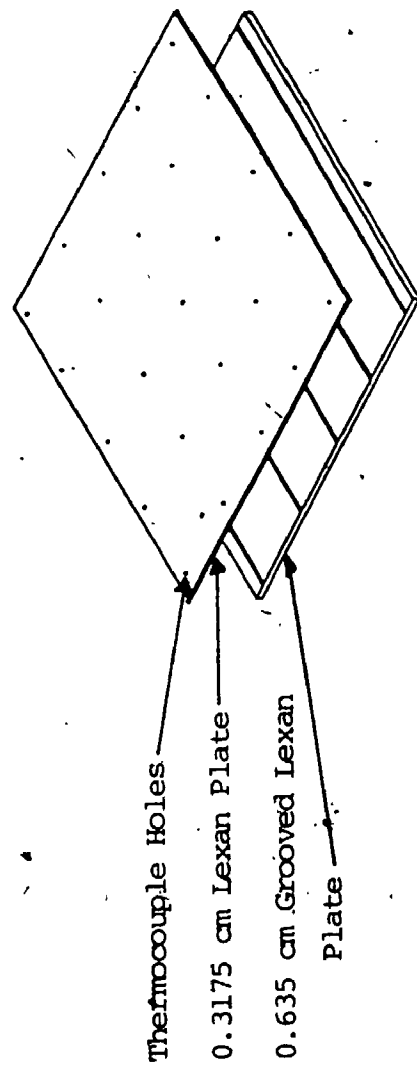


FIGURE 5.11 Exploded view of the Cold Plate

an inside diameter of 2.032 mm and a 9.525 mm length. The inside diameter was reduced to 0.762 mm on the top where the thermocouples were soldered to the pipes and mechanically fitted to the drilled holes on top of the copper plate. All the thermocouples were then tested for accuracy and consistency. The top of the copper plate was then highly polished to minimize the influence of radiation in the transfer of heat to the cold plate.

The thermocouple readings were recorded by a Doric Digitrend 220 automatic recorder. The Digitrend was capable of recording up to 100 thermocouples, and printing two per second with an accuracy of $\pm 0.4^{\circ}\text{C}$.

5.4.2 Cold Plate Assembly

The cold plate, shown in Figure 5.11, was constructed from two plates of polycarbonate plastic called Lexan, 45.72 cm wide and 44.96 cm long with two different thicknesses, 0.317 cm and 0.635 cm. The thicker plate was grooved to allow for the installation of thermocouple wires. The thermocouples, after passing through the grooves, were inserted into 0.762 mm holes to record the surface temperatures of the top and bottom of the cold plate assembly. There were 15 thermocouples on each side. A thermal contact compound, Dow Chemical type 732, with the same thermal conductivity as Lexan, was used to fill the grooves and provided good

thermal contact between the two Lexan plates.

Lexan was selected because of the similarity of its thermal conductivity to that of glass, as well as its widely accepted use as a glazing for solar collectors. Properties of the Lexan also made it possible to attach the thermocouples, which record surface temperatures, in a way which would cause no disturbance to flows inside or outside of the cavity.

For the above arrangement of equipment it was observed that:

- a) Tunnel velocities of 0.0 m/s to 2.3 m/s were possible.
- b) Vibration effects were important for velocities beyond 1.7 m/s and one datum was recorded beyond this region.
- c) The isothermal heated surface could be maintained to within 1°C for plate temperatures up to 90°C .
- d) The temperature differentials across the collecting cavity could be varied from zero to a maximum of 45°C .
- e) The aspect ratio was easily altered to 8.85, 11.80, 17.70 and 35.40.
- f) Tilt angle could be changed from 0° to 60° with respect to the horizontal, and finally
- g) Interferograms of adequate quality were attainable.

CHAPTER VI

EXPERIMENTAL METHODS AND PROCEDURES

6.1 OPERATING PROCEDURE AND MEASUREMENTS

By far, the most difficult task in this investigation was the alignment of the wind tunnel, the interferometer, and the model. The adjustment of one of the above consequently required the adjustment of the other two. It was imperative that the experiment be conducted under vibration free conditions. Therefore, it was necessary to examine each part of the apparatus individually before any actual data were taken. In this chapter, each section of the apparatus is described separately and problems encountered in making essential experimental measurements are discussed.

6.1.1 THE WIND TUNNEL

Since the wind tunnel was placed on some twenty pneumatic air sacs, the pressures in the air sacs required careful adjustments in order to provide a horizontal working section. This adjustment also adjusted the cold surface of the model.

The preliminary tests in the tunnel indicated excessive and undesirable levels of vibration which resulted in unattainable interferograms. This was resolved by

designing an assembly with four vertically adjustable legs, with plates at one end and bushings with 1.27 cm diameter steel rods at the other. The legs were designed adjustable for the future study of the model, when it would be required to tilt the model and the working section of the tunnel. The plates were positioned on air sacs in order to provide supports for the section and to minimize the vibrations. The bushings were fastened to the bottom of the section to enable the model to be tilted at various tilt angles with respect to the horizontal axis. The assembly was then adjusted to an exact horizontal position by regulating the pressure in the air sacs. Both the wind tunnel motor and the fan were lubricated as often as required for smooth operation and to minimize vibrations.

A desired air velocity in the tunnel was attainable by adjusting the flow velocity control on the motor. The velocity was then kept constant throughout each set of experiments. The flow temperature inside the tunnel and the room temperature outside of the tunnel were measured and recorded by the Digitrend thermocouple indicator. The pressures inside the working section, behind the test model, were measured by using the Scanivalve system integrated to a Barocel pressure transducer (Datametric Inc., Type 590D). All the static tubes were connected

in parallel to the reference side of the transducer.

For all of the experiments, air at atmospheric pressure and temperature was used as the cooling fluid. The air temperature in the room adjacent to the laboratory from which the air was drawn and exhausted, was kept constant within a maximum of 1°C for the duration of each individual experiment.

6.1.2 The Interferometer Alignment

As was mentioned before, since the interferometer could not tolerate an excessive vibration caused by the building and the wind tunnel, another sandbox with concrete pillar and air sacs was added under the heavy I-beam which supported the interferometer. This greatly reduced the level of vibrations transmitted to the interferometer.

To facilitate the alignment of the interferometer, the following steps were taken:

1. The I-beam was horizontally adjusted such that the interferometer was perpendicular to the air flow in the wind tunnel working section.
2. The laser tube (A), (see Figure 5.7), was horizontally aligned such that the light beam passed through the two beam splitters (B_1 and B_2).

3. The expanding lens (D_1) was removed from the path of the beam. The beam splitter (B_1) and the plane mirror (C_1) were adjusted so that the test beam was centred on the parabolic mirror (E_1).
4. The lens was moved back into the path of the beam, (B_1) and (C_1) were adjusted to centre the expanded beam on (E_1).
5. The parabolic mirror (E_1) was adjusted so that the horizontal expanded beam passed through the test model and was centred on the parabolic mirror (E_2).
6. The parabolic mirror (E_2) was adjusted so that the reflected beam was centred on the plane mirror (C_2).
7. The plane mirror (C_2) was adjusted such that the reflected beam was centred on the beam splitter (B_2) and passed through a shutter onto the screen of camera (F).
8. The expanding lens (D_2), the plane mirror (C_2) and the parabolic mirror (E_2) were adjusted so that the reference and the test model beams intersected on the side of (B_2) facing the laser light source. When this was achieved, an interference pattern was attainable on the screen. This could not occur if the interferometer was subjected to vibrational disturbances.

At this time, the interference pattern in the form of an infinite fringe field was possible by fine tuning of E_2 , C_2 and B_2 . A method was developed and used throughout all the experimental testing by which a fast transition from an infinite fringe field to a finite fringe field and vice versa was possible. It involved rotating the parabolic mirror (E_2) about its vertical axis which changed the fringe spacing and again rotating (E_2) about the horizontal axis which in turn rotated the fringes to any desired angle. The reversed procedure was applied for returning to the original infinite fringe field. The procedure, which took approximately one minute made it possible to obtain two interferograms on the same negative film. After the first interferogram was taken, the proper adjustment was made, then the film holder was rotated by 180° before the second interferogram was obtained. During this period the camera was not moved. For the analysis, interferograms with the finite fringe fields were used. Infinite fringe interferograms were taken to visualize the isotherms inside and outside of the enclosure.

The fringe fields from the long path Mach-Zehnder interferometer were recorded on Polaroid 4X5 Land Film, Type 55/positive-negative. The interferograms were taken

by a Calumet 10 cm x 12.5 cm view camera with its lenses removed. The focussing was accomplished by the interferometer optics. The interferograms were Panchromatic, Type B sensitization films with a negative resolution of 150 to 160 lines per mm. For best results, the shutter speed was always set at 1/125 second. During the two exposures of infinite and finite fringe fields, the power to the hot plate heating wires, the position of the cavity and the air velocity in the wind tunnel were kept constant.

Approximately one thousand interferograms with both fields were taken at four different heating rates. The air velocity in the tunnel was varied from zero to approximately 2.3 m/s for each heating rate. The length and the width of the model were kept constant, but the aspect ratio was varied from 8.85 to 35.40. Most of the interferograms were taken during night hours when the ventilation system was lowered and the building vibration disturbances were at a minimum. Two dehumidifiers were operating in the laboratory to remove excessive moisture from the air. They were turned off during the period when interferograms were taken.

The interferograms were set in a jig attached to a travelling microscope. Various locations with respect to the cavity edge on each set of interferograms were

vertically scanned in the enclosure from the hot plate to the cold plate. The location of the fringes was determined by setting the crosshairs of the eyepiece on the centre of the white fringe of the interferograms and recording their values. For determining the edge effects in the enclosure, three points close to each wall were scanned. The locations of each horizontal boundary on the hot and cold plates were also recorded. The travelling microscope was accurate to ± 2.5 microns. The scale factor was determined by traversing the height of the cavity between the hot and cold plates with the travelling microscope and comparing the value to the known height. The height of the enclosure was measured by a Vernier Caliper to the nearest 0.1 mm.

6.1.3 Positioning the Test Model

In order that the model could be shifted upstream or downstream the optical glasses were removed and the model assembly was moved to a proper location. After the cold plate was checked to be horizontal, the hot plate was moved up or down by the four supporting legs to provide a desired spacing from the cold plate. The height was measured to the nearest ± 0.1 mm by a Vernier Caliper at several locations within the enclosure. Overall spacing was estimated to be within ± 0.5 mm of the

nominal width.

The following procedure was used to make sure that a horizontal parallel light beam passed through the cavity of the model. After the light source was turned on, a very thin circular-cylinder was placed inside the enclosure, next to the walls and the resolution of the circular ends was checked on the screen. Also, before any interferograms were taken, a thin transparent paper was placed behind the model to ascertain the presence of the parallel and horizontal beam.

After the alignment was complete, the optical glasses were reinstalled. A smoke test was conducted for any possible air leaks in the enclosure which would disturb the two dimensional effect necessary for a good interferogram. The enclosure was lined on the two opposite ends with a thin soft rubber for a continuous fit along the optical flats and the working section walls of the wind tunnel to adequately seal the enclosure.

Since the optical glasses were 15.24 cm and the length of the cavity was 44.96 cm, the test model had to be moved four times for a complete scan. For advancing the test model, the two opposite sides of the tunnel had to be opened slightly. This was achieved by removing two heavy C-clamps holding the sides. The floor sections of the

wind tunnel on each side of the test model were made of Perspex sections which were bolted together. These sections were designed in such a manner that, for advancing the model, one could easily be removed from one side and after the advancement it could be placed on the other side of the model. Thus, always an equal movement of the test model was attainable throughout the experiment. Interferograms with finite and infinite fringe fields were taken for each section separately for the same boundary conditions.

6.2 DATA RECORDING PROCEDURES

After all of the above procedures were followed, the test model was moved back to the first section, where the thermal boundary layer on the surface of glazing starts with the forced convection on the surface of the glazing as shown in Figure 1.3. The bottom hot plate was gradually heated to a desired operating temperature by a Hewlett Packard 6443B DC power supply and the interferometer was set at infinite fringe field, as was described in section 6.1.2. It took approximately two to three hours before any steady state condition could be established. This was accomplished by monitoring the temperatures until they stabilized. The steady state conditions were assumed when the temperatures did not vary

by more than 0.1°C in a fifteen minute period. An interferogram was then taken with infinite and finite fringe fields for processing.

The temperatures of the hot plate, cold plate, the vicinity of the enclosure, the flow inside the wind tunnel and the room were measured and recorded. The temperatures of the hot plate remained isothermal to within $\pm 1.0^{\circ}\text{C}$ for the high heating rates but dropped to $\pm 0.2^{\circ}\text{C}$ for the low heating rates. At this time, because of the consistency of the isothermal hot plate, it was decided that the heating guard heater was not required. Consequently, it was not used during the course of this experiment. The temperature of the cold plate was never isothermal, as expected. The temperature peaked at the centre of the plate and decreased to lower values towards the edges for no flow conditions. The temperatures of the cold plate showed a dependency on parameters such as the height of the enclosure, the temperature of the hot plate and the exterior Reynolds number. The hot plate temperature distribution is illustrated in Figure 6.1 while the average temperature plots of the cold plate, along the width, perpendicular to the forced direction are presented in Figures 6.2 and 6.3. Due to the thermal boundary layer effect, the plate is colder at the leading edge of the boundary layer where there is less thermal resistance to heat



FLOW DIRECTION

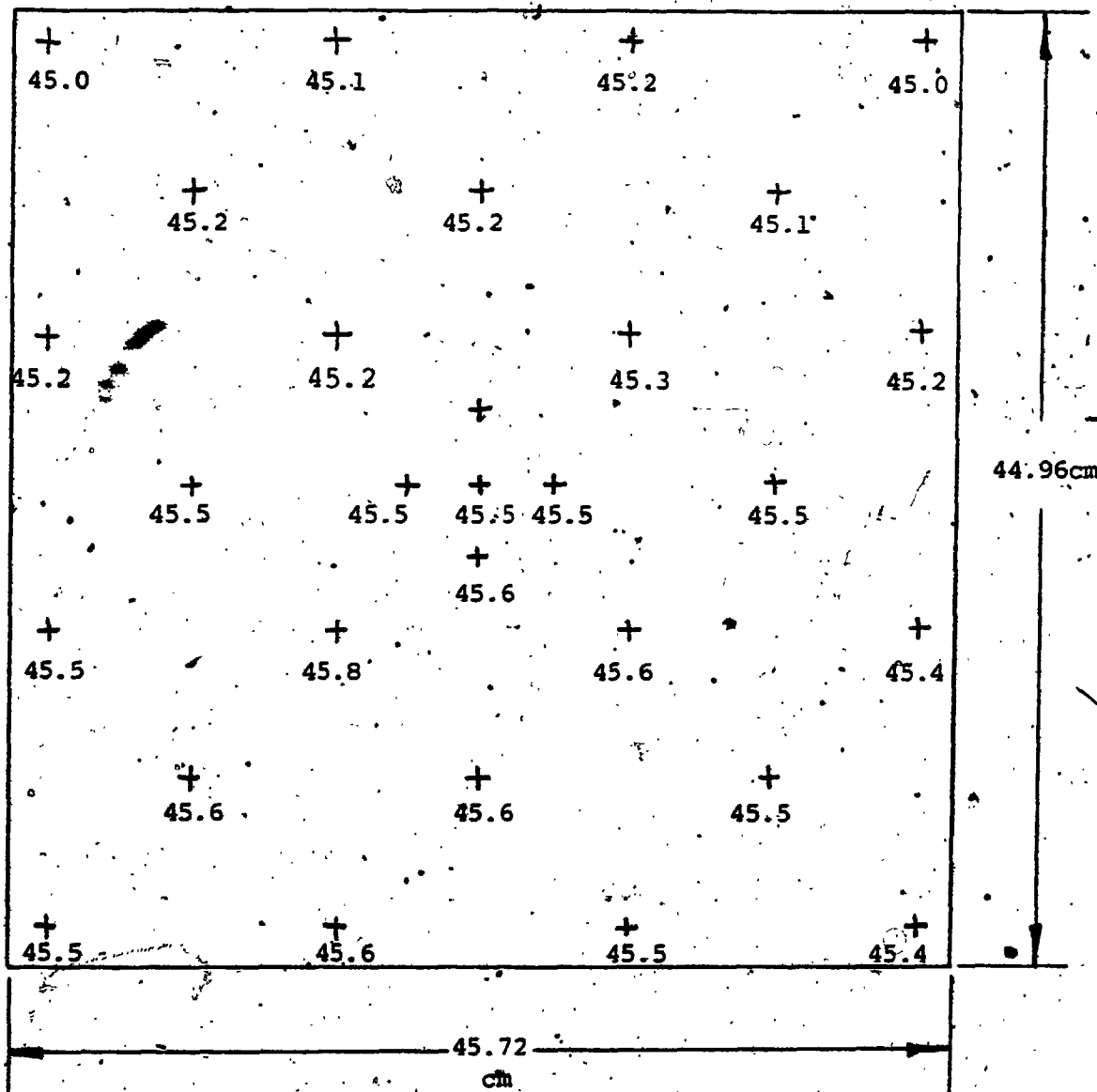


FIGURE 6.1 Temperature Distributions in Hot Plate

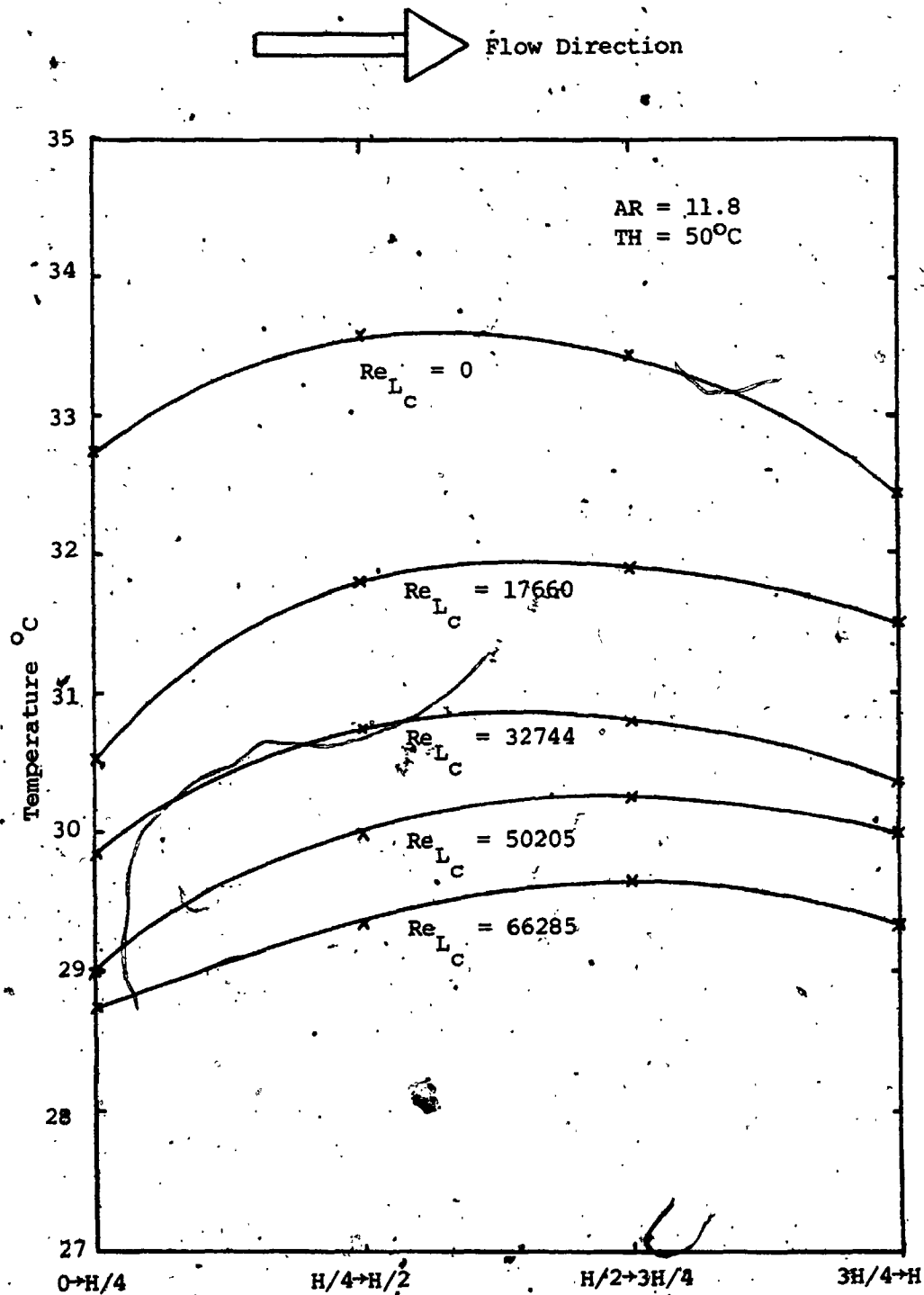


FIGURE 6.2 The Average Cold Plate Temperature Drop Profile for the Top of the Cold Plate Due to Forced Convection Thermal Boundary Layer Effect

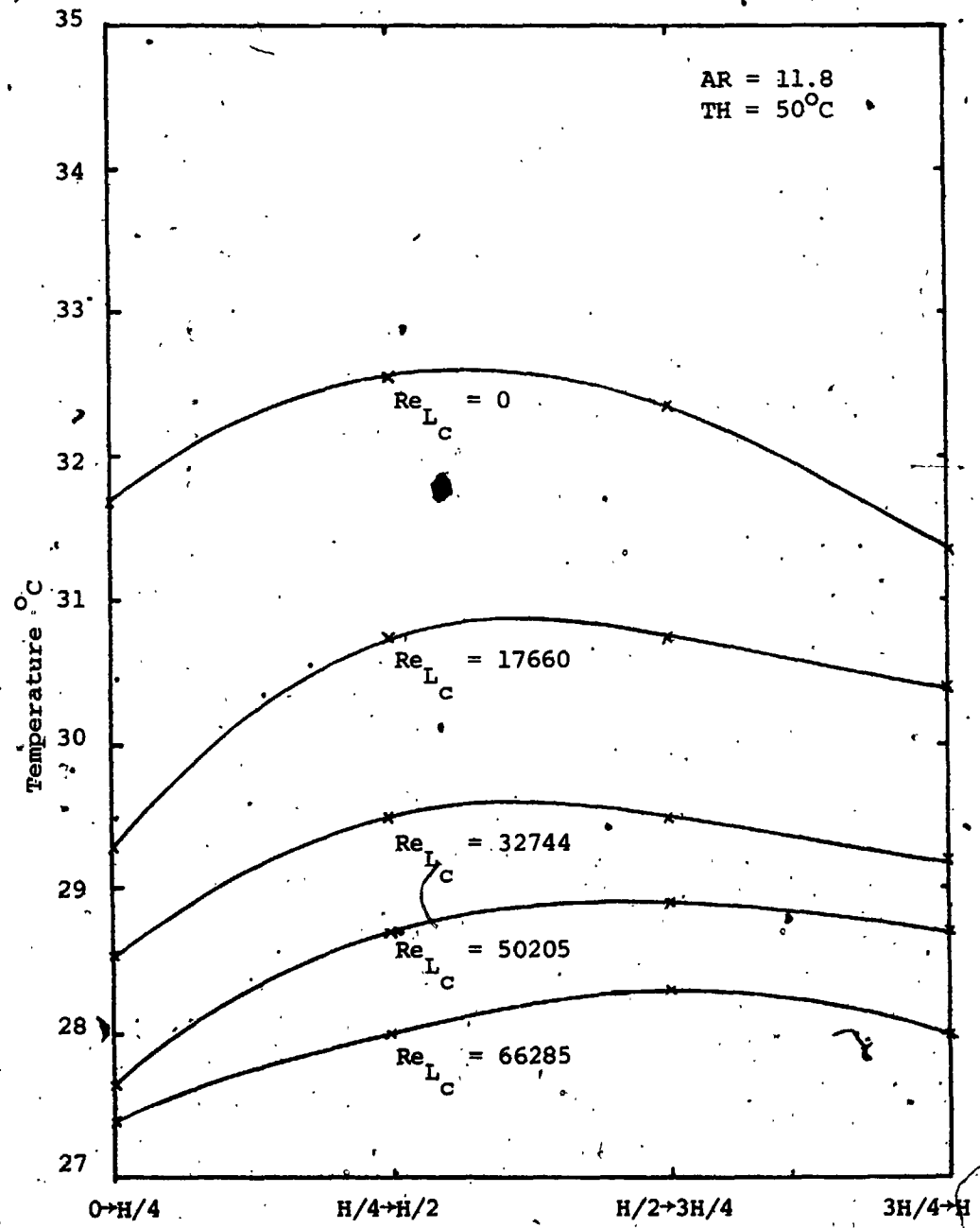
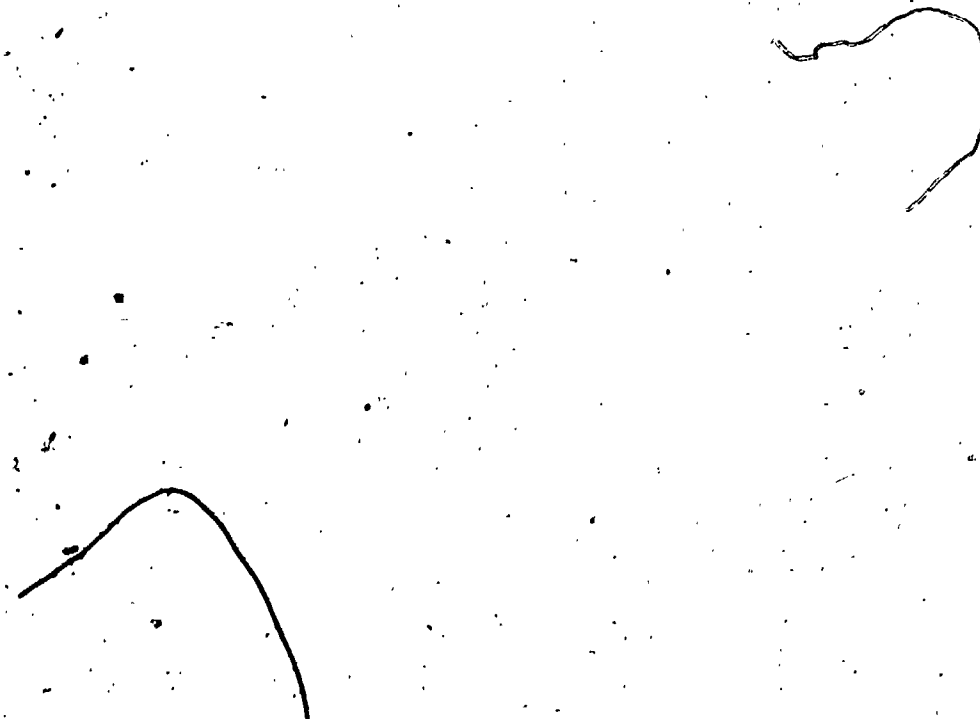


FIGURE 6.3 The Average Cold Plate Temperature Drop Profile for the Bottom of the Cold Plate Due to Forced Convection Thermal Boundary Layer Effect

transfer. As the thermal boundary layer gets thicker on the plate, there is more thermal resistance to heat transmitted to the top fluid. This would result in a higher plate temperature.

The room pressure, the voltage and the current input to the test model were recorded. For each interferogram, a record was maintained of the test section temperatures, the flow velocities in the wind tunnel and the aspect ratios.

The test model was then advanced to the next section. A period of at least thirty minutes was required before the next interferogram could be taken. The procedure of the first section was then repeated for all subsequent sections.



CHAPTER VII
PRESENTATION AND DISCUSSION OF
EXPERIMENTAL RESULTS

7.1 INTRODUCTION

A long path difference Mach-Zehnder interferometric study was conducted on the natural convection heat transfer phenomena in horizontal, enclosed air layers. The bottom plate boundary was heated isothermally and the non-isothermal exterior of the top plate boundary was exposed to a surface air flow in a wind tunnel. Various parameters, given in Table 7.1, such as the bottom hot plate temperature, aspect ratio (length over height) and Reynolds number in the wind tunnel were considered. During the course of this investigation, the length (44.96 cm) and the width (45.72 cm) of the model were kept constant at all times.

As mentioned in Chapter II, the literature survey, the extent of this study deals with three major natural and forced convection heat transfer problems. In order to obtain an overall understanding of the present investigation, the results are also presented in the same order as in Chapter II. First, the results related to the Benard cells are considered. Secondly, the results of the total horizontal enclosure and finally the forced convection

TABLE 7.1 Range of Nominal Values of Parameters

Air Layer Thickness (cm)	1.27	1.91	2.54	3.81	5.08
Aspect Ratio	35.40	23.60	17.70	11.80	8.85
Hot Plate Temperature, °C	30	50	70	90	
Reynolds Number	0 - 6.6×10^4				
Rayleigh Number	1.0×10^3 - 3.27×10^5				

on the surface of a horizontal plate are discussed.

7.2 CELLULAR CONVECTIVE MOTION (BENARD CELLS)

A dimensionless parameter describing the ratio of convective heat transfer to viscous forces is defined by the Rayleigh number; this can be written as

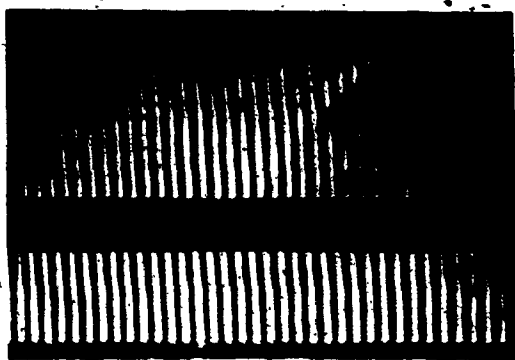
$$Ra = \frac{g\beta\Delta TL^3}{\nu\alpha}$$

This parameter is important in an enclosure for any geometry where natural convective motion occurs. Its magnitude determines the onset of natural convection and the nature of the flow. The numerical value for this condition is called the critical Rayleigh number and the value varies for different geometries and boundaries, as discussed in Chapter III. For $Ra < Ra_{crit.}$, the flow is called stable and heat is transferred only by conduction. In this case, the Nusselt number is unity. If $Ra > Ra_{crit.}$, then convective currents occur and heat is transmitted by natural convection. In this case, the Nusselt number is greater than one. The magnitude of the Rayleigh number indicates the strength of the convective motion in the form of cellular currents called Benard cells, as shown in Figure 7.1.

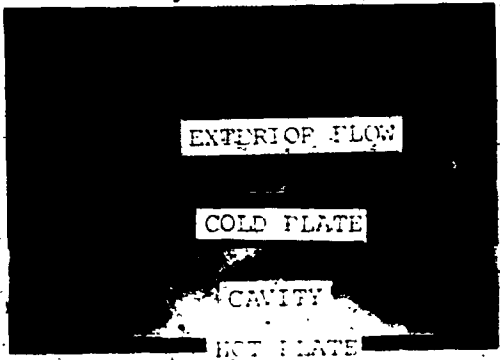
A sequence of interferograms are illustrated in Figures 7.2 to 7.4, with finite fringe fields on the



FIGURE 1.1 Two-dimensional color image of a surface with a wavy texture. The image is a scan of a document page.



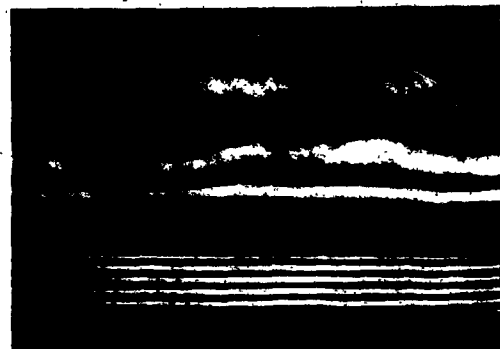
(a)



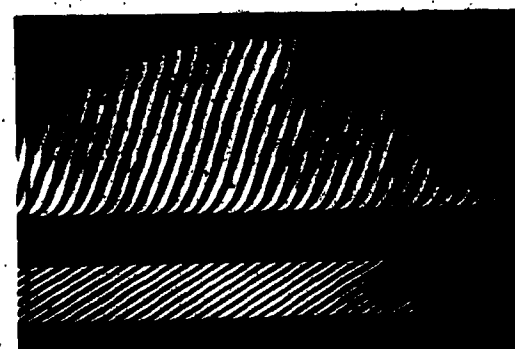
(b)



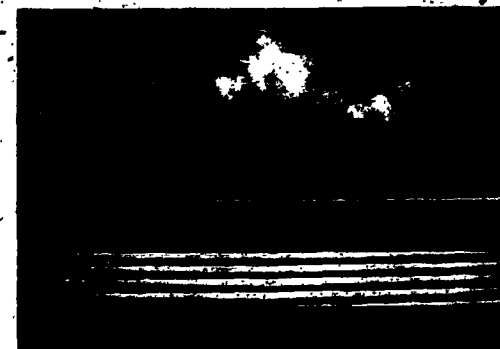
(c)



(d)



(e)



(f)

FIGURE 7.2 Sequence of Interferograms With Finite Fringes for Analysis and Infinite Fringes Showing Isotherms in Test Sections; for a & b $Re=0$, $Ra=0$; for c & d $Re=0$, $Ra=1390$; for e & f $Re=50680$, $Ra=1543$

left-hand side, and the corresponding infinite fringe fields on the right-hand side. In these interferograms, the two distinct heat transfer regions, separated by the top and bottom boundary plates, are clearly defined. Figures 7.2a and 7.2b are interferograms taken with no temperature difference between the top and bottom plates. In Figure 7.2a, the straight fringe field indicates a uniform temperature field, while in Figure 7.2b the uniform temperature field is shown as an interferogram with no fringes. Figures 7.2c and 7.2d illustrate shifted fringes and isotherms respectively when a temperature variation is imposed on the fluid inside the cavity. These fringes and isotherms are equally spaced. Fringes which are straight lines indicate that no convection is taking place ($Re = 0$ and $Ra = 1390$). Up to this point, the critical Rayleigh number has not been achieved in the enclosure. On the surface of the cold plate, natural convection is indicated by the shifted fringes and the isotherms near to the plate respectively. Forced convection on the surface of the top boundary is shown in Figures 7.2e and 7.2f where $Re = 50680$ and the bottom plate temperature was kept the same as c and d. Because of the coupling effect of the forced convection, the Rayleigh number inside the enclosure has been increased from $Ra = 1390$

to $Ra = 1543$. Again, straight linear fringes indicate that there is no natural convection occurring in the cavity.

Figures 7.3a and 7.3b illustrate that shifted fringes are no longer straight or linear. This is an indication that the critical Rayleigh number has now been exceeded ($Re = 0$ and $Ra = 1882$). The formation of the two-dimensional convection Bénard cells are shown in Figure 7.3d. The sinusoidal patterns of the isotherms indicate the direction of the fluid flow. When the fringes (isotherms) are concave downwards (peak), warm air moves upward where there is heat transfer to the top boundary (cold plate). At this point the flow moves laterally and becomes colder (more dense). The downward flow is demonstrated by concave upward (trough) isotherms. The flow is then lateral along the hot surface opposite to the direction along the cold plate, where the air gets warmer (less dense) and moves upward. Thus, the circulation pattern is a closed cell, in longitudinal rolls between the bottom and top plate of the cavity. The non-linear finite fringes in Figure 7.3c indicate that convection heat transfer is taking place. As the Rayleigh number was increased further, two distinct modes of heat transfer became apparent and these can be seen in

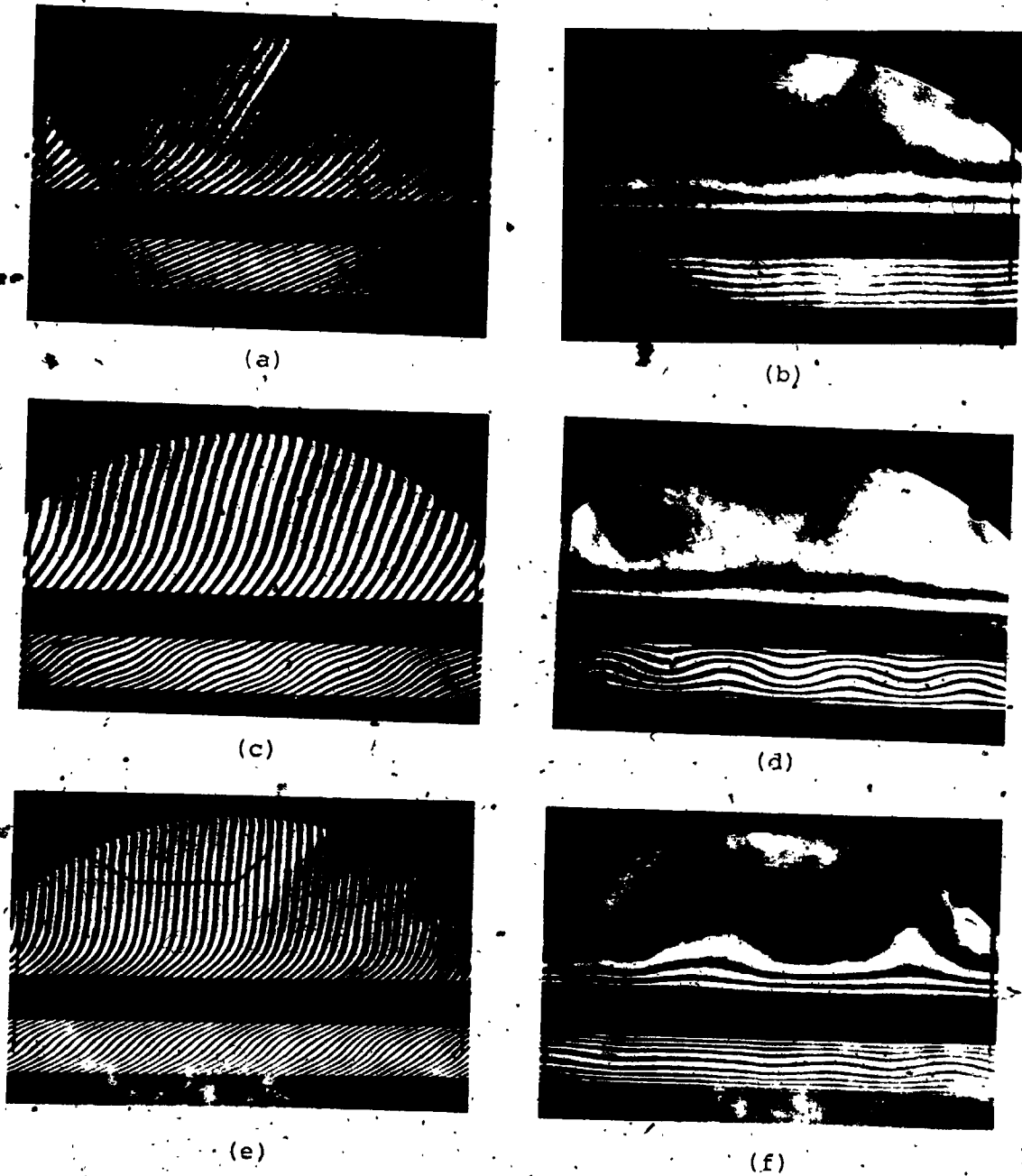


FIGURE 7.3. Sequence of Interferograms With Finite Fringes for Analysis and Infinite Fringes; Showing Isotherms in the Test Sections; for a & b $Re=0$, $Ra=1882$; for c & d $Re=0$, $Ra=2167$; for e & f $Re=0$, $Ra=2676$

Figures 7.3e, 7.3f, 7.4a and 7.4b. In the interferograms with infinite fringe fields, isotherms are straight, horizontally concentrated near the plates and are separated in the central regions. This indicates heat conduction near the surface of the plates, with a low velocity cellular convection flow in the central region. The distance away from the plates where the conduction took place was approximately $1/4$ of the total height from each horizontal boundary. This phenomenon occurred at about $Ra = 2500$. Figures 7.3a to f and 7.4a and b illustrate the natural convective motion on the surface of the top boundary (the cold plate), while Figures 7.4c to f show interferograms with forced convection due to the wind tunnel air flow over the surface of the cold plate. The aspect ratio for all the interferograms shown was 25.40 except Figures 7.4e and f, where it was 17.70. As the Rayleigh number increased, it was suspected that the Bénard cells moved from two-dimensional to three-dimensional form. This is illustrated in Figures 7.4e and f with $Re = 65054$ and $Ra = 23789$. The central region isotherms (convection region) shown in Figure 7.4f were no longer stable, but the isotherms near the horizontal boundaries (conduction regions) remained stable. This phenomenon occurred at about $Ra = 23000$.

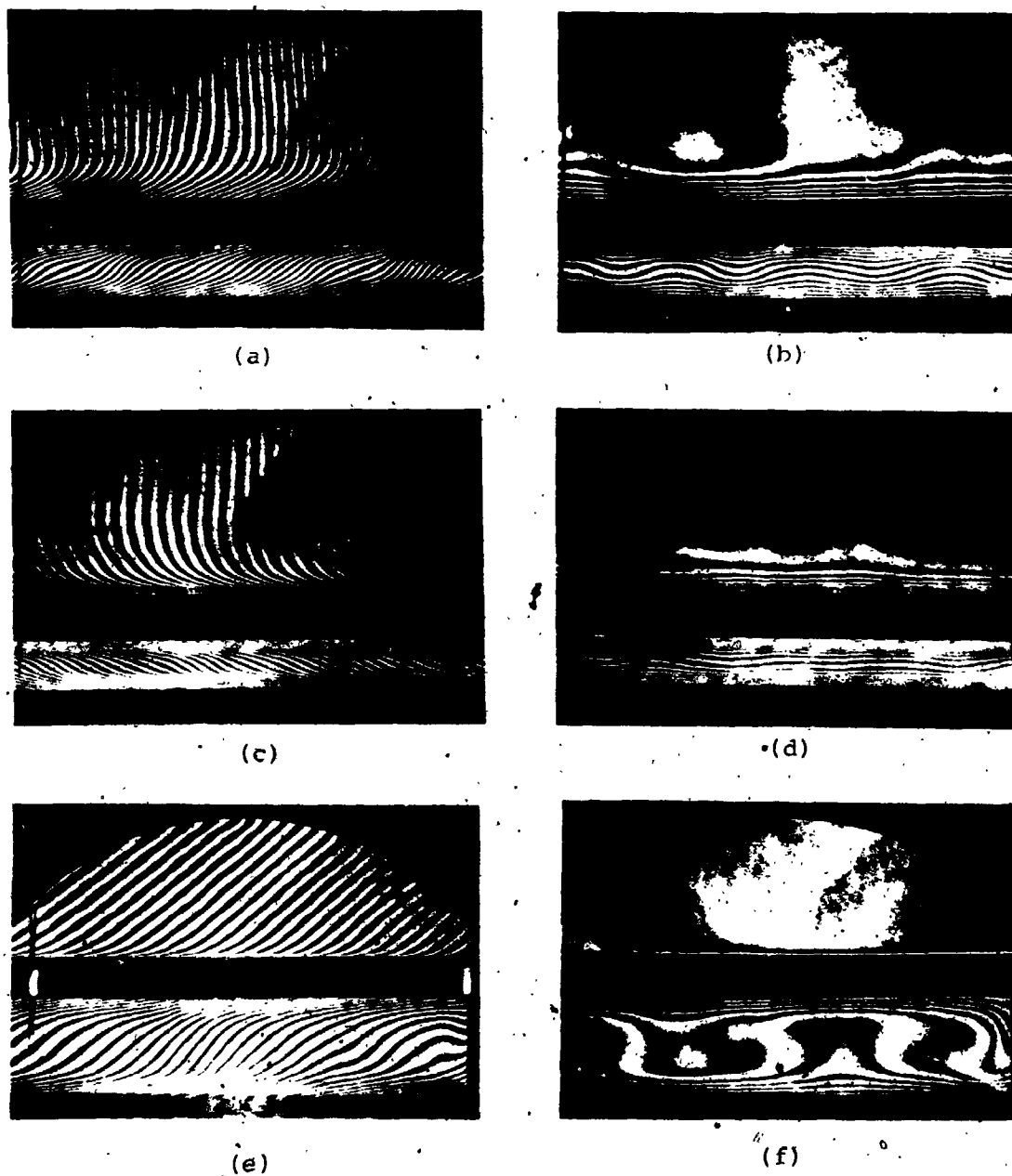


FIGURE 7.4 Sequence of Interferograms With Finite Fringes for Analysis and Infinite Fringes Showing Isotherms in Test Sections; for a & b $Re=0$, $Ra=3521$; for c & d $Re=32709$, $Ra=4332$; for e & f $Re=65054$, $Ra=23789$

7.2.1 Non-Dimensional Temperature Profile For the Benard Cell.

The interferograms with finite and infinite fringe fields were examined at the same scanning positions for purposes of plotting the temperature profiles. The results appeared to be identical. Infinite fringe interferograms were not used for such plots since the horizontal boundary was difficult to accurately plot. Thus, only the interferograms with finite fringe field were utilized for analysis to plot the temperature profiles.

Figure 7.5 demonstrates a plot of non-dimensional vertical temperature profile of Figure 7.2c, with six horizontal locations as shown. See Chapter I for a definition of the nomenclature. The linear temperature profiles indicate a conduction regime, as expected, since the Rayleigh number is less than the critical Rayleigh number. As was mentioned, in the state of pure conduction the fringes, both finite and infinite, are parallel and equally spaced. In this case, although the fluid flow is thermally induced, the instability does not occur until the critical Rayleigh number is reached. The temperature profiles after the onset of natural convection, when $Ra > Ra_{crit.}$, is shown in Figure 7.6. When the critical Rayleigh number is reached, the temperature profiles are no longer linear. They appear as a

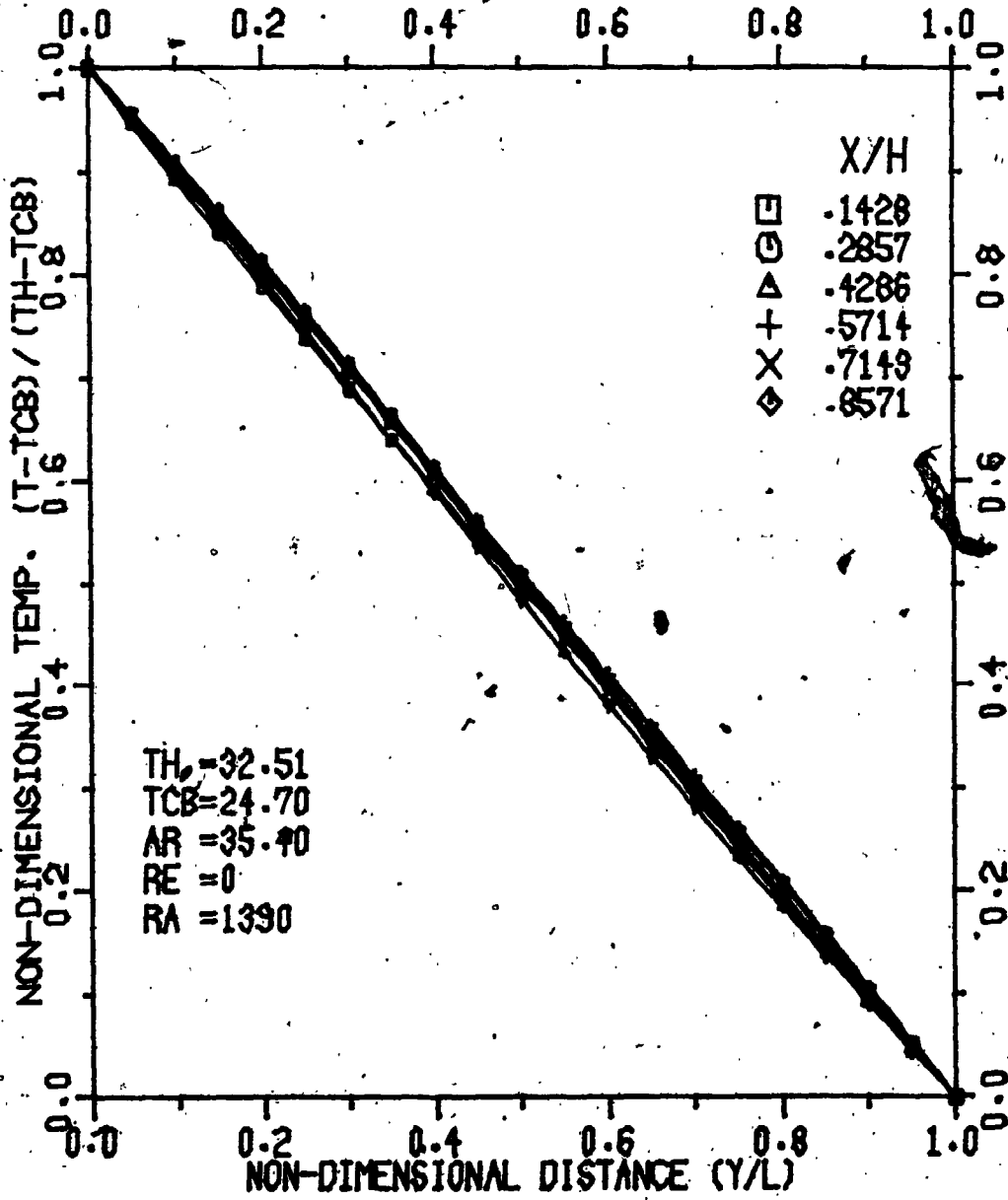


FIGURE 7.5 Experimental Vertical Temperature Profile in the Cavity

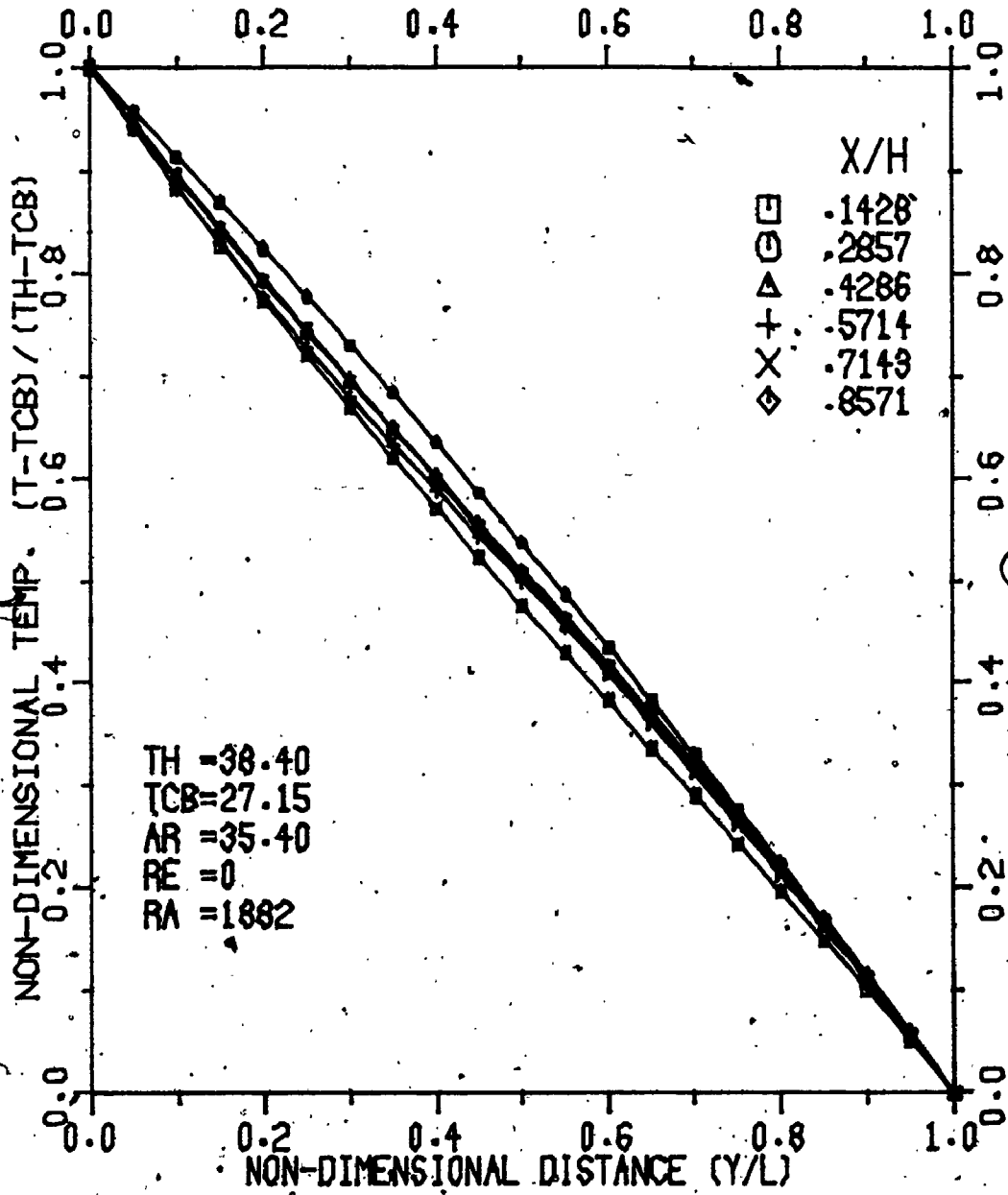


FIGURE 7.8 Experimental Vertical Temperature Profiles in the Cavity

sinusoidal pattern in the infinite fringe field. As the Rayleigh number was increased, the nonlinearity of the temperature profile became more pronounced. This is shown in Figure 7.7 which is information processed from the interferogram of Figure 7.4c. As the Rayleigh number was further increased the temperature profiles, in the central region, became reversed. This is due to the fact that when the hot air moves upward it does not have sufficient time to transmit the energy to the air layers in the conduction region adjacent to the cold surface; thus, this warm air flows laterally and then downward. The same analysis holds for the air moving down and along the bottom plate. There is insufficient time for transfer of the maximum possible heat from the hot plate. This results in an increase of air rotation but in a reduction in the overall heat flux. Figure 7.8 illustrates the temperature reversal in the enclosure.

For all the temperature profiles, the slopes at the horizontal boundaries are negative. The temperature gradients near the hot and cold boundaries are shown in Figure 7.9. In this figure, the temperatures of upflow, downflow and mid-cell are also shown. As the Rayleigh number increased, the negative slopes became

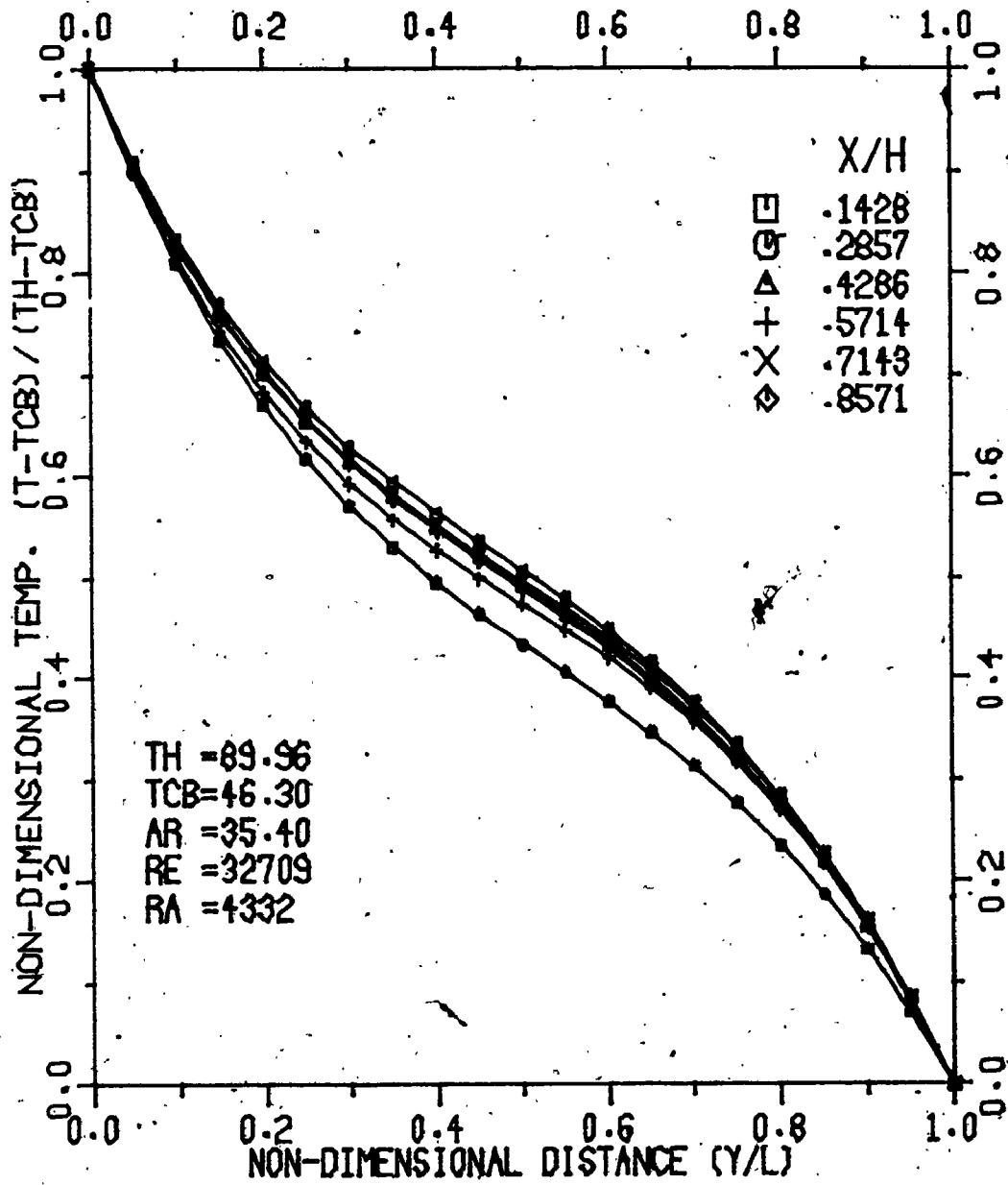


FIGURE 7.7 Experimental Vertical Temperature Profile in the Cavity

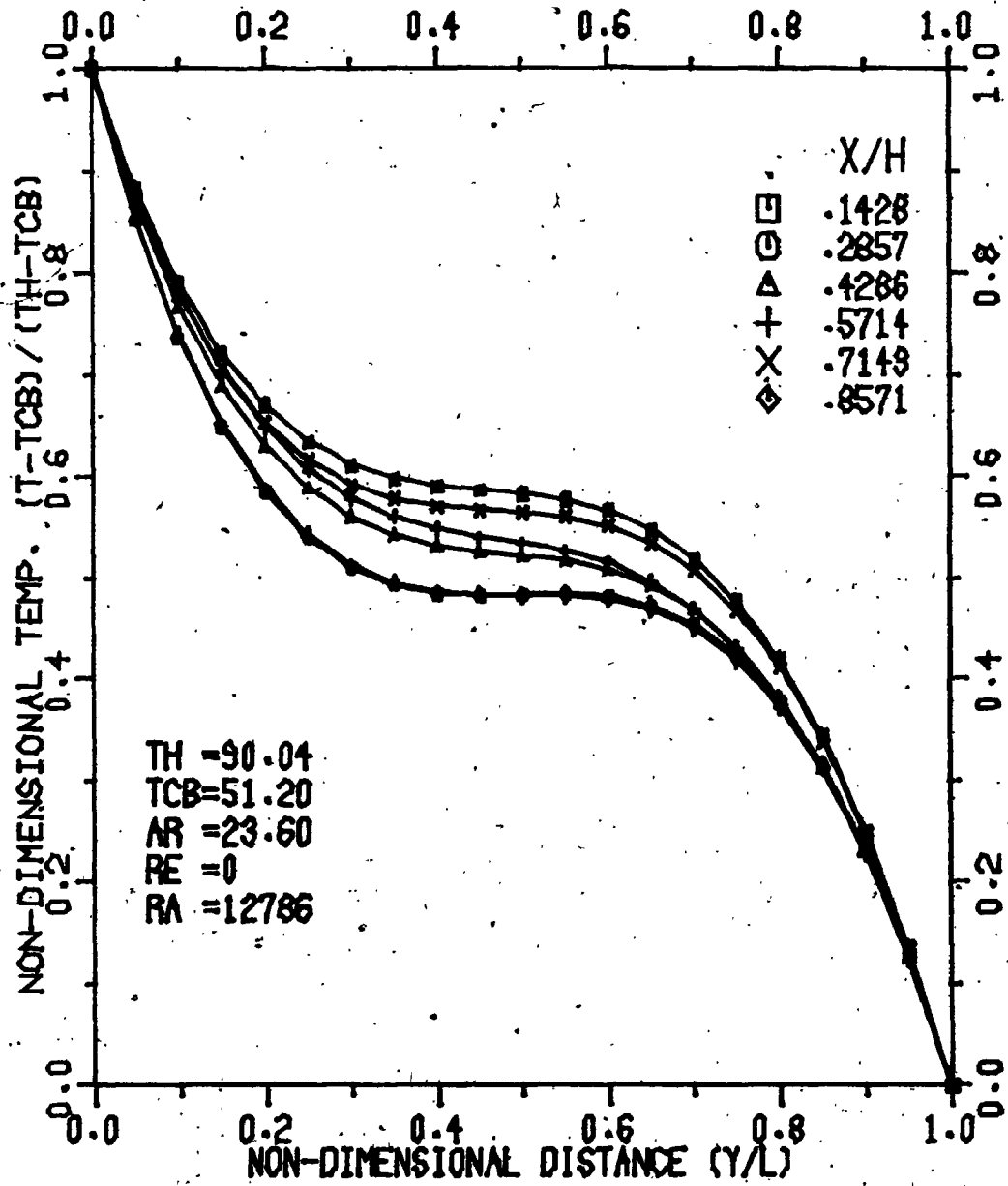


FIGURE 7.8 Experimental Vertical Temperature Profile in the Cavity

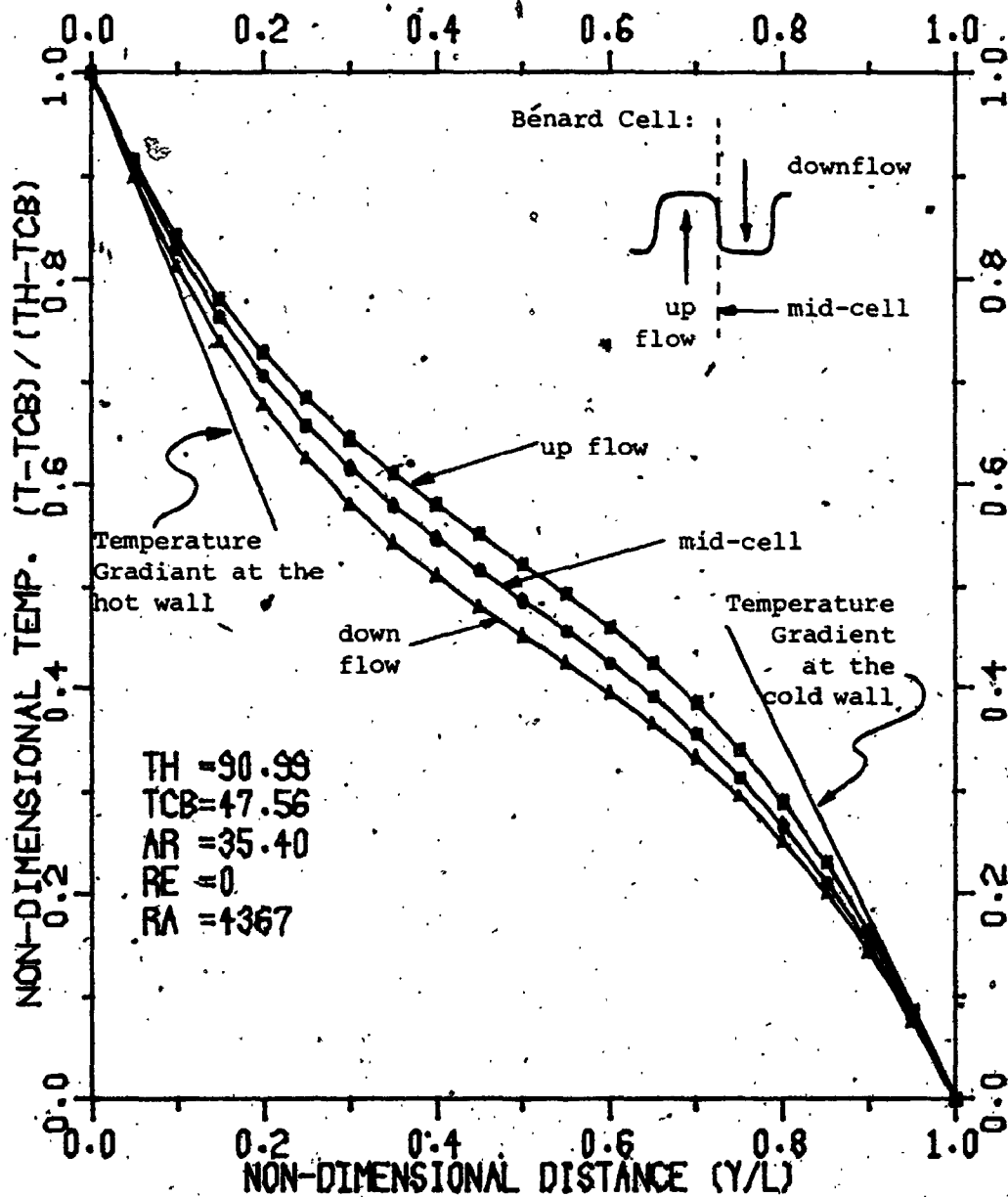


FIGURE 7.9 Experimental Vertical Temperature Profile in the Cavity, showing Upflow, Mid-cell and Downflow in a Bénard Cell, as well as Temperature Gradients at the hot and cold walls

much more pronounced. Also as mentioned, and it is apparent from the interferogram in Figure 7.4b, rotational flows are predominant in the central region (convective region). In this region, the slope is negative at low Rayleigh numbers and increases to zero at about $Ra = 12000$. This is seen in Figure 7.8. The slope becomes positive for about a $Ra \geq 12000$. This phenomenon in the central region of the enclosure is known as the temperature reversal. As the Rayleigh number and the strength of the rotation increased, the temperature reversal became more pronounced.

From the interferograms of Figures 7.3d and 7.4f, it is apparent that the cell-height to width ratio was decreased as the Rayleigh number increased. This agrees with Farhadieh [37], Willis [41] and disagrees with the calculation of Schneck [17] who assumed the cell-height to width ratio to be 1.0.

The results of this investigation indicate a reversal in the temperature profile occurring at about $Ra/Ra_{crit.} \geq 7.0$, in the central region of the enclosure, where the natural convection is important. However, these results are in disagreement with the previous studies of Veronis [19], Farhadieh [37] and Gille [36] who discovered reversal in the temperature profile at

$Ra/Ra_{crit.} \geq 4, 3.8$ and 16 respectively.

7.3 HEAT TRANSFER BY NATURAL CONVECTION IN THE ENTIRE ENCLOSURE

To establish the heat transfer by natural convection in the entire enclosure, it is important to determine the critical Rayleigh number for the onset of natural convection. The straight line equation developed by Hollands et al. [105] and used by Elsharbiny [106], is of the form

$$\overline{Nu} = 1 + C \left[1 - \frac{Ra_{crit.}}{Ra} \right]$$

This equation was then applied to the data of the previous section. The results were plotted with $(\overline{Nu} - 1)$ vs $1/Ra$. Figure 7.10 illustrates these results when $(\overline{Nu} - 1)$ was plotted against $(10000/Ra)$. The critical Rayleigh number was determined by the intersection of a least square method (a straight line) through the data points and the horizontal axis. The critical Rayleigh number was then obtained and found to be $Ra_{crit.} = 1717$. This value agrees well with the expected theoretical value [106] of $Ra_{crit.} = 1708$ within 0.5%.

7.3.1 Conduction Regime

Typical interferograms of the conduction regime, for the entire cavity, are shown in Figure 7.11.

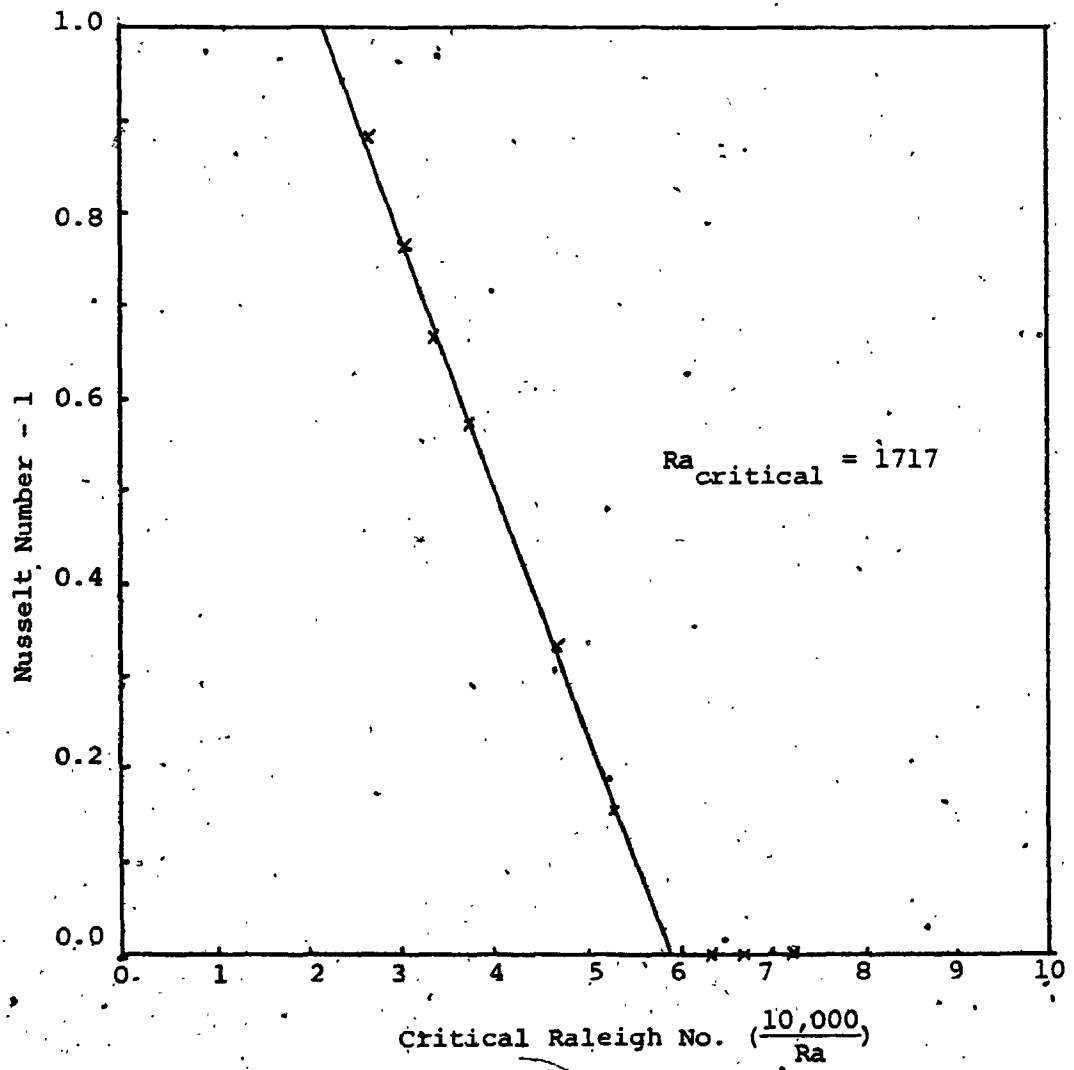


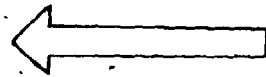
FIGURE 7.10 Determination of the Critical Rayleigh Number

In these finite fringe interferograms, the two distinct heat transfer regions, separated by the top and bottom plate boundaries, are clearly defined and shown in Figure 7.11a. The flow direction on the surface of the cold plate, the top boundary, is illustrated where the flow passes over the sections (a,b,c and d) respectively.

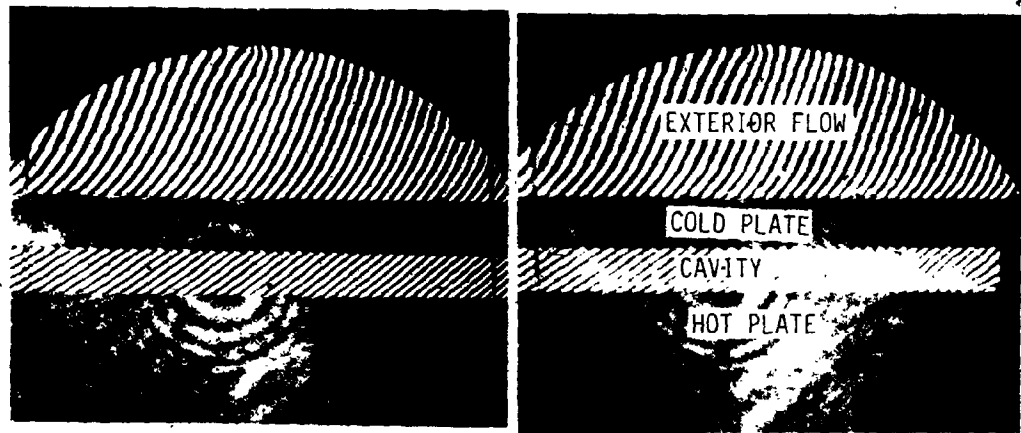
In the enclosure, the fringes are straight and equally spaced. As discussed in section 7.3, this indicates that the heat transfer in this region is predominantly conduction. A closer examination of the interferograms (7.11a and d) indicate shifted fringes at the two ends. For these end effects, a slight degree of natural convection is taking place. This might be due to the boundary layer effects on the vertical walls and by the fact that these boundaries are hotter at the bottom and colder at the top.

The forced convection on the surface of the top plate is illustrated by a slight fringe shift close to the boundary. However, away from this boundary, fringes are straight and equally spaced which indicates a uniform free stream temperature.

Vertical and horizontal temperature profiles in the entire enclosure of the interferograms of Figure 7.11 are given in Figures 7.12 and 7.13. In Figure

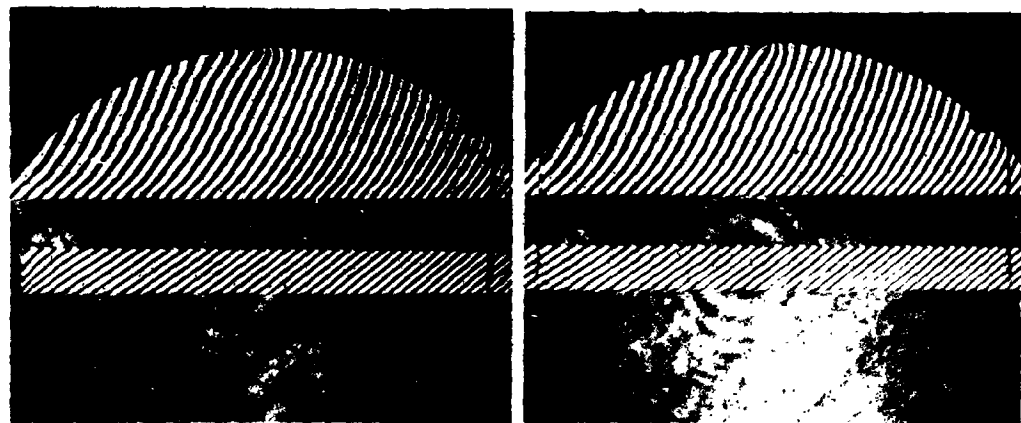


FLOW DIRECTION



b

a



d

c

FIGURE 7.11 Finite Interferograms Illustrating the Conduction Regime; AR=35.4, Re=17600, Ra=1100, THC=30.2, TCB=24.0

SEC.	THC	TCB	AR	REY	RAL
1	30.10	23.92	35.40	17652	1117
2	30.22	24.04	35.40	17652	1114
3	30.28	24.18	35.40	17663	1098
4	30.00	24.20	35.40	17674	1046

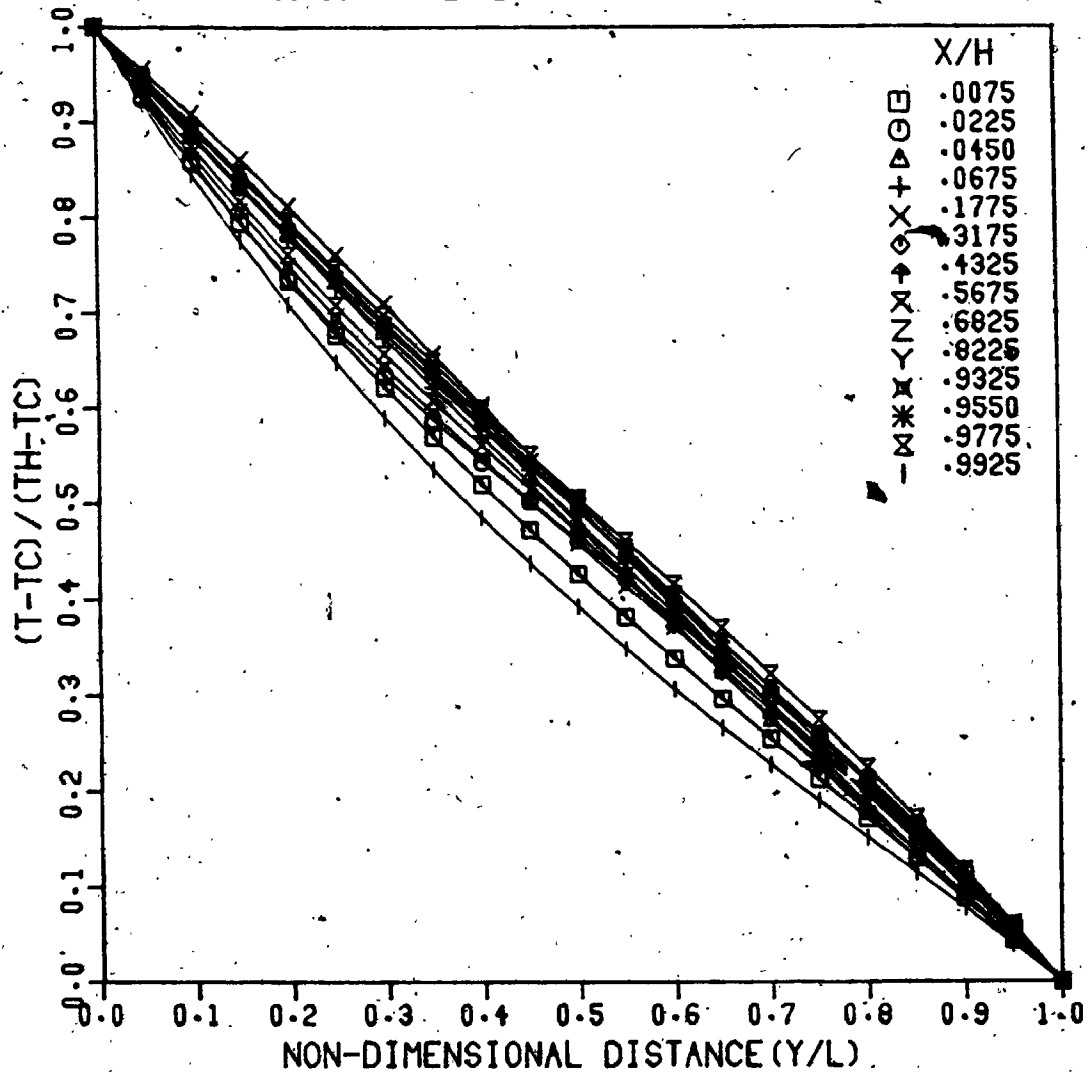


FIGURE 7.12 Experimental Vertical Temperature Profile

7.12, the results of fourteen temperature profiles scanned at various horizontal positions are presented. These include for Figure 7.11 five scans for interferogram (a) for $X/H = 0.0075$ to 0.1775 , two scans for the interferogram (b) for $X/H = 0.3175$ and 0.4325 , two scans for interferogram (c) for $X/H = 0.5675$ and 0.6825 , and five scans for interferogram (d) for $X/H = 0.8225$ to 0.9925 . The end effects are shown by the nonlinear temperature profiles close to the two vertical boundaries. Also, for each interferogram, the average temperatures of the hot plate and cold plate boundaries, the aspect ratio, the Reynolds number and the Rayleigh number are shown respectively. Procedures for the temperature calculation from the shifted fringes are given in Appendix B.

Figure 7.13 describes the horizontal temperature profiles for the same interferograms. Because of the conduction regime, these profiles are equally spaced and close to linear except near the vertical walls. The edge effects of the vertical boundaries are clearly defined. The vertical position, $Y/L = 0.05$ to 0.95 , for each horizontal temperature plot is given on the right-hand side.

The local Nusselt numbers were calculated from the

SEC.	THC	TCB	AR	REY	RAL
1	30.10	23.92	35.40	17652	1117
2	30.22	24.04	35.40	17652	1114
3	30.28	24.18	35.40	17663	1098
4	30.00	24.20	35.40	17674	1046

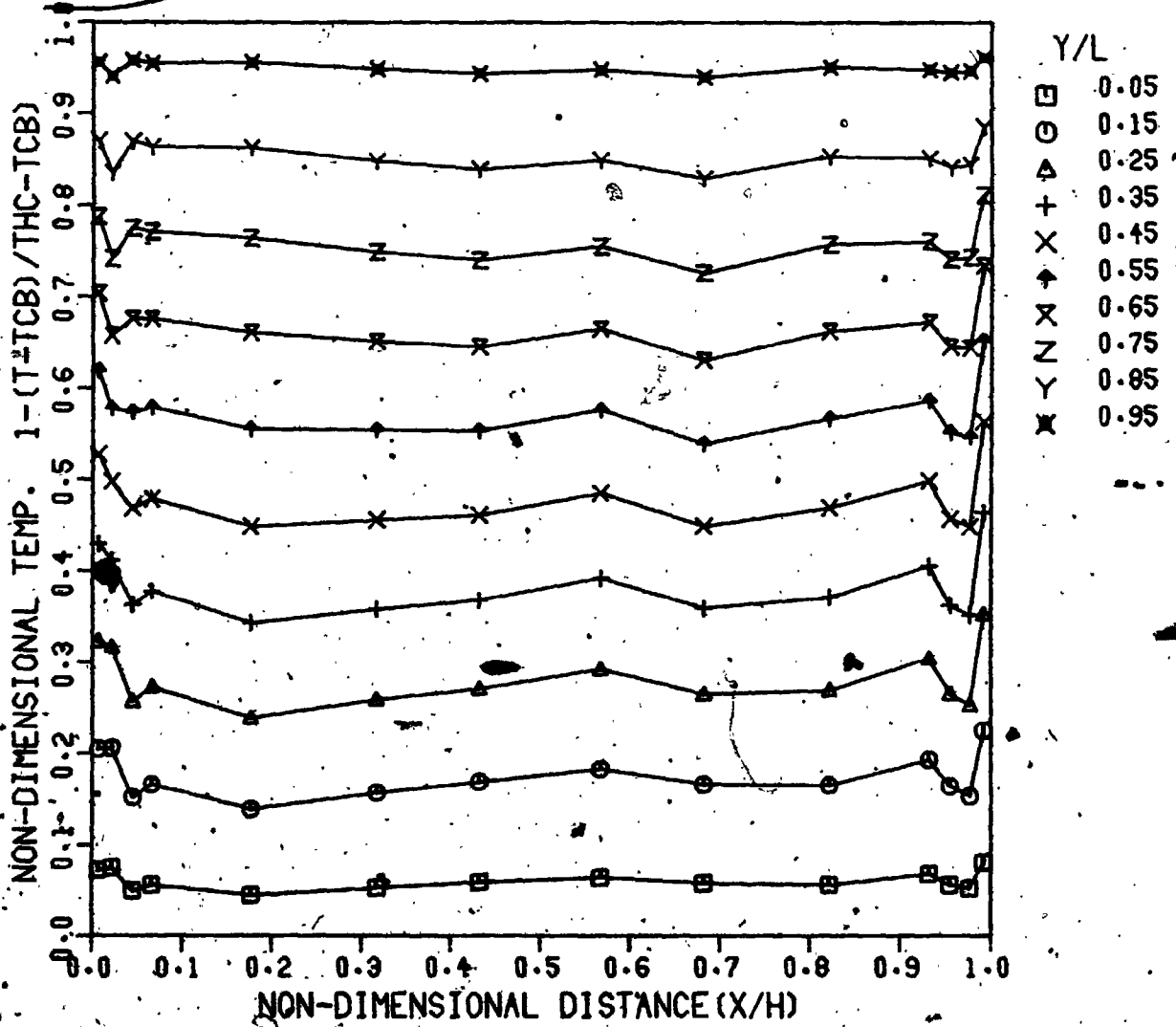


FIGURE 7.13 Experimental Horizontal Temperature Profile in the Cavity.

vertical temperature profiles, as given in Appendix C. Figure 7.14 is a plot of the local Nusselt numbers calculated from the vertical temperature profiles of Figure 7.12. The Nusselt numbers were determined from the slopes of the temperature profiles near the hot and cold plate boundaries respectively. The average Nusselt numbers were calculated from the local Nusselt numbers, as given in Appendix C. For the conduction regime, the average Nusselt number was found to be unity.

7.3.2 Convection Regime

For the Rayleigh number greater than the critical Rayleigh number, $Ra_{crit.} = 1717$, the motion due to natural convection in the form of cellular rotational or Benard cells, occurred in the enclosure. This regime, which occurs in the entire enclosure, is illustrated in Figure 7.15. In these interferograms, the two distinct heat transfer regions, separated by the top and bottom plate boundaries, are clearly defined and shown in Figure 7.15a. The finite interferograms, for the same physical and boundary conditions similar to Figure 7.15, are shown in Figure 7.16. As expected, because of the natural convection in the cavity and on the surface of the top plate, the shifted fringes are no longer linear. However, the slightly shifted fringes

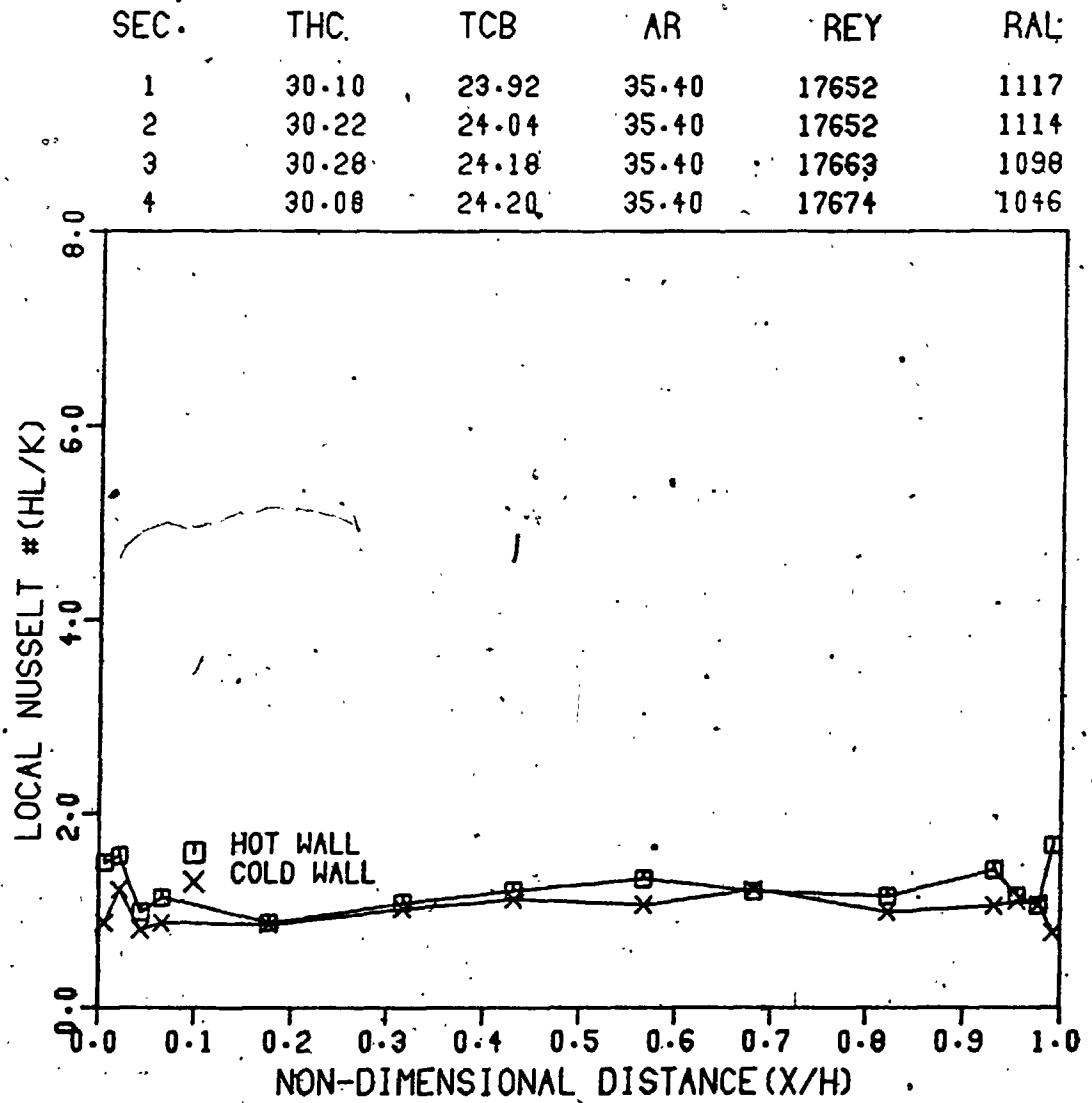
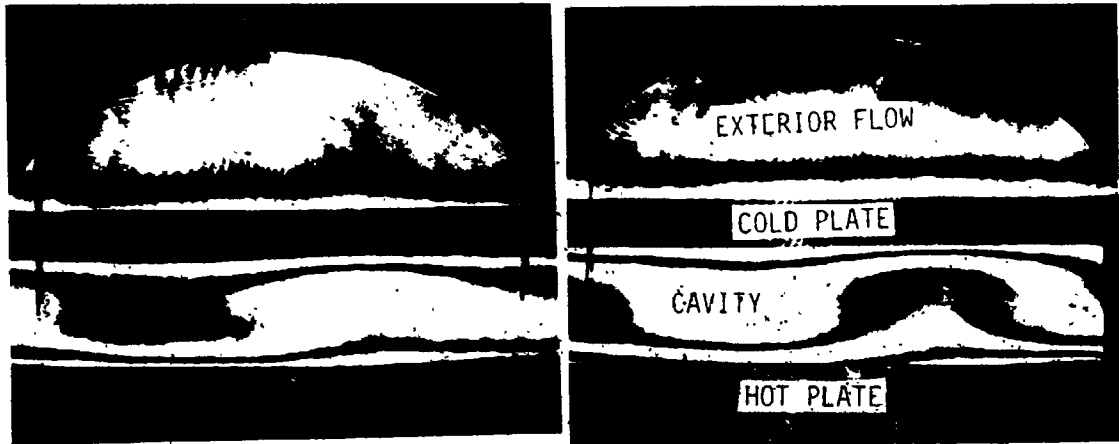
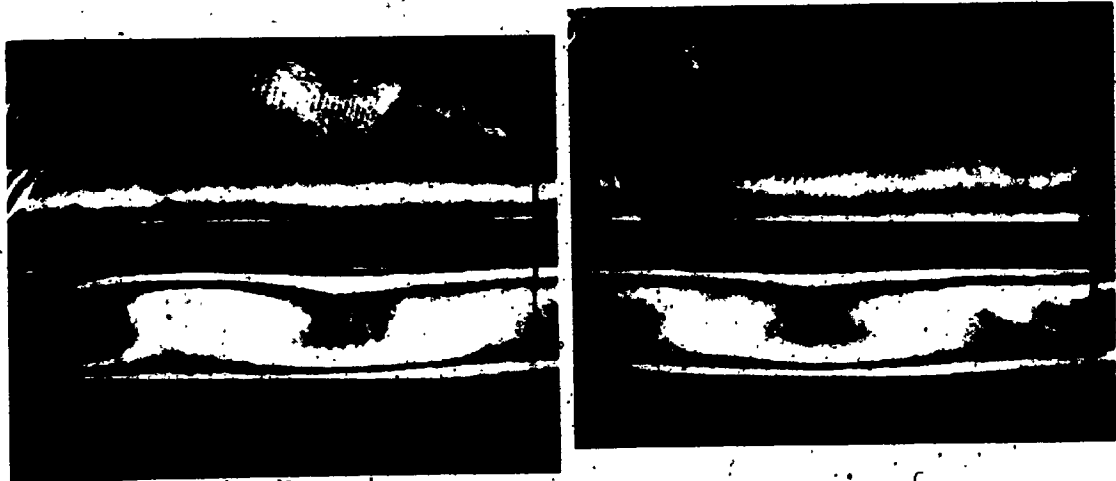


FIGURE 7.14 Local Characteristic of Nusselt Number



b

a



d

c

FIGURE 7.15 Infinite Fringe Interferograms for Free Convection; $AR=17.7$, $Re=0.0$, $Ra_{ave}=8357$, $THC_{ave}=30.24$, $TCB_{ave}=24.41$

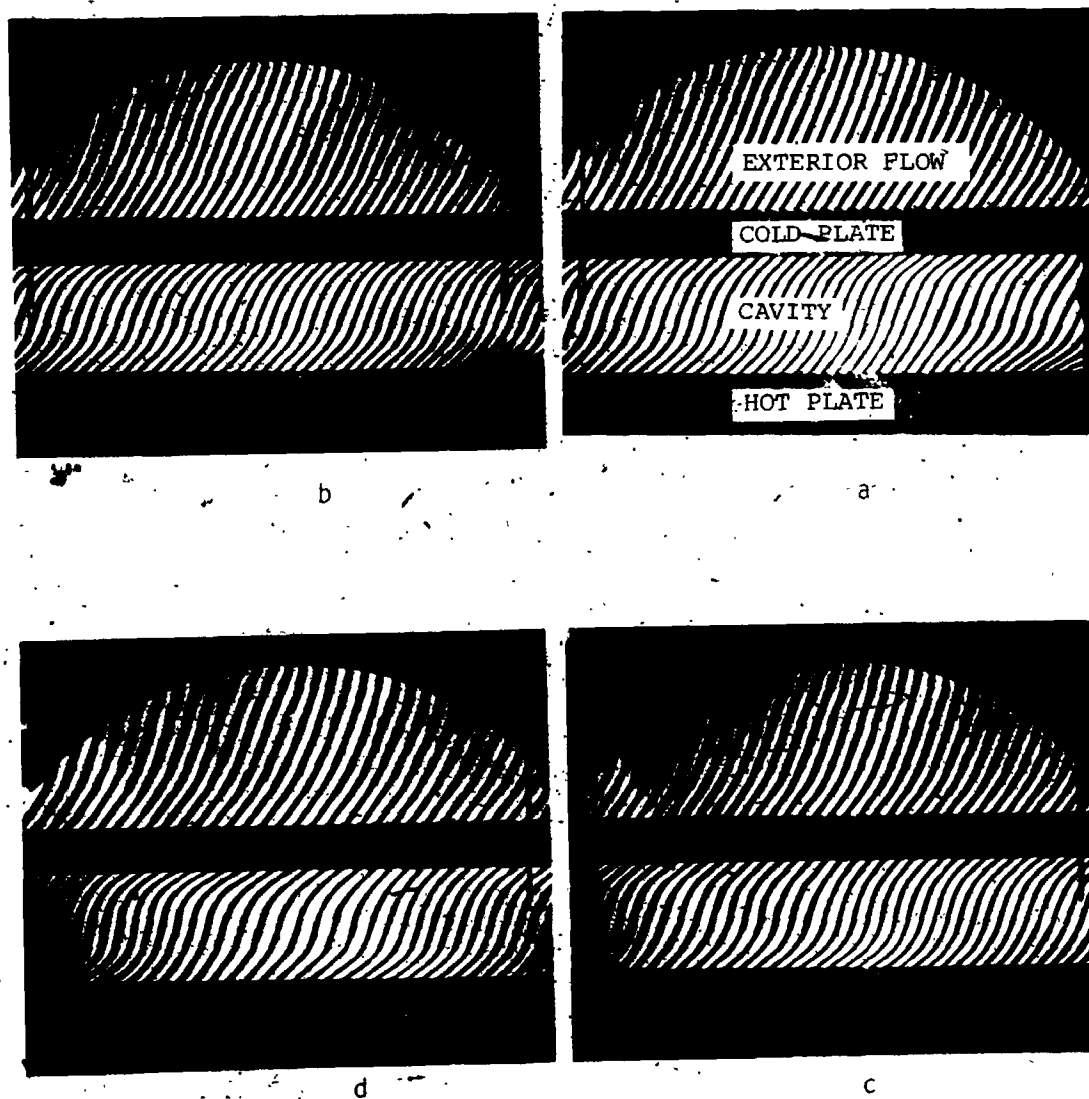
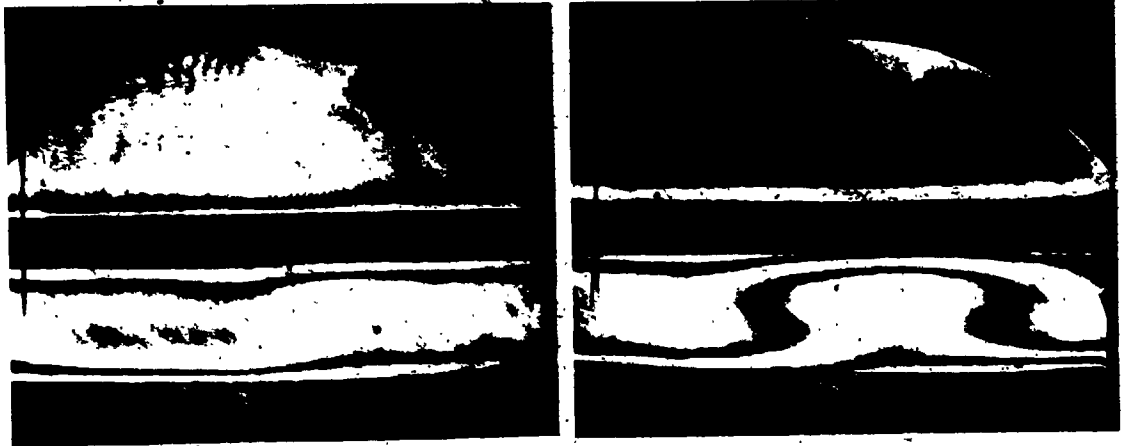
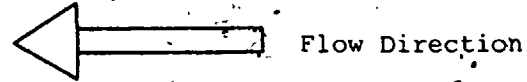


FIGURE 7.16 Finite Fringe Interferograms for Free Convection; $AR=17.7$, $Re=0.0$, $Ra_{ave}=8357$, $THC_{ave}=30.24$, $TCB_{ave}=24.41$

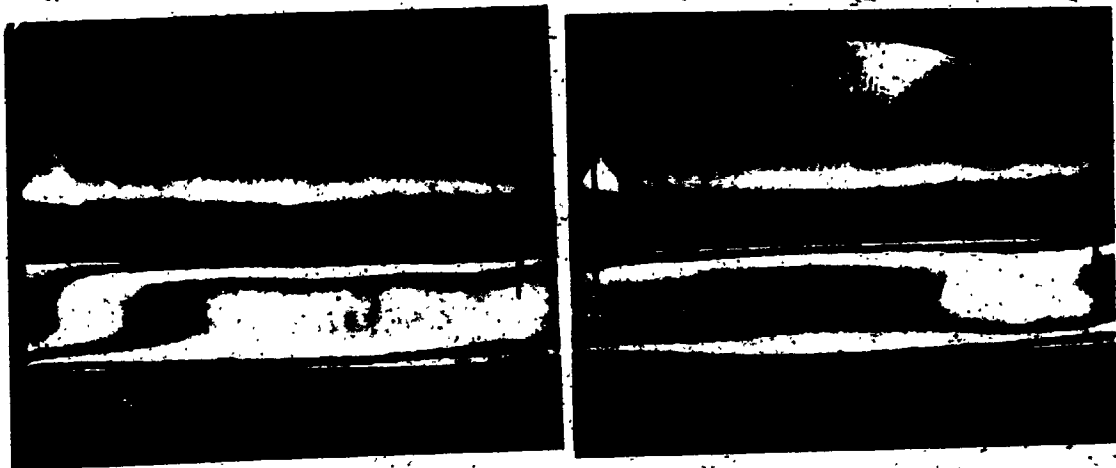
near the top surface become linear further away from the top surface. This is due to the fact that near the top surface there exists some natural convection and that the free stream temperature is uniform. This can also be seen in Figure 7.15.

The forced convection on the top surface boundary for the same isothermal bottom boundary condition is illustrated in Figures 7.17 and 7.18. The infinite fringe interferograms shown in Figure 7.17 have the same physical boundary conditions as the finite fringe interferograms in Figure 7.18. To illustrate the coupling effect of the exterior forced convection on the natural convection in the enclosure, the bottom plate temperature was kept constant for all of the interferograms shown in Figures 7.15 to 7.18. As the Rayleigh number increased, the convection heat transfer also increased and this is shown on Figures 7.19 and 7.20. Figure 7.19 illustrates the vertical temperature profiles in the enclosure for the interferograms of Figure 7.16 with no forced convection on the top surface. Figure 7.20 shows a plot of vertical temperature profiles within the cavity for the interferograms of Figure 7.18 where there is exterior forced convection.



b

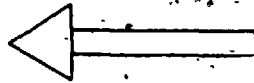
a



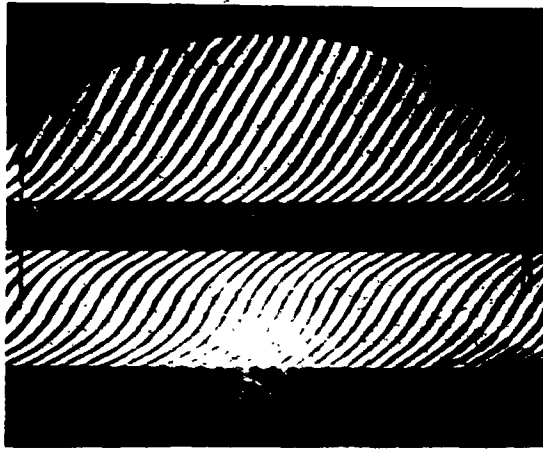
d

c

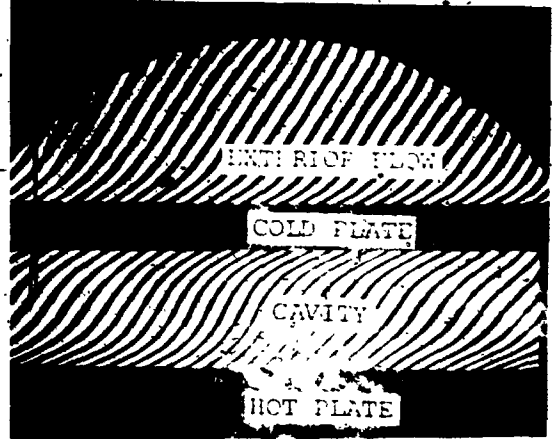
FIGURE 7.17 • Infinite Fringe Interferograms for Forced Convection; $AR=17.7$, $Re_{ave}=16973$, $Ra_{ave}=91037$, $ThC_{ave}=30.15$, $TcB_{ave}=23.83$



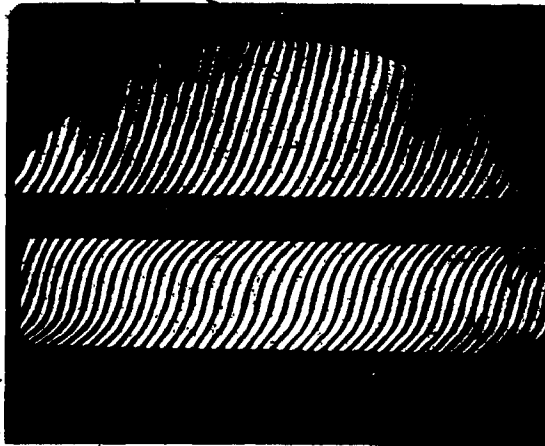
Flow Direction



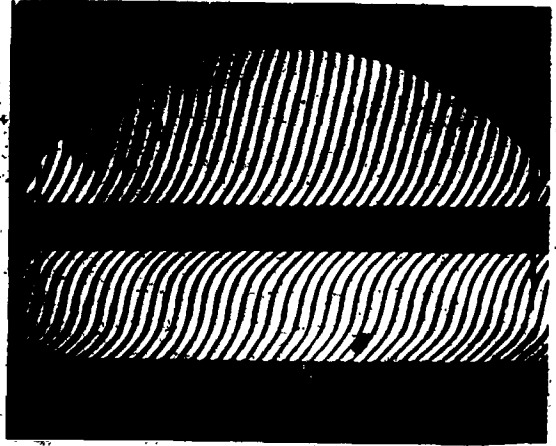
b



a



d



c

FIGURE 7.18 Finite Fringe Interferograms for Forced Convection; $AR=17.7$, $Re_{ave}=16973$, $Ra_{ave}=9103$, $THC_{ave}=30.15$, $TCB_{ave}=23.83$

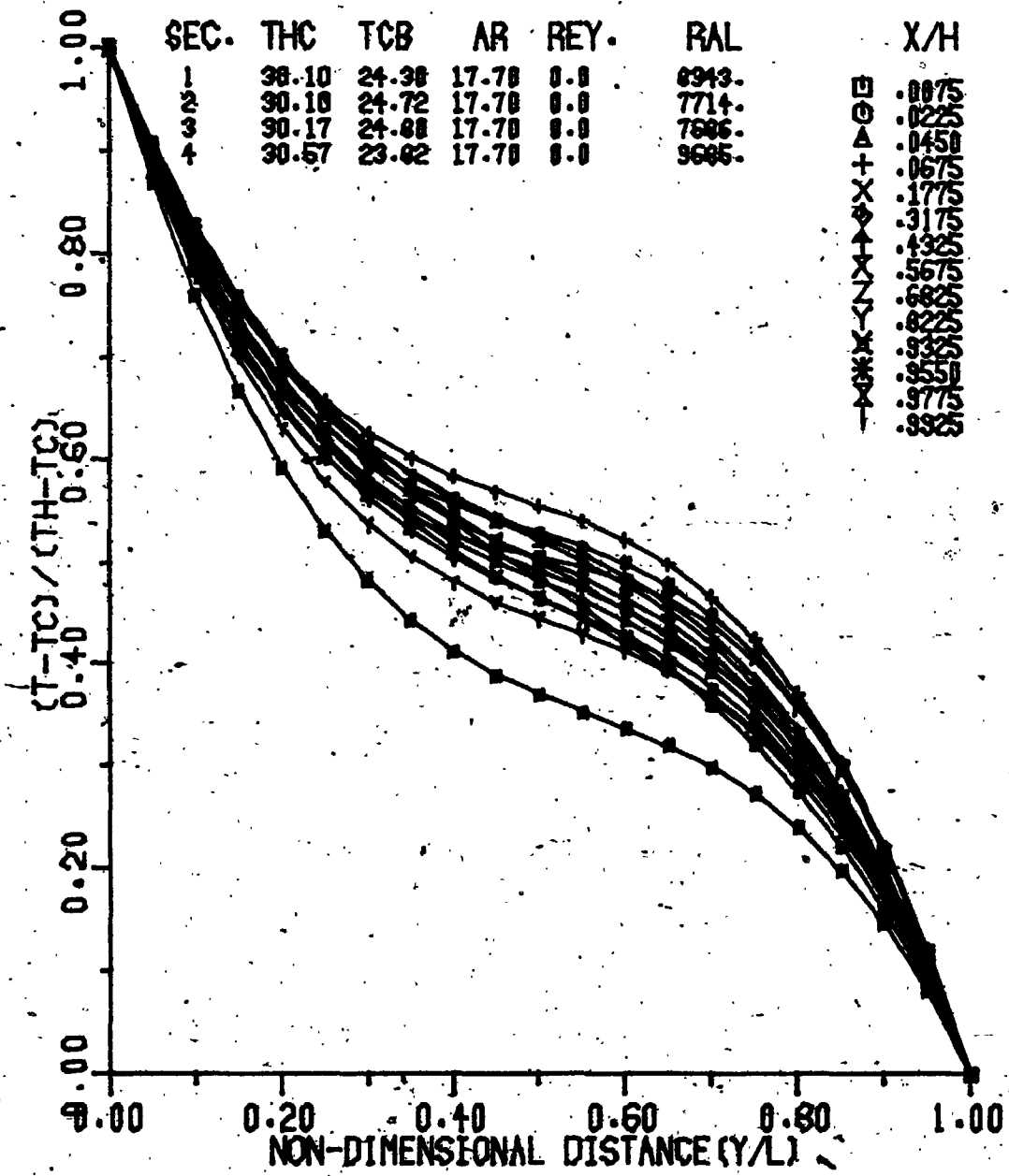


FIGURE 7.19 Experimental Vertical Temperature Profile in the Cavity

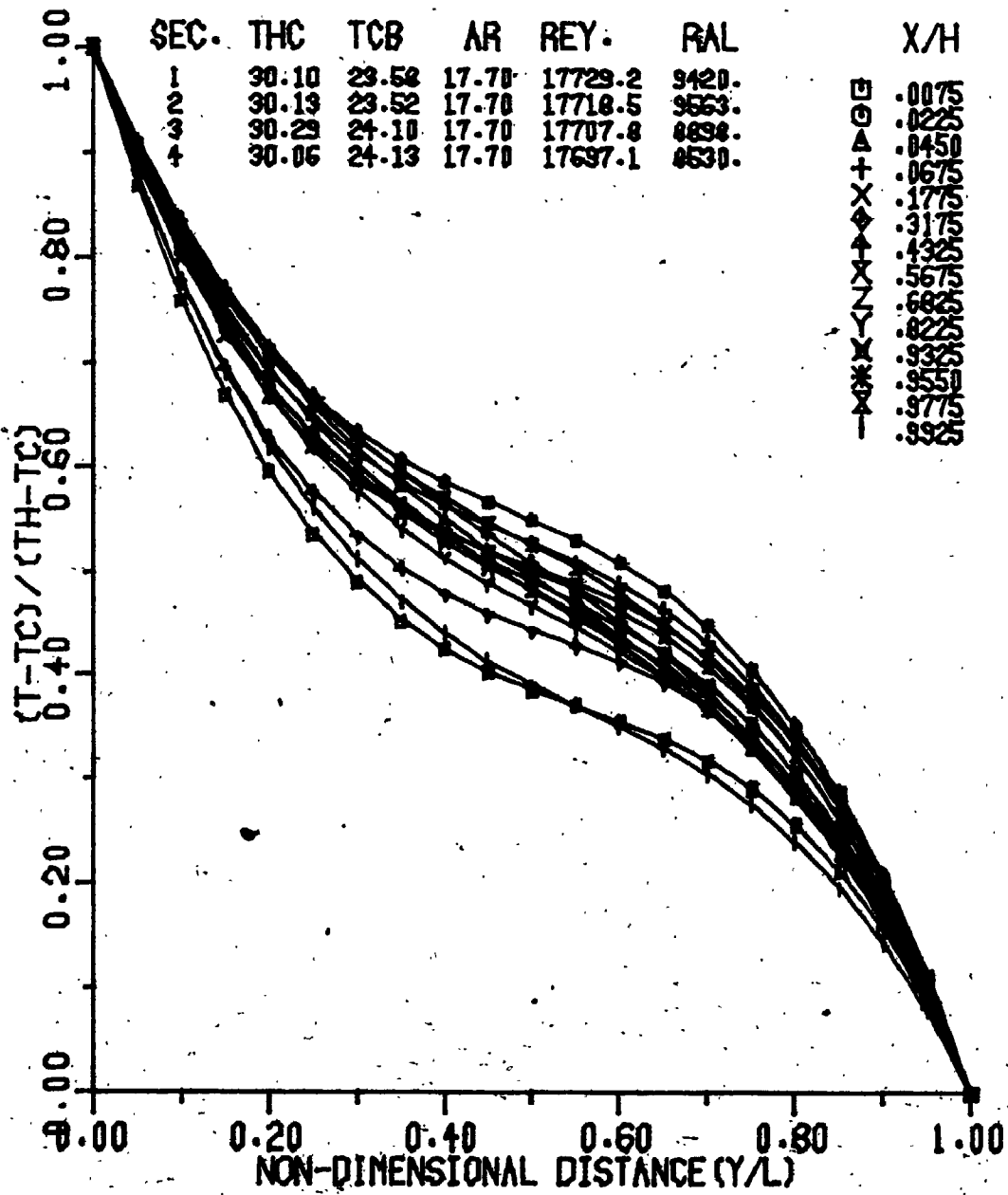


FIGURE 7.20 Experimental Vertical Temperature Profile in the Cavity

The temperature distribution within the cavity was also plotted horizontally for the convection regime. Figure 7.21 is a typical plot of horizontal temperature for equal vertical spatial increments while Figure 7.22 is a plot of the same interferograms with equal horizontal temperature increments. In these figures, because of the natural convection regime within the cavity, the temperature profiles are no longer equally spaced. In Figure 7.21, the temperature profiles are concentrated in the central region which indicate smaller temperature gradients; thus, there is less heat transfer. However, closer to the horizontal boundaries, the temperature profiles are farther apart which indicate greater temperature gradients; thus, there is more heat transfer. The same argument holds for Figure 7.22.

The gradients of the vertical temperature profiles near the two horizontal boundaries were established and then were used to calculate the local Nusselt numbers. The average Nusselt number was calculated from the local Nusselt numbers. A typical plot of the local Nusselt numbers is given in Figure 7.23.

Figure 7.24 shows the infinite fringe pattern for natural convection in the cavity where two dimensional Benard cells no longer exist. The finite fringe interferograms

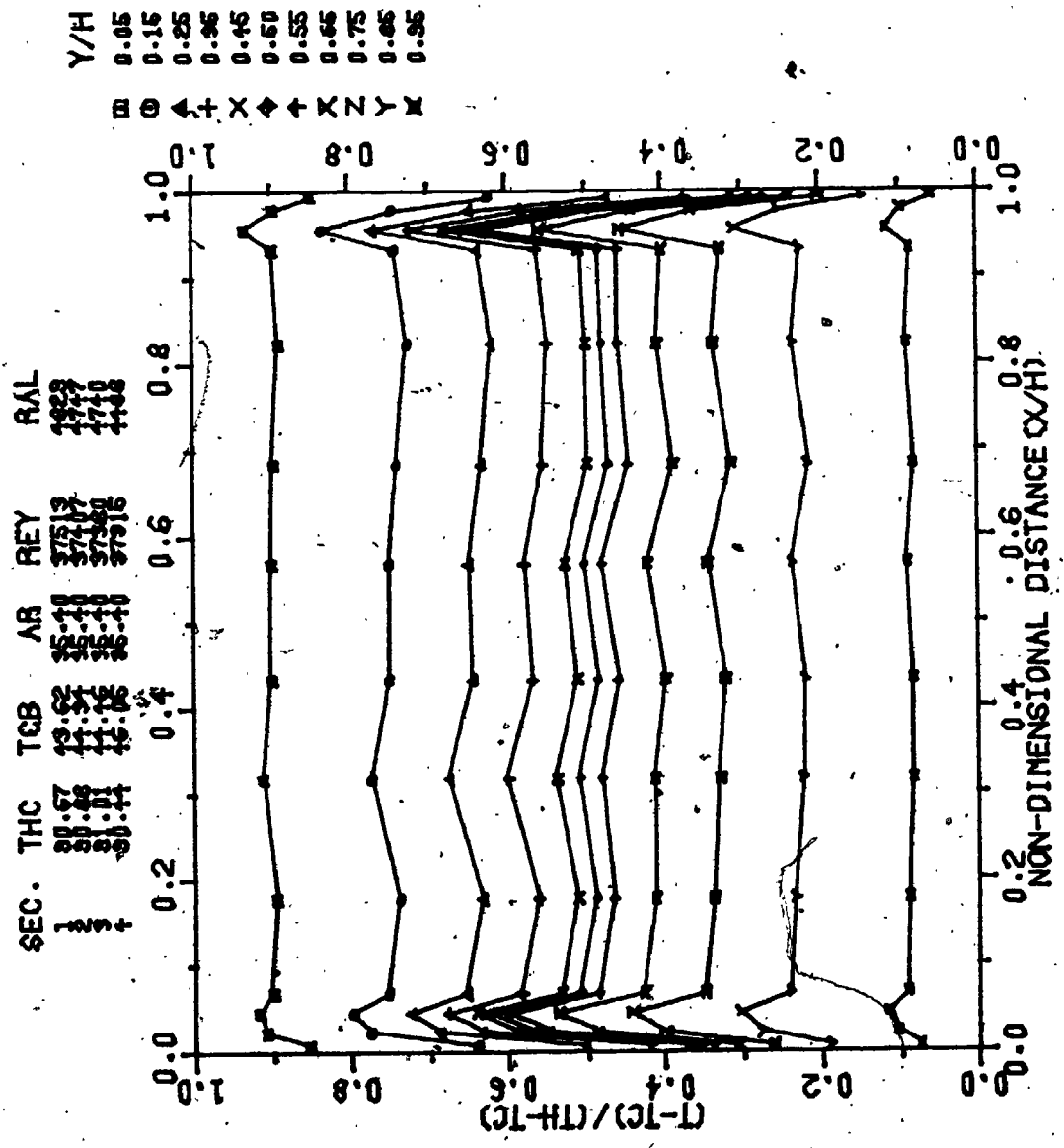


FIGURE 7.21 Experimental Horizontal Temperature Profile.

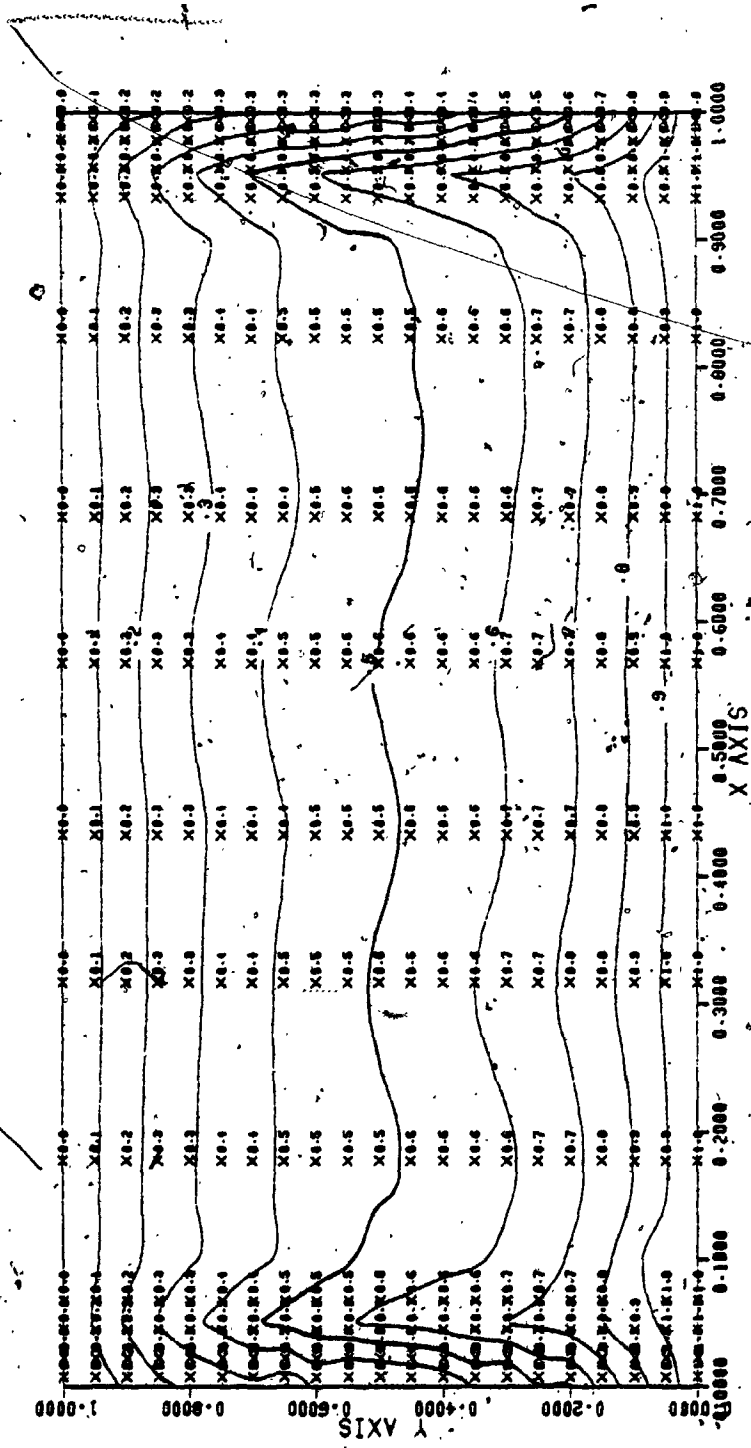


FIGURE 7.22 Plot of Isotherms in the Cavity;

AR=35.4, Re_{ave} =37404, Ra_{ave} =4701,

Thc_{ave} =90.75, Tcb_{ave} =44.62

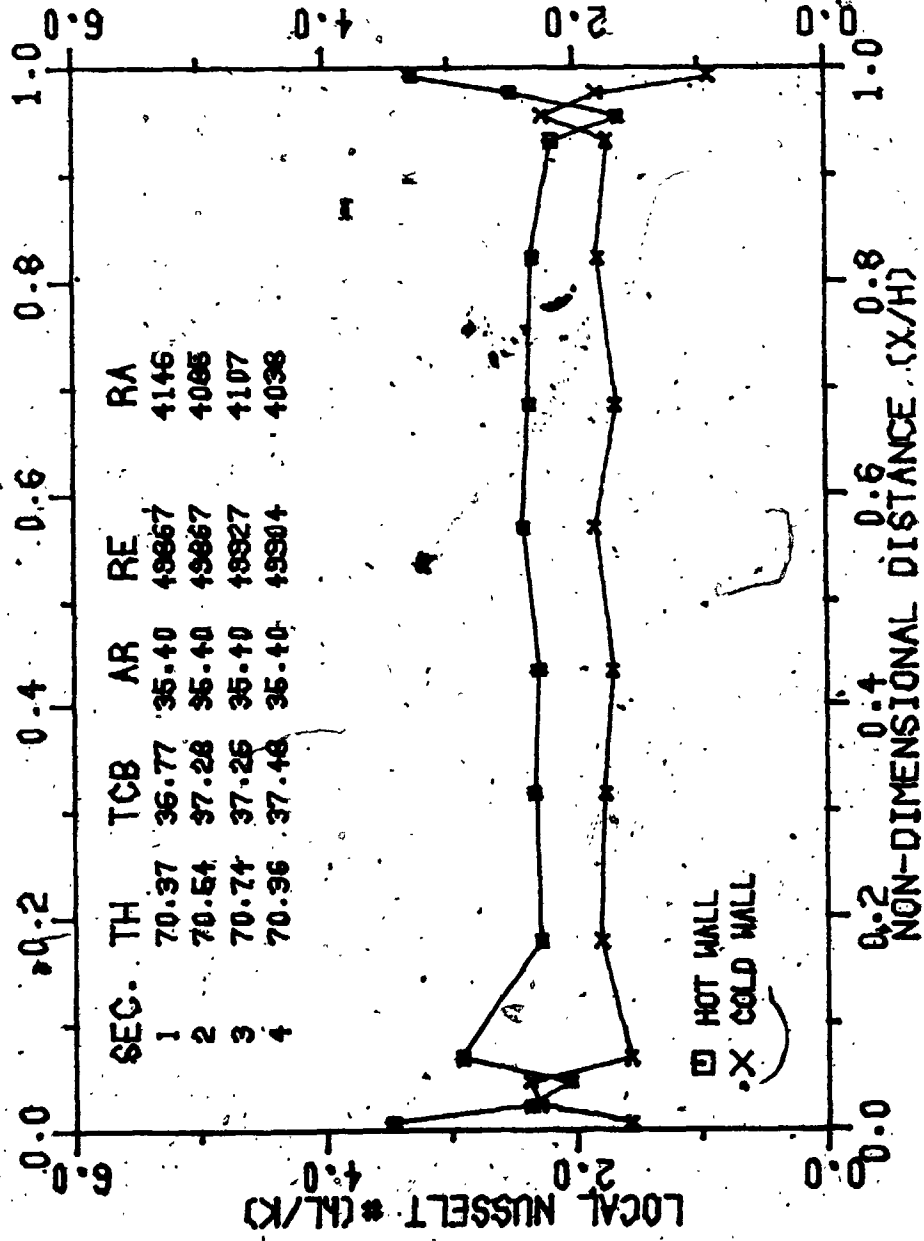
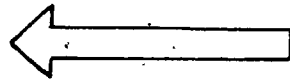
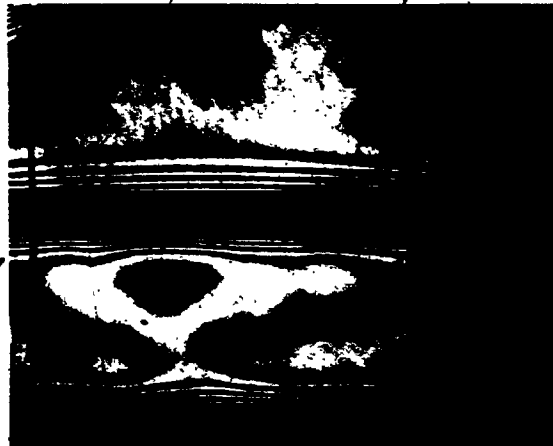


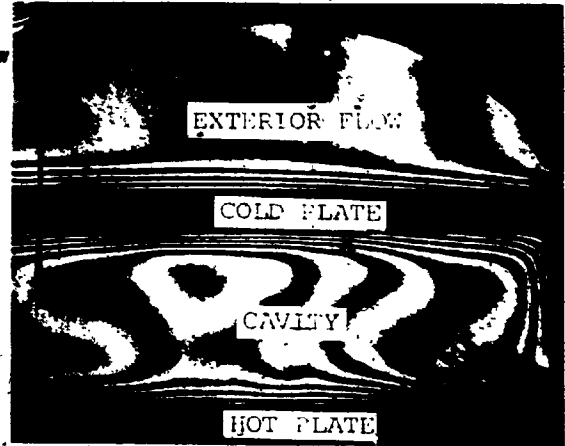
FIGURE 7.23 Cavity Nusselt Number as a Function of Distance



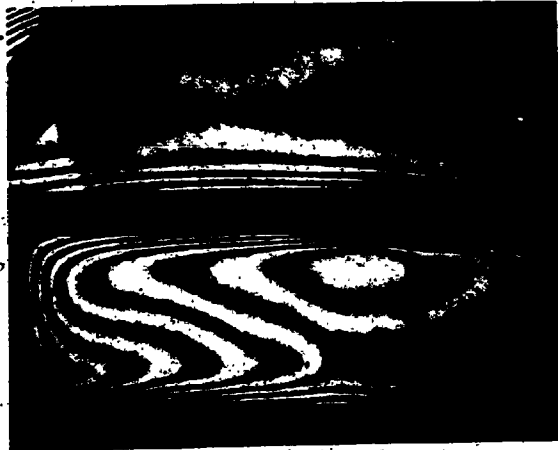
FLOW DIRECTION



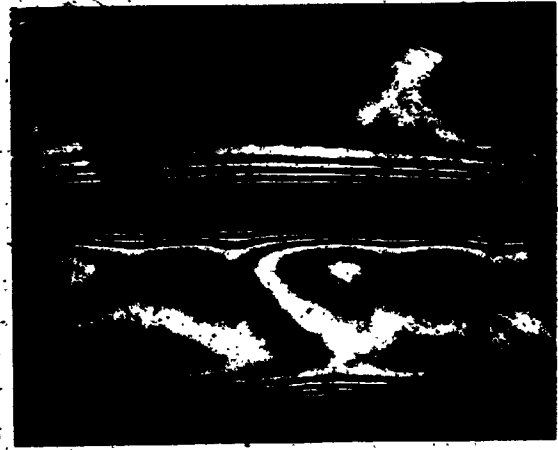
b



a



d



c

FIGURE 7.24 Infinite Fringe Interferograms for Forced Convection; $AR=11.8$, $Re_{ave}=17701$, $Ra_{ave}=75560$, $THC_{ave}=50.33$, $TCB_{ave}=31.47$.

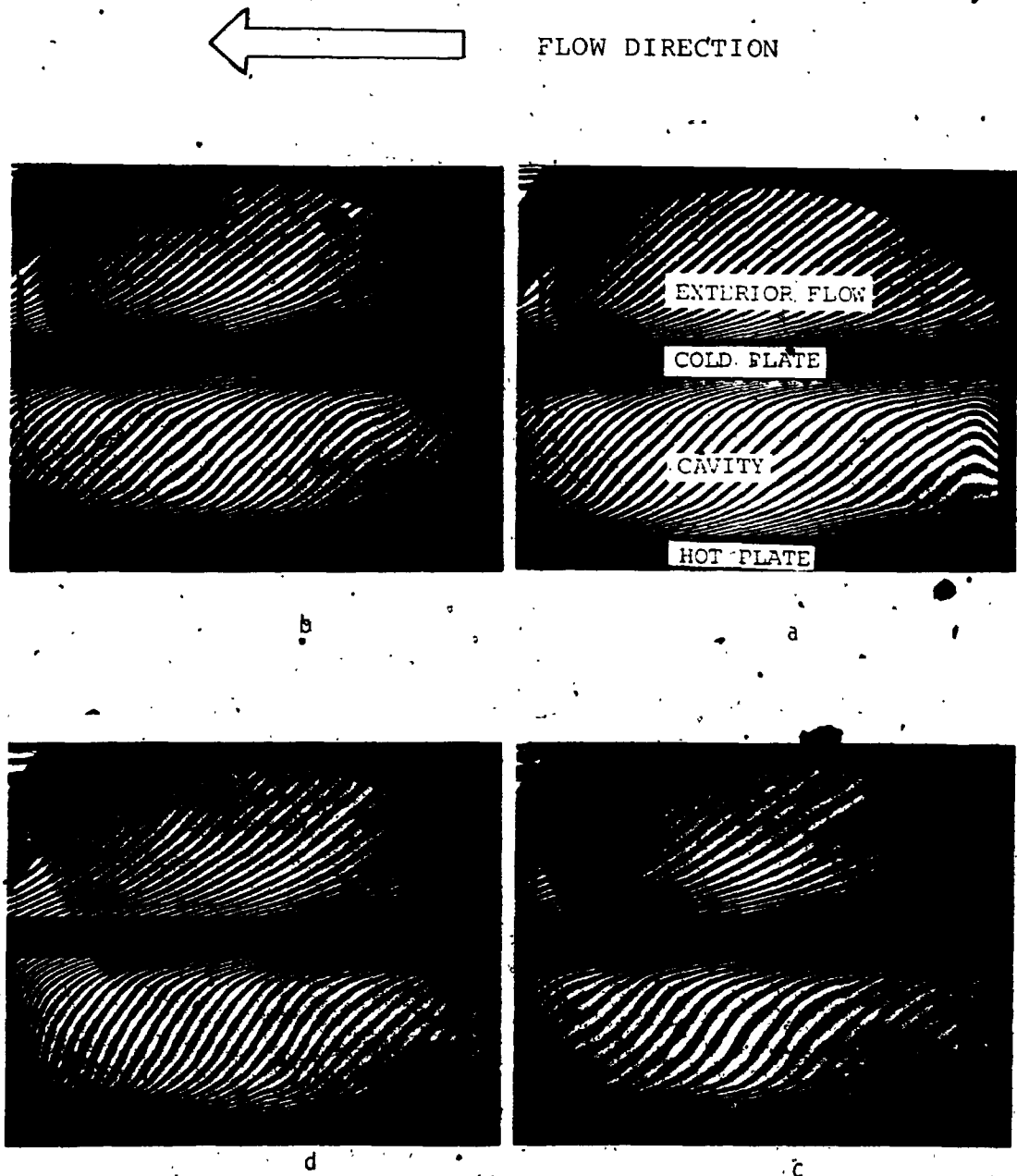


FIGURE 7.25 Finite Fringe Interferograms for Forced Convection; $Ar=11.8$, $Re_{ave}=17701$, $Ra_{ave}=75560$, $ThC_{ave}=50.33$, $TcB_{ave}=31.47$

for the same figure are shown in Figure 7.25. The temperature reversal of the vertical and horizontal profiles for the same interferograms are given in Figures 7.26 and 7.27 respectively. The plot of local Nusselt numbers is presented in Figure 7.28.

7.3.3 Cavity Data Correlation

As it was shown in Chapter II, from the non-dimensional governing mathematical equations, the heat transfer in an enclosure depends on parameters such as Grashof number, Prandtl number and possibly aspect ratio.

For the conduction regime within the enclosure, when Rayleigh number is less than the critical Rayleigh number, $Ra_{crit.} = 1717$, the average Nusselt number was found to be unity, $\overline{Nu} = 1$. However, for the convection rotational regime, when Rayleigh number is greater than the critical Rayleigh number, $Ra > 1717$, the experimental data revealed a strong dependency of the average Nusselt number on the Rayleigh number. A statistical computer analysis program, called FASTFIT, from System Analysis, Control and Design Activity (SACDA), The University of Western Ontario, was used for finding the data correlation equation. The regression of the data by the program provided the following equation:

$$\overline{Nu} = 0.714 Ra_L^{0.149}$$

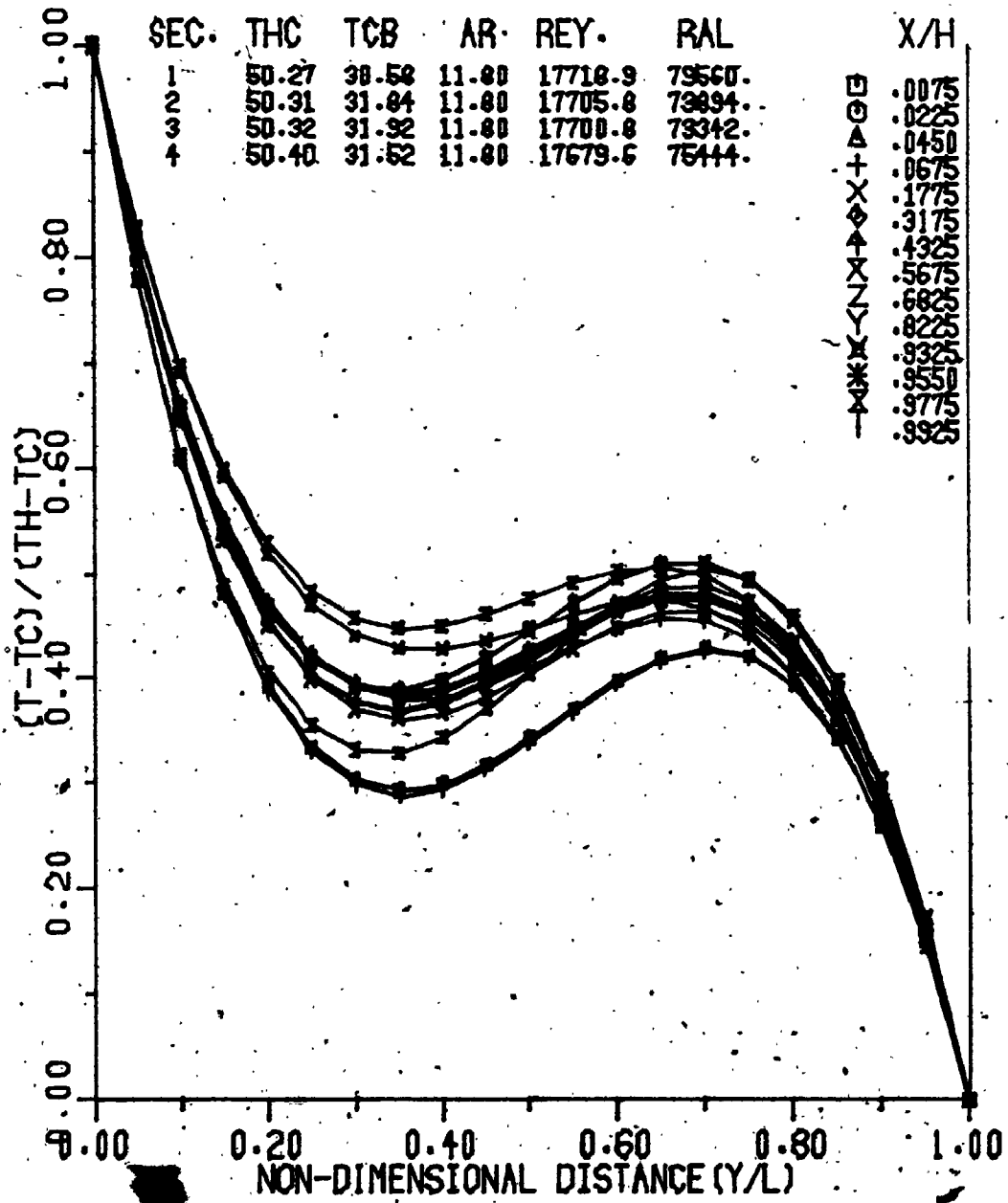
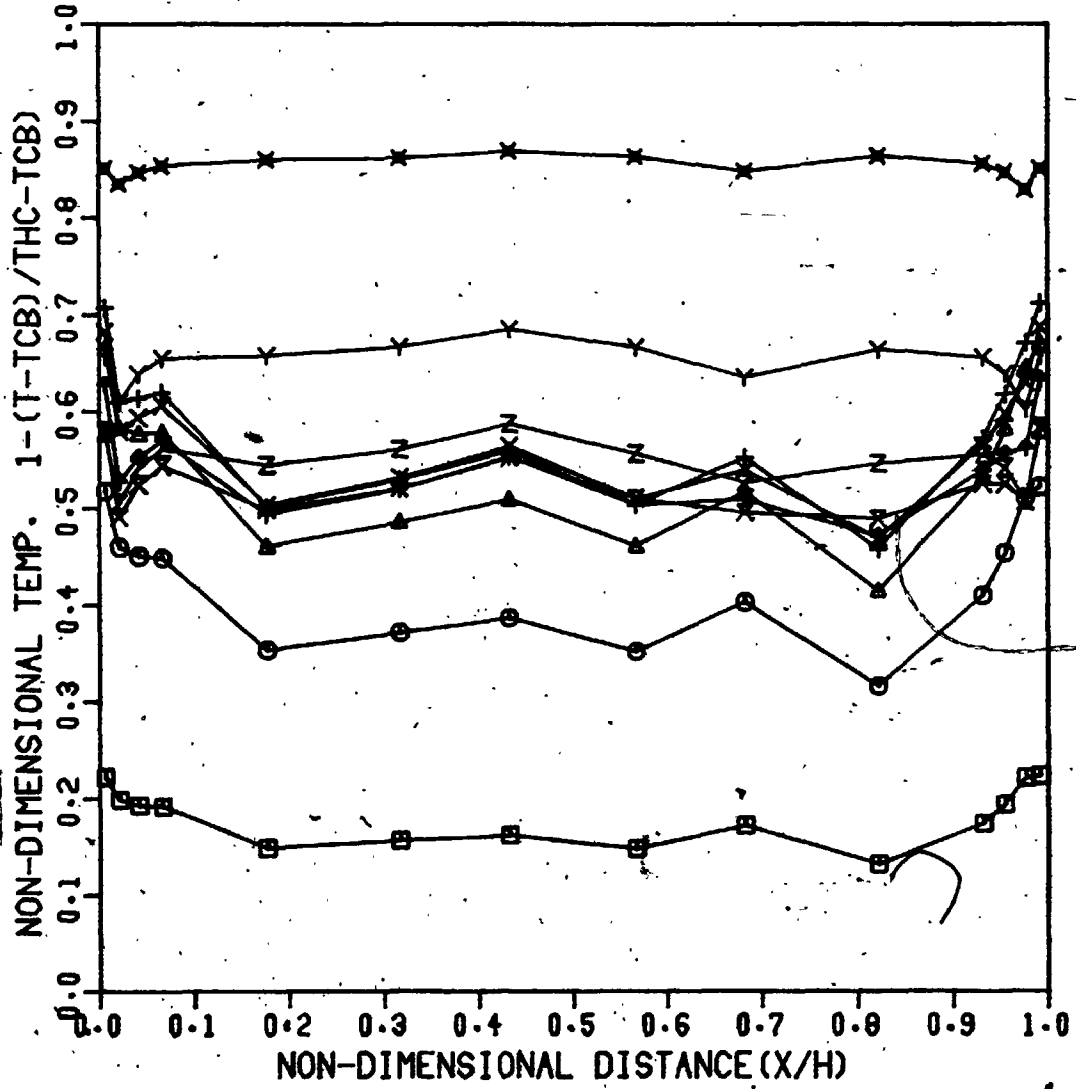


FIGURE 7.26 Experimental Vertical Temperature Profile in the Cavity

SEC.	THC	TCB	AR	REY.	RAL.
1	50.27	30.58	11.80	17719	79560
2	50.31	31.84	11.80	17706	73894
3	50.32	31.92	11.80	17701	73342
4	50.40	31.52	11.80	17680	75444



Y/L	
0.05	□
0.15	○
0.25	△
0.35	+
0.45	x
0.55	↑
0.65	X
0.75	Z
0.85	Y
0.95	x

FIGURE 7.27 Experimental Horizontal Temperature Profile in the Cavity

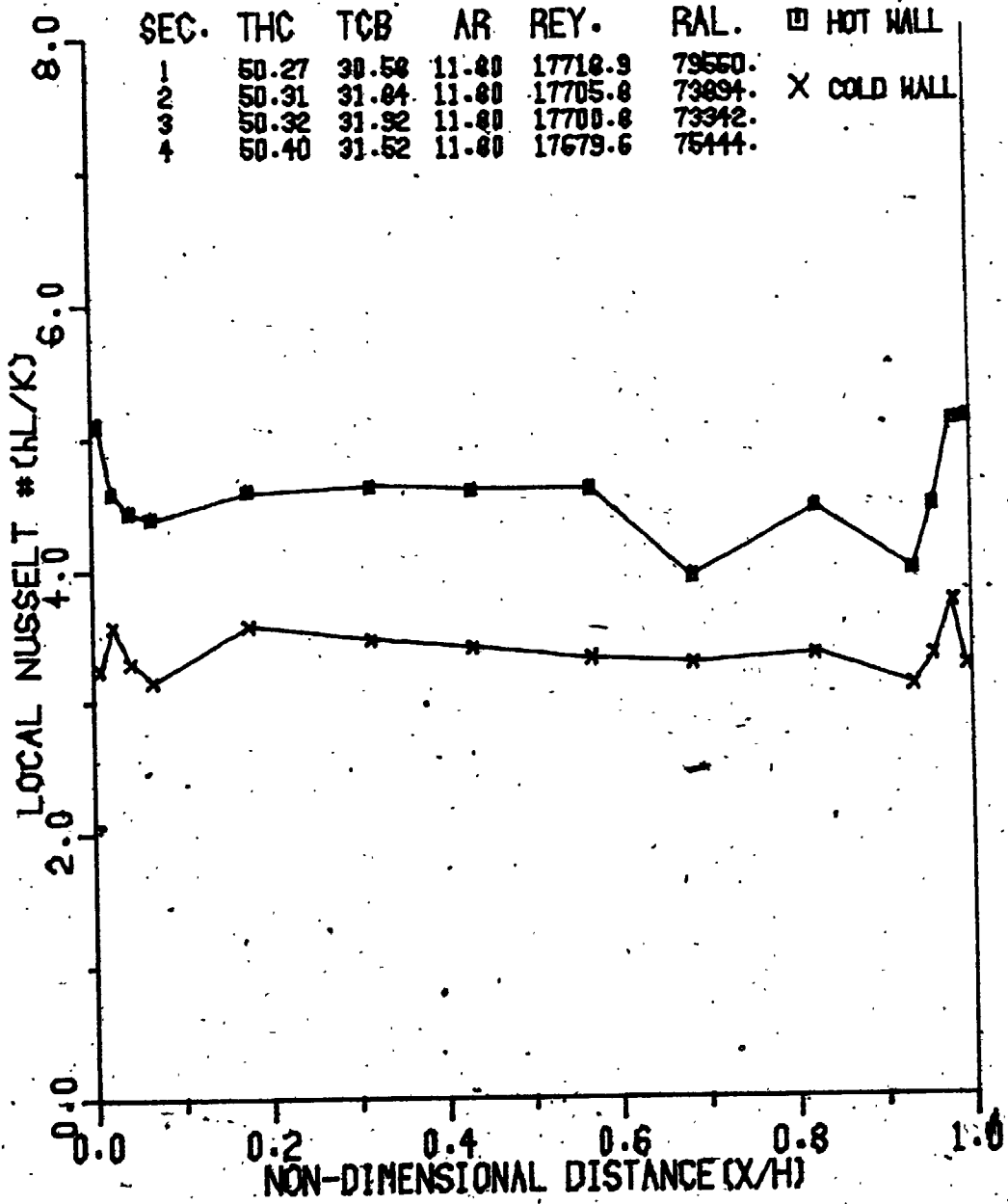


FIGURE 7.28 Local Characteristic of Nusselt Number in the Cavity

with an average percent error of 5.1.

A plot of this equation is compared with the results of other investigations in Figure 7.29.

7.4 FORCED CONVECTION ON THE SURFACE OF GLAZING PLATE

The temperature of the glazing surface depended on parameters such as the temperature of the bottom plate boundary, the height of the cavity and forced convection in the wind tunnel. The surface temperature never seemed to be isothermal. In the case of natural convection, the temperature peaked at the centre of the plate and tapered off toward the edges. However, for the case of forced convection, the plate was cooled more at the leading edge of the thermal boundary layer on the surface. As the boundary layer got thicker, due to the fact that there was more resistance to the heat transfer, the temperature drop was not as pronounced at the leading edge.

Figure 7.15 illustrates the natural convection on the surface of the glazing. The exterior forced convection is shown in Figures 7.17 and 7.24. The forced convection had a coupling effect with the natural convection inside the enclosure by increasing the Rayleigh number, within the cavity. The average Nusselt number below the glazing surface was used for calculating the

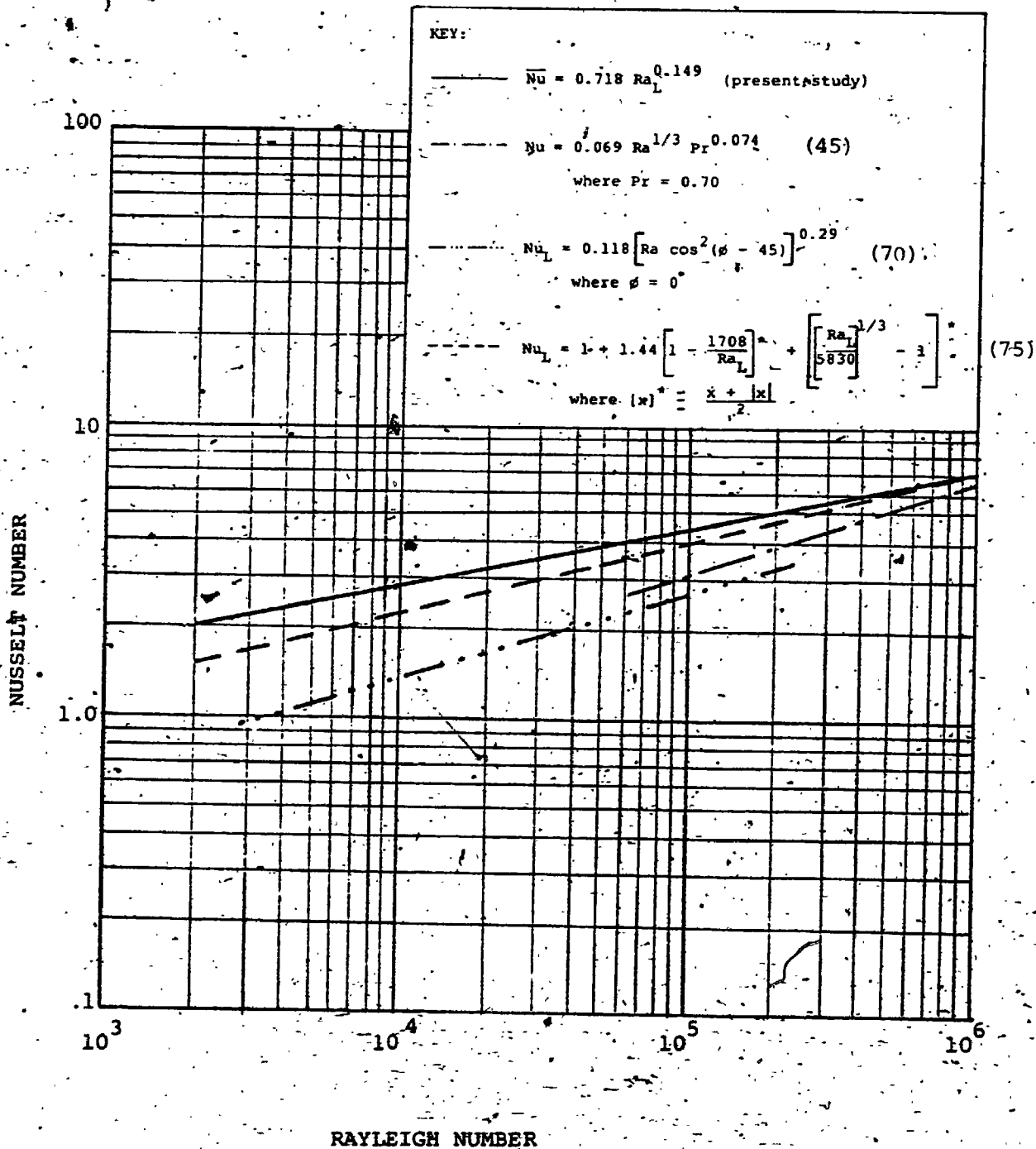


FIGURE 7.29 Comparison of Previous Correlations with the Result of the Present Investigation

heat losses through the top boundary of the cavity. The procedure is described in Appendix C.

7.4.1 Forced Convection Data Correlation

In Chapter II, the non-dimensional mathematical governing equations of heat transfer by forced convection over the surface of the glazing were introduced. From these equations, it was concluded that the rate of heat transfer by forced convection was dependent on non-dimensional parameters such as the Prandtl number and the Reynolds number, since the Prandtl number was constant during this investigation. The Reynolds numbers were correlated with the results of the forced convection film coefficients, calculated from the heat losses through the top boundary, the cold plate, as discussed in Appendix D. The statistical computer analysis program, FASTFIT, provided the following regression equation for the wind related heat transfer coefficient:

$$\bar{h}_{w_i} = 0.039 \text{ Re}_{L_c}^{0.436} \quad (7.4.1.1)$$

with an average percent error of 2.4 where L_c is the characteristic length of the surface as defined before. This equation can be written in a non-dimensional form of Nusselt number as

$$\bar{Nu} = 0.731 Re_{L_c}^{0.436} \quad (7.1.2.2)$$

presenting this equation in the form of Ramsey's [85] equation. The following equation can be obtained:

$$\bar{h}_W = 0.820 \frac{K}{L} Re_{L_c}^{0.436} Pr^{1/3} \quad (7.1.2.3)$$

or in a non-dimensional form, it becomes

$$\bar{Nu} = 0.820 Re_{L_c}^{0.436} Pr^{1/3} \quad (7.1.2.4)$$

The data was also correlated for $Re_{L_c}^{1/2} Pr^{1/3}$ as was assumed by Ramsey. The following equations resulted:

$$\bar{h}_W = 0.414 \frac{K}{L_c} Re_{L_c}^{1/2} Pr^{1/3} \quad (7.1.2.5)$$

with an average percent error of 3.9. In a non-dimensional form this equation becomes

$$\bar{Nu} = 0.414 Re_{L_c}^{1/2} Pr^{1/3} \quad (7.1.2.6)$$

The present correlation is compared with the equation given by Ramsey in Figure 7.30. The results of the computer programs are given in Appendix B.

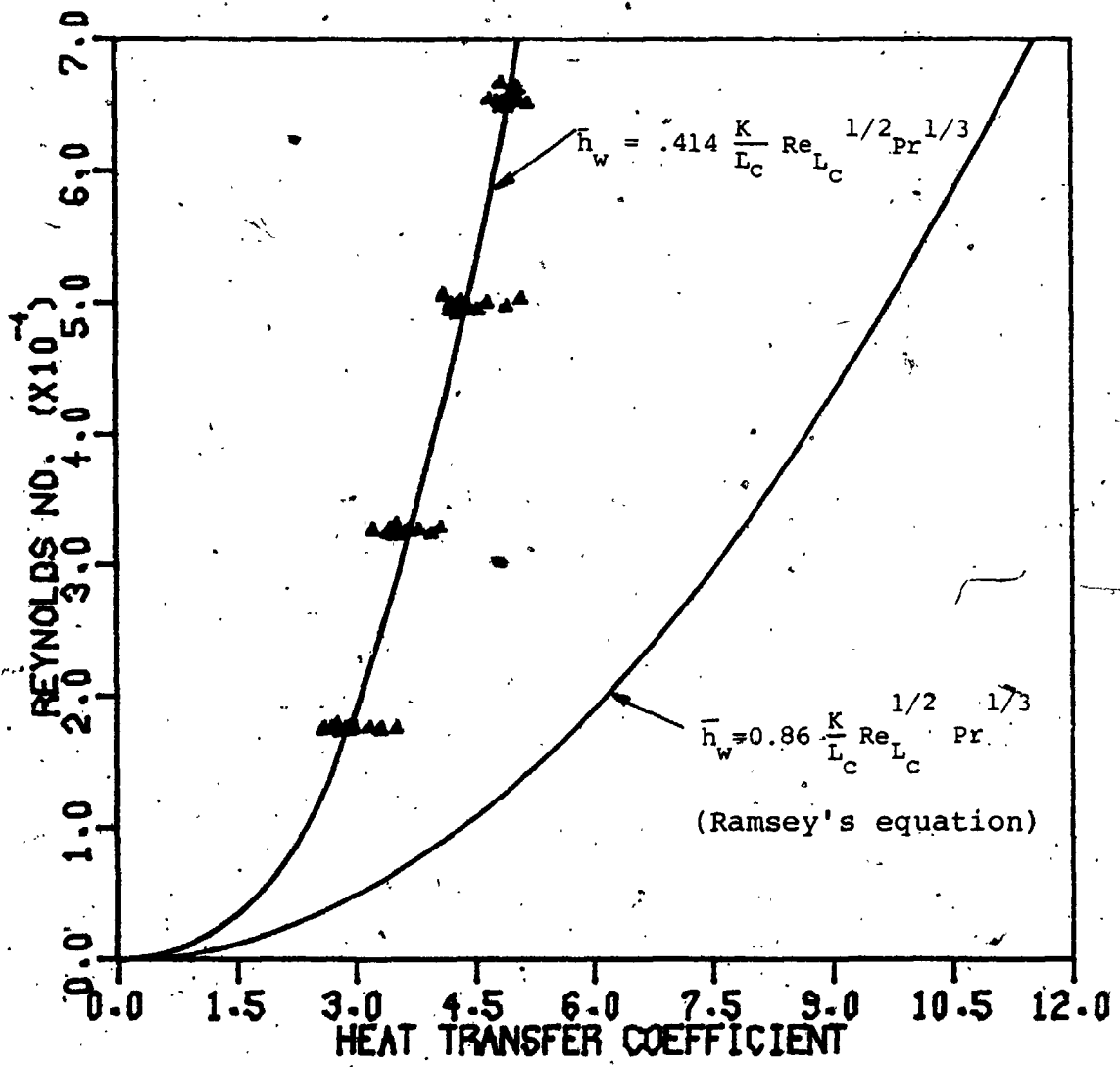


FIGURE 7.30 Plot of Reynolds Number as a function of Heat Transfer Coefficient

CHAPTER VIII

CONCLUSIONS AND RECOMMENDATIONS

The coupled convective flow phenomena in horizontal enclosed air layers with two opposed horizontal boundaries at different temperatures, where the bottom plate is isothermal and the top plate is exposed to exterior forced convection, are of a complex nature.

The parameters such as the bottom plate temperature, the thickness and the thermal conductivity of the top plate boundary, the nature of the flow and the exterior Reynolds number; the leading edge of the surface thermal boundary layer and the film coefficient near the bottom of the top plate boundary dictate the temperature distribution of the top plate. This is not an easily defined or predicted boundary. Consequently, the coupled-convective flow characteristic is highly complex and not easy to model or solve analytically.

A combined long path Mach-Zehnder interferometer-low speed wind tunnel was employed and proven to be satisfactory for simulating and studying some of these parameters affecting the solar collector performance. The apparatus and the model utilized in this investigation provided accurate, reliable and consistent

interferograms within the enclosure as well as on the surface of the top boundary with natural and forced convection. The interferograms yielded accurate temperature fields from which the local and overall Nusselt numbers were attainable. In light of the experimental limitations, the following results and conclusions can be made for each of the following flow conditions:

1. A technique was developed by which interferograms with finite and infinite fringe fields, on the same film negative, having the same boundary conditions were possible. The interferograms with finite fringe field proved to be more practical for analysis of temperature profiles while interferograms with infinite fringe field were utilized for flow visualization. The technique also proved to be practical and time saving when studying the coupled-convective heat transfer in the solar test model.
2. A critical Rayleigh number ($Ra_{crit.} = 1717$) was established for the onset of convective motion within the enclosure in the form of Benard cells. This numeric value agreed with the predicted Rayleigh number within 0.5%.
3. For Rayleigh number less than the critical Rayleigh number, heat transfer by conduction was predominant.

However, near the vertical boundaries, a weak convection was observed. For $Ra \geq Ra_{crit.}$, three distinct heat transfer regions were observed, mainly two conduction regions near the horizontal boundaries and one convection region in the centre of the cavity.

4. The horizontal and vertical temperature profiles within the cavity were plotted which showed the regions of heat transfer. The slopes of the vertical temperature profiles near the horizontal boundaries were negative and became progressively more negative as the Rayleigh number increased. However, in the central region where convection or flow rotation was predominant, the slope changed from negative to positive at about $Ra \geq 12000$ (see Figure 7.8). This phenomenon is known as the temperature reversal within the enclosure.
5. As the Rayleigh number increased, the Benard cell-height to width ratio decreased (see Figures 7.3d and 7.4f).
6. The temperature of the cold surface boundary was at no time isothermal. The temperature distribution was a maximum at the centre and had lower values near the edges. The temperature of the hot plate

remained isothermal to within $\pm 1.0^\circ\text{C}$ for the high heating rates and dropped to $\pm 0.2^\circ\text{C}$ for the low heating rates (see Figures 6.1 and 6.2).

7. As the Rayleigh number increased, due to the temperature reversal within the enclosure, convective rotation in the central region increased. However, the overall heat flux through the horizontal boundaries slightly decreased (see section 7.2.1).
8. The convection heat transfer equation within the enclosure (see section 7.3.3) was found to be

$$\overline{\text{Nu}} = 0.714 \text{ Ra}_L^{0.149}$$

with an average percent error of 5.1.

9. The exterior forced convection on the surface of the top boundary affected the temperature distribution of the plate. The temperature at the leading edge of the thermal boundary layer on the surface dropped more and as the boundary layer got thicker, the temperature drop was less pronounced (see Figure 6.2).
10. The coupling effect of forced convection heat transfer on the top surface boundary was found to moderately affect the natural convection within the

enclosure. This is seen in Figures 7.2c,d,e and f and Figures 7.15 to 7.18.

11. The heat transfer equation by forced convection over the top surface was found to be

$$\bar{h}_W = 0.039 \text{Re}_{L_c}^{0.436} \quad (\text{for Pr}=0.7)$$

or in a non-dimensional form as

$$\bar{Nu} = 0.731 \text{Re}_{L_c}^{0.436}$$

with the average percent error of 2.4 (see section 7.4.1).

The following recommendations are suggested for future studies:

1. The range of parameters such as the wind tunnel Reynolds number, the aspect ratio and the glazing thermal and physical characteristics should be extended to likely design values.
2. The nature of the exterior flow likely influences the overall heat transfer from the cavity. Further study is necessary to establish the cavity response to unheated starting lengths and flow direction.
3. The glazing thermal characteristics influence the overall cavity thermal response. A study is required

to establish how the glazing thermal conductivity and its thickness influence the coupled heat transfer characteristics.

4. There is need to develop a technique which would be capable of demonstrating the flow patterns for each flow regime. For example, a Laser-Doppler anemometer might yield useful information on the velocity fields while the cavity experiences a temperature reversal.

Finally, it is likely that a wide variety of wind situations are experienced by a solar collector. A study is necessary which would catalogue the most probable wind direction for a given collector location. Such information would allow for highly practical simulations in any additional studies as described in this thesis.

APPENDIX A

THE PHYSICAL PROPERTIES OF AIR

There are two parameters which affect the physical properties of air: temperature and pressure. In the case of natural convection, pressure variation is always small and assumed to be negligible, which also constitutes a state of constant temperature. Thus, the changes in physical properties of air are attributed to changes in temperature only.

The following are the equations employed in this investigation.

1. Dynamic Viscosity, μ

The temperature variation of the dynamic viscosity was adapted from the Sutherland formula [107]

$$\mu = C_1 \frac{T^{3/2}}{C_2 + T} \quad \text{Kg/m.s.}$$

where T is in °K,

$$C_1 = 1.4582 \times 10^{-6} \quad \text{Kg/m.s}^\circ\text{K}^{1/2}$$

and $C_2 = .110.39^\circ\text{K}$ for air at atmospheric pressure. The temperature range of this equation is between 280 to 1500°K.

2. Specific Heat, C_p

For evaluation of the specific heat of air at constant pressure, the equation was taken from the National Bureau of Standards [108]

$$C_p = 1.02432748 - 1.39785579 \times 10^{-4}T + 2.06057349 \times 10^{-7}T^2 + 2.00205 \times 10^{-10}T^3 \quad \text{KJ/Kg}^\circ\text{K}$$

where T is in $^\circ\text{K}$ and the temperature range is 250 to 410 $^\circ\text{K}$.

3. Thermal Conductivity, K

The temperature variation of thermal conductivity equation was presented [109] by

$$K = 7.4960 \times 10^{-5}T + 0.024204 \quad \text{W/m}^\circ\text{C}$$

where T is in $^\circ\text{C}$ and the temperature range is 0 to 150 $^\circ\text{C}$.

4. Coefficient of Thermal Expansion, β

By definition, as given in Eq. 2.1.11, the coefficient of thermal expansion of air is given by

$$\left. \frac{\partial \rho}{\partial T} \right|_p = -\rho\beta$$

For gases that may be considered to behave as ideal gases, such as air considered in this study, the coefficient of

thermal expansion is represented by

$$\beta = \frac{1}{T}$$

where T is the temperature in °K.

5. Refractive Index, n

The equation representing the general relation between the refractive index n and the density ρ is given by the Lorentz-Lorenz equation [110]

$$\frac{n^2 - 1}{\rho(n^2 + 2)} = f(\lambda)$$

Since air has a refractive index near unity, this equation can be represented as the Gladstone-Dale equation [110]

$$\frac{2(n-1)}{3\rho} = K$$

where K is the Gladstone-Dale constant. For the He-Ne laser with a wavelength of 6.328×10^{-7} m employed in this study, the constant K was 1.504×10^{-4} m²/Kg. The refractive index value was taken from the Critical Tables [111] at 20°C and 760 mm Hg as

$$n = 1.0002716$$

APPENDIX B

INTERFEROGRAM ANALYSIS

The long path difference Mach-Zehnder interferometer operates on the principle of a change in the refractive index of a fluid or gas due to a density gradient, which causes a disturbance in a coherent beam of light passed through it. This beam is then recombined with an undisturbed coherent reference beam to produce the phenomenon of light interference. The density gradients in the direction normal to the light path passing through a test section appear in the form of either finite or infinite fringe field interferograms. All density changes along a single beam are integrated by the interferometer. The advantage and disadvantage of each interferogram was presented in Chapter IV and the proper interferometer alignment for the formation of interference fringes was discussed in Chapter VI. The procedure for the determination of temperature, which was also considered by Randall [2], Hauf et al. [110] and Carlson [112] is discussed here.

For natural convective conditions, pressure variations are negligible and any changes in density which do take place are attributed to changes in temperature alone. The desired temperature distribution can then be determined by means of refractive index of the test medium compared

with the refractive index of the reference beam.

The optical path length is defined as the distance that light would travel in a vacuum for the same period of time that it takes the light to travel in a test medium. The difference between the two optical path lengths, travelling in the test medium and the reference medium are then expressed as follows:

$$\Delta S = nW - n_0 W \quad (B.1)$$

where n = refractive index of test medium

n_0 = refractive index of reference medium

W = width of the test medium in the direction of the light beam.

The above equation can be written for the transverse variation of the refractive index to the light path direction by

$$\Delta S(x,y) = \int_0^W [n(x,y) - n_0] dz \quad (B.2)$$

where x, y are transverse coordinates to the light beam, and z is coordinate in the direction of the light beam. Since both light beams travel in the form of wave trains, the difference between the optical path lengths can be presented in terms of wavelengths which represent the finite fringe shifts. Thus,

$$F_{sh}(x,y) = \frac{1}{\lambda} \int_0^W [n(x,y) - n_0] dz \quad (B.3)$$

where $F_{sh}(x,y)$ is the fringe shift in the test medium, and λ is the wavelength of the light source, or

$$F_{sh}(x,y) = \frac{W}{\lambda} [n(x,y) - n_0] \quad (B.4)$$

The refractive index of a homogeneous, transparent medium is a function of density and is given by the Lorentz-Lorenz equation [110] as

$$\frac{n^2 - 1}{\rho(n^2 + 2)} = f(\lambda) \quad (B.5)$$

Since air has a refractive index near unity, $n = 1.0002716$, then

$$\frac{2(n-1)}{3\rho} = G \quad (B.6)$$

where G is the Gladstone-Dale constant.

This study was conducted for air in an enclosure which was at atmospheric pressure and temperature varied between 20°C to 95°C. Over the temperature variation it was therefore assumed that air behaved as an ideal gas. Thus, the ideal gas law may be used:

$$\rho = \frac{P}{RT} \quad (B.7)$$

where ρ = density

P = absolute pressure

R = universal gas constant, and

T = absolute temperature

Upon the substitution of Eq. B.7 into Eq. B.6, the following equation is obtained:

$$\frac{2(n-1)RT}{3P} = G \quad (B.8)$$

Also, by substituting Eq. B.8 into Eq. B.4, the following equation represents the fringe shift between two absolute temperatures:

$$F_{sh}(x,y) = \frac{3GWP}{2\lambda R} \left[\frac{1}{T(x,y)} - \frac{1}{T_0} \right] \quad (B.9)$$

Equation B.9 can be rearranged such that temperature at a specific location in the enclosure can be obtained as follows:

$$T(x,y) = \frac{3GWT_0 P}{3GWP + 2F(x,y)\lambda RT_0} \quad (B.10)$$

Equation B.10 requires that the fringe shift at specific location of X/H, for two known absolute temperatures within the enclosure, be calculated first. This was accomplished by substituting the two known measured temperatures of the hot (T_H) and cold (T_{CB}) plates, as reference temperatures, into Eq. B.9. At the location $X/H = X_1$, the number of fringes and their values of Y/L were recorded.

A third order polynomial of the form,

$$F_{sh} \left(\frac{X}{H} = X_1, Y/L \right) = A + B(Y/L) + C(Y/L)^2 + D(Y/L)^3$$

where A, B, C and D are the polynomial constants, which were fit to the data by a computer program which provided the plot of a shifted fringe. A straight line was passed from the hot plate with a zero fringe shift to the cold plate where the maximum fringe shift occurred. This line represents the reference fringe if the hot plate were not heated.

As it was discussed previously, fourteen X/H values (0.0075, 0.0225, 0.045, 0.0675, 0.1775, 0.3175, 0.4325, 0.5675, 0.6825, 0.8225, 0.9325, 0.9550, 0.9775 and 0.9925) were chosen for the entire enclosure, which was scanned from the hot plate to the cold plate. The vertical temperatures were then calculated after finding the proper fringe shifts at these locations, and for Y/L from 0.0 (hot plate) to 1.0 (cold plate) with an increment of 0.05. At $X/H = X_1$, the fringe shift at $Y/L = Y_1$ was found by subtracting the value of the reference fringe from the respective value of the plotted fringe. This fringe shift value was then substituted into Eq. B.10 which provided the temperature at $X/H = X_1$ and $Y/L = Y_1$. The computer program furnished a total of 294 temperature points within

the cavity for a complete temperature map.

A sample of the computer program with the results of one data set is included.

```

*****
*
*   F A S T F I T   R U N
*
*   RUN DATE - 83/01/08
*   TIME     - 11.57.50
*   REVISION - 1982/09/01
*
*****

```

FORCED CONVECTION HEAT TRANSFER CORRELATION

LINEARIZED EQUATION TYPE

THE FORM OF THE FITTED EQUATION IS :

```

      A LOG(HW)
      + COEFF. A * 1
      + COEFF. B * LOG(Re)

```

RELATIVE ERROR TO BE CALCULATED

DATA POINTS ARE NOT INDIVIDUALLY WEIGHTED

```

NUMBER OF VARIABLES IN EQUATION = 2
NUMBER OF FITTED CONSTANTS = 2
NUMBER OF POINTS FITTED = 48

```

```

*****
*
*   F A S T F I T   R U N
*
*   RUN DATE - 83/21/78
*   TIME     - 11.57.50
*   REVISION - 1982/29/71
*
*****

```

FORCED CONVECTION HEAT TRANSFER CORRELATION

THE COEFFICIENTS FOR THE EQUATION ARE

```

A = -3.839754
B = 4.352244

```

DEPENDENT TERM MEASURED	TERM CALC.	PERCENT ERROR	WEIGHT	ALL VARIABLES HW	RE
.958	1.02	-6.76	1.00	2.61	1.754E+24
1.23	1.29	-4.84	1.00	3.43	3.262E+24
1.43	1.47	-2.87	1.00	4.19	4.954E+24
1.59	1.59	-4.94	1.00	4.89	6.533E+24
1.25	1.29	-3.91	1.00	3.47	3.283E+24
1.44	1.48	-2.26	1.00	4.24	4.989E+24
1.52	1.60	.180	1.00	4.95	6.574E+24
1.26	1.02	3.58	1.00	2.89	1.772E+24
1.31	1.29	1.12	1.00	3.70	3.274E+24
1.47	1.48	-.682	1.00	4.34	5.016E+24
1.62	1.60	1.37	1.00	5.07	6.627E+24
1.31	1.29	1.35	1.00	3.71	3.275E+24
1.59	1.48	7.42	1.00	4.92	4.977E+24
1.63	1.59	2.27	1.00	5.09	6.534E+24
1.22	1.02	.586	1.00	2.79	1.745E+24
1.43	1.29	-4.93	1.00	3.42	3.259E+24
1.43	1.47	-2.77	1.00	4.19	4.953E+24
1.57	1.59	-1.39	1.00	4.82	6.530E+24
1.79	1.82	5.97	1.00	2.97	1.767E+24
1.25	1.29	3.42	1.00	3.47	3.238E+24
1.45	1.47	-.619	1.00	4.32	4.937E+24
1.62	1.59	.403	1.00	4.94	6.496E+24
1.73	1.82	5.39	1.00	2.95	1.763E+24
1.32	1.29	.431	1.00	3.66	3.264E+24
1.48	1.47	.367	1.00	4.39	4.948E+24
1.55	1.60	-2.92	1.00	4.71	6.548E+24
1.98	1.63	-2.74	1.00	2.71	1.771E+24
1.41	1.30	8.02	1.00	4.09	3.293E+24
1.34	1.48	4.31	1.00	4.68	5.000E+24
1.22	1.02	7.999E-03	1.00	2.79	1.770E+24
1.24	1.29	-4.35	1.00	3.45	3.272E+24
1.49	1.47	.479	1.00	4.40	4.954E+24
1.62	1.59	.575	1.00	4.97	6.543E+24
1.22	1.23	-.583	1.00	2.79	1.793E+24
1.26	1.30	-2.74	1.00	3.54	3.314E+24
1.42	1.48	-4.37	1.00	4.14	5.062E+24
1.50	1.62	-1.52	1.00	4.85	6.672E+24
1.15	1.29	-2.64	1.00	3.51	3.232E+24
1.50	1.47	-.822	1.00	4.30	4.915E+24
1.56	1.59	-.574	1.00	4.86	6.489E+24
1.22	1.29	-.627	1.00	3.60	3.239E+24
1.41	1.47	-1.24	1.00	4.28	4.913E+24
1.62	1.59	3.33	1.00	5.19	6.512E+24
1.34	1.29	3.49	1.00	3.82	3.281E+24
1.49	1.48	.829	1.00	4.43	4.988E+24
1.61	1.60	.829	1.00	5.22	6.572E+24
1.62	1.47	2.93	1.00	4.56	4.945E+24
1.62	1.59	.513	1.00	4.96	6.518E+24

AVERAGE PERCENT ERROR = 2.4
 AVERAGE ERROR = 3.21E-02
 MAXIMUM PERCENT ERROR = 8.7
 MAXIMUM ERROR = 1.18E-01

FORCED CONVECTION HEAT TRANSFER CORRELATION

RESULTS SUMMARY

LHS CALCULATED

MINIMUM VALUE 0.958

MAXIMUM VALUE 1.05

INCREMENT VALUE 0.01

PROGRAM: PASEK

157 23 01 1961

FILE: 4.8.552

SHIFT=(H-H0)/LAMBDA*(1+D)*T0*3+CC*P1**3
SHIFT=(H-H0)/LAMBDA*(1+D)*T0*3

NOW THE FLIP ANGLE CAN BE CAL. BY THE NET FRINGE SHIFT

WUTD=4.5/2
DLN=1.328L-1
D12=1.504L-3
T=TH/(12.*Y*DLN*(H0+TH)/(3.*WUTD*DN*PAMB*101325/760)+1.0)
TUTL(JJ)=(1-TL)/(TH-TL)

THE NEXT IF SECTION DO N TO ST.#15 IS CALCULATING THE
PARTIAL DER. OF INFLA. IN THE NON-DIM. DIST. Y/L
DUE TO A SECOND ORDER FORWARD DIFFERENCE FORMULA
THE FINAL EXPRESSION, D1 IS THE SLOPE, USED IMMEDIATELY
TO CALCULATE THE LOCAL FUSSEL NO. AT THE WALL (UNUL)

*IF (PI.GT.0) GO TO 15
A1=0.050
X=0.1
Y1=(H-H0)*A1*CC*A1*(1+D)*A1*(1+D)
Y2=(H-H0)*A2*CC*A2*(1+D)*A2*(1+D)
T1=TH/(12.*Y*DLN*(H0+TH)/(3.*WUTD*DN*PAMB*101325/760)+1.0)
Y1=TH*(12.*Y*DLN*(H0+TH)/(3.*WUTD*DN*PAMB*101325/760)+1.0)
T2=(Y1-TL)/(TH-TL)
Y2=(Y2-TL)/(TH-TL)
D1=(Y2-Y1)/(1+D)
UNUL=DN/D1*(1+D)
A1=0.050
X=0.1
Y1=(H-H0)*A1*CC*A1*(1+D)*A1*(1+D)
Y2=(H-H0)*A2*CC*A2*(1+D)*A2*(1+D)
T1=TH/(12.*Y*DLN*(H0+TH)/(3.*WUTD*DN*PAMB*101325/760)+1.0)
Y1=TH*(12.*Y*DLN*(H0+TH)/(3.*WUTD*DN*PAMB*101325/760)+1.0)
T2=(Y1-TL)/(TH-TL)
Y2=(Y2-TL)/(TH-TL)
D1=(Y2-Y1)/(1+D)
UNUL=DN/D1*(1+D)
ALUL=ALUL*1000

WRITE(7,88)ALUL,A1,D1,E,MM,IGHL,HAL,DORA,RAX,DNUL,UNUL
ON PWB AT (2A,"ALUL="F3.1," MM",5X,"NON-DIM. DISTANCE",F3.5X,
10R="E10.4,5X,MM",F3.5,2X,"UNUL",E10.4,5X,"HAL",
10R="E10.4,5X,MM",F3.5,2X,"RAX",E10.4,5X,"DNUL",F3.5,
10R="UNUL",F3.5)

WRITE(7,89)
FORM AT (2A,"TOTAL FRINGE SHIFT",F1.4,2//)
WRITE(7,90)INDEA
FORM AT (2A,"SELECTION",LAMP#,11,1,2//)
WRITE(7,91)
FORM AT (3A,"DIST",5L,"LUC",5X,"SHIFT",3A,
10R="SA",10R="T(L)A")
WRITE(7,92)
FORM AT (2A,"INFLA",3X,"(L)",2//)

FIN 4.8*552

FIN 4.8*552

```

CALL PLUT(AA(1)/U.2,THE1(1)/U.2,3)
CALL PLUT(AA(1)/U.2,THE2(1)/U.2,3)
CALL PLUT(AA(1)/U.2,THE3(1)/U.2,3)
CALL PLUT(AA(1)/U.2,THE4(1)/U.2,3)
CALL PLUT(AA(1)/U.2,THE5(1)/U.2,3)
CALL PLUT(AA(1)/U.2,THE6(1)/U.2,3)
CALL PLUT(AA(1)/U.2,THE7(1)/U.2,3)
CALL PLUT(AA(1)/U.2,THE8(1)/U.2,3)
CALL PLUT(AA(1)/U.2,THE9(1)/U.2,3)
CALL PLUT(AA(1)/U.2,THE10(1)/U.2,3)
CALL PLUT(AA(1)/U.2,THE11(1)/U.2,3)
CALL PLUT(AA(1)/U.2,THE12(1)/U.2,3)
CALL PLUT(AA(1)/U.2,THE13(1)/U.2,3)
CALL PLUT(AA(1)/U.2,THE14(1)/U.2,3)
CALL PLUT(AA(1)/U.2,THE15(1)/U.2,3)
CALL PLUT(AA(1)/U.2,THE16(1)/U.2,3)
CALL PLUT(AA(1)/U.2,THE17(1)/U.2,3)
CALL PLUT(AA(1)/U.2,THE18(1)/U.2,3)
CALL PLUT(AA(1)/U.2,THE19(1)/U.2,3)
CALL PLUT(AA(1)/U.2,THE20(1)/U.2,3)
CALL SYMUL(1.0,0.35,125,0,EXPERIMENTAL TEMP. PROFILE,0,20)
CALL SYMUL(5.0,0.35,125,0,EXPERIMENTAL HORIZONTAL TEMP. PROFILE,0,37)
CALL SYMUL(5.35,4.0,10,4,0,0,3)
CALL SYMUL(5.30,4.6,10,4,0,0,-1)
CALL SYMUL(5.6,4.0,10,4,0,0,0,4)
CALL SYMUL(5.30,4.0,10,4,0,-1)
CALL SYMUL(5.6,4.4,10,4,0,10,0,4)
CALL SYMUL(5.30,4.2,10,4,0,-1)
CALL SYMUL(5.6,4.2,10,4,0,25,0,4)
CALL SYMUL(5.30,4.0,10,4,0,-1)
CALL SYMUL(5.6,4.0,10,4,0,35,0,4)
CALL SYMUL(5.30,3.8,10,4,0,-1)
CALL SYMUL(5.6,3.0,10,4,0,5,0,4)
CALL SYMUL(5.30,3.0,10,4,0,-1)
CALL SYMUL(5.6,3.6,10,4,0,50,0,4)
CALL SYMUL(5.30,3.0,10,4,0,-1)
CALL SYMUL(5.6,3.6,10,4,0,55,0,4)
CALL SYMUL(5.30,3.4,10,4,0,-1)
CALL SYMUL(5.6,3.4,10,4,0,65,0,4)
CALL SYMUL(5.30,3.2,10,4,0,-1)
CALL SYMUL(5.6,3.2,10,4,0,75,0,4)
CALL SYMUL(5.30,3.0,10,4,0,-1)
CALL SYMUL(5.6,3.0,10,4,0,85,0,4)
CALL SYMUL(5.30,2.8,10,4,0,-1)
CALL SYMUL(5.6,2.8,10,4,0,95,0,4)
CALL SYMUL(0.1,0.0,0,125,4,MS C,0,4)
CALL SYMUL(0.27,5.75,0.10,1M1,0,1)
CALL SYMUL(0.27,5.55,0.10,1M2,0,1)
CALL SYMUL(0.27,5.35,0.10,1M3,0,1)
CALL SYMUL(0.27,5.15,0.10,1M4,0,1)

```


FTN 4.8-552 83/01/03. 15.25.38

INVALID 4TH PARAMETER IN CALL TO VALD (0000)
 4TH OUTPUT INDICATED

INVALID 12TH PARAMETER IN CALL TO VALD (0000)
 12TH OUTPUT INDICATED

INVALID 13TH PARAMETER IN CALL TO VALD (0000)
 13TH OUTPUT INDICATED

TIME 2.9000 T=23.0700 TCR=21.9000 TAMD=21.90 PAMB=.735.0MM HG
 A.P.C.T. MATH=17.000 TILL ANGLE= J.V. VEL=2.200M/S DIST BETWEEN PLATES=25.4000 MM
 # 357333 15.942100 -23.280306 13.3344605

ALU= 3.5 MG NORMIN DISINCE= .000 MEZ .64/2L+05 PR= .709 NULCM=1.8623
 G.L.= 12.20005 MALS .0017100 UNAS =2.11E+02 MAX= .1992E+02 NUL=3.7973
 TOTAL FRICTION SHIP= 3.0073

SECTIONAL SCANS (1)

YLOC	YLOC	SHIFT	TEMP	THETA
0.000	0.000	0.000	17.900	10000
0.500	0.500	0.627	18.875	0269
1.000	1.000	1.139	18.032	0043
1.500	1.500	1.559	17.337	0009
2.000	2.000	1.892	16.809	0775
2.500	2.500	2.154	16.311	0473
3.000	3.000	2.346	15.836	0352
3.500	3.500	2.474	15.380	0300
4.000	4.000	2.535	14.933	0246
4.500	4.500	2.573	14.500	0184
5.000	5.000	2.583	14.081	0133
5.500	5.500	2.553	13.685	0077
6.000	6.000	2.484	13.311	0028
6.500	6.500	2.380	12.956	0008
7.000	7.000	2.244	12.622	0002
7.500	7.500	2.079	12.307	0000
8.000	8.000	1.887	12.012	0000
8.500	8.500	1.670	11.737	0000
9.000	9.000	1.428	11.482	0000
9.500	9.500	1.164	11.247	0000
10.000	10.000	0.880	11.032	0000

.....

TMINU=22.70 PAMB= 735.0MM HG
 DIST BETWEEN PLATES=25.4000 MM
 TAMB=21.90
 VELM=2.200M/S
 17.0877028

TCT=23.700 ICD=21.7000
 TAMB=21.90
 VELM=2.200M/S
 17.0877028

ALPH=0.0100 DISTANCE=0.23 PH=0.709
 DIST=0.2300 RAX=0.912003 RAX=0.580E+03 NUL=3.7366 NULCM=2.9086
 TOTAL PRESSURE SHIP=3.5575

SECTIONAL ANALYSIS

DISP	YLOC	SCALE	TEMP	PLATE
10.000	0.0000	0.000000	21.700	1.000
10.250	0.0000	0.000000	20.7054	0.975
10.500	0.0000	1.000000	20.8150	0.950
10.750	0.0000	1.500000	21.0000	0.925
11.000	0.0000	2.000000	21.1700	0.900
11.250	0.0000	2.500000	21.3300	0.875
11.500	0.0000	3.000000	21.4800	0.850
11.750	0.0000	3.500000	21.6200	0.825
12.000	0.0000	4.000000	21.7500	0.800
12.250	0.0000	4.500000	21.8700	0.775
12.500	0.0000	5.000000	21.9800	0.750
12.750	0.0000	5.500000	22.0800	0.725
13.000	0.0000	6.000000	22.1700	0.700
13.250	0.0000	6.500000	22.2500	0.675
13.500	0.0000	7.000000	22.3200	0.650
13.750	0.0000	7.500000	22.3800	0.625
14.000	0.0000	8.000000	22.4300	0.600
14.250	0.0000	8.500000	22.4700	0.575
14.500	0.0000	9.000000	22.5000	0.550
14.750	0.0000	9.500000	22.5200	0.525
15.000	0.0000	10.000000	22.5300	0.500
15.250	0.0000	10.500000	22.5300	0.475
15.500	0.0000	11.000000	22.5200	0.450
15.750	0.0000	11.500000	22.5000	0.425
16.000	0.0000	12.000000	22.4700	0.400
16.250	0.0000	12.500000	22.4300	0.375
16.500	0.0000	13.000000	22.3800	0.350
16.750	0.0000	13.500000	22.3200	0.325
17.000	0.0000	14.000000	22.2500	0.300
17.250	0.0000	14.500000	22.1700	0.275
17.500	0.0000	15.000000	22.0800	0.250
17.750	0.0000	15.500000	21.9800	0.225
18.000	0.0000	16.000000	21.8700	0.200
18.250	0.0000	16.500000	21.7500	0.175
18.500	0.0000	17.000000	21.6200	0.150
18.750	0.0000	17.500000	21.4800	0.125
19.000	0.0000	18.000000	21.3300	0.100
19.250	0.0000	18.500000	21.1700	0.075
19.500	0.0000	19.000000	21.0000	0.050
19.750	0.0000	19.500000	20.8150	0.025
20.000	0.0000	20.000000	20.7054	0.000

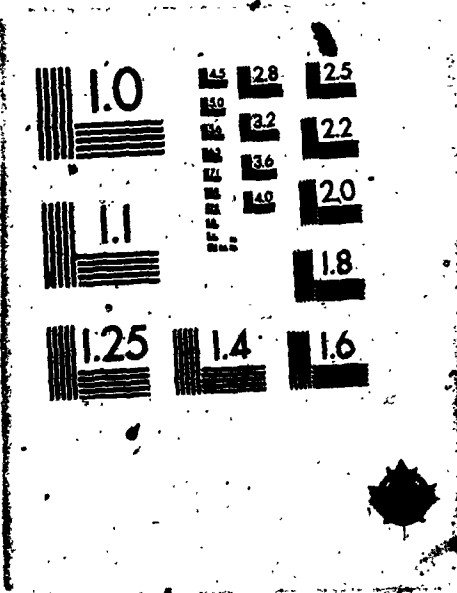
INR=9.4007 IRT=23.0700 ICR=23.0500 TAMB=21.90 TMINU=22.70 PAMB= 735.0MM HG
 ASPECT RATIO=17.1000 TILT ANGLE= 0.0 VEL=2.260M/S DIST: BETWEEN PLATES=25.4000 MM
 277199 14.179749 -23.493351 14.986762
 200336
 ALICE 200000 NON-DIM DISTANCE= 0.00 MEZ .6472E+05 PR= .709 NULCW=2.6775
 GRES .12E+05 PALZ .001E+04 UNAZ .6344E+04 RAAZ .4567E+04 NUL=3.3964
 TOTAL FRIDGE SHIFTS 3.2573

SECTIONAL SCHEMATIC

YLOC	YLOC	SHIF	TEMP	THEIA
(MM)	(MM)		(C)	
0.0000	0.0000	0.0000	29.9000	1.0000E
1.271	.5514	28.9925	.8947	
2.543	.9005	28.2036	.8726	
3.814	1.3400	27.6931	.8272	
5.086	1.8130	27.3003	.8591	
6.357	1.8000	26.9401	.8010	
7.629	1.9392	26.7316	.8698	
8.900	2.0001	26.5901	.9423	
10.172	2.0004	26.5274	.9313	
11.443	2.0621	26.5012	.9254	
12.715	2.0821	26.5113	.9259	
13.986	2.0770	26.5090	.9273	
15.258	2.0700	26.5074	.9270	
16.529	2.0695	26.4961	.9260	
17.801	2.0693	26.49021	.9261	
19.072	2.0690	26.4810	.9264	
20.344	2.0687	26.4694	.9274	
21.615	2.0680	26.4571	.9284	
22.887	2.0670	26.4441	.9294	
24.158	2.0660	26.4301	.9304	
25.430	2.0650	26.4151	.9314	
26.701	2.0640	26.4001	.9324	
27.973	2.0630	26.3841	.9334	
29.244	2.0620	26.3681	.9344	
30.516	2.0610	26.3521	.9354	
31.787	2.0600	26.3361	.9364	
33.059	2.0590	26.3201	.9374	
34.330	2.0580	26.3041	.9384	
35.602	2.0570	26.2881	.9394	
36.873	2.0560	26.2721	.9404	
38.145	2.0550	26.2561	.9414	
39.416	2.0540	26.2401	.9424	
40.688	2.0530	26.2241	.9434	
41.959	2.0520	26.2081	.9444	
43.231	2.0510	26.1921	.9454	
44.502	2.0500	26.1761	.9464	
45.774	2.0490	26.1601	.9474	
47.045	2.0480	26.1441	.9484	
48.317	2.0470	26.1281	.9494	
49.588	2.0460	26.1121	.9504	
50.860	2.0450	26.0961	.9514	
52.131	2.0440	26.0801	.9524	
53.403	2.0430	26.0641	.9534	
54.674	2.0420	26.0481	.9544	
55.946	2.0410	26.0321	.9554	
57.217	2.0400	26.0161	.9564	
58.489	2.0390	26.0001	.9574	
59.760	2.0380	25.9841	.9584	
61.032	2.0370	25.9681	.9594	
62.303	2.0360	25.9521	.9604	
63.575	2.0350	25.9361	.9614	
64.846	2.0340	25.9201	.9624	
66.118	2.0330	25.9041	.9634	
67.389	2.0320	25.8881	.9644	
68.661	2.0310	25.8721	.9654	
69.932	2.0300	25.8561	.9664	
71.204	2.0290	25.8401	.9674	
72.475	2.0280	25.8241	.9684	
73.747	2.0270	25.8081	.9694	
75.018	2.0260	25.7921	.9704	
76.290	2.0250	25.7761	.9714	
77.561	2.0240	25.7601	.9724	
78.833	2.0230	25.7441	.9734	
80.104	2.0220	25.7281	.9744	
81.376	2.0210	25.7121	.9754	
82.647	2.0200	25.6961	.9764	
83.919	2.0190	25.6801	.9774	
85.190	2.0180	25.6641	.9784	
86.462	2.0170	25.6481	.9794	
87.733	2.0160	25.6321	.9804	
89.005	2.0150	25.6161	.9814	
90.276	2.0140	25.6001	.9824	
91.548	2.0130	25.5841	.9834	
92.819	2.0120	25.5681	.9844	
94.091	2.0110	25.5521	.9854	
95.362	2.0100	25.5361	.9864	
96.634	2.0090	25.5201	.9874	
97.905	2.0080	25.5041	.9884	
99.177	2.0070	25.4881	.9894	
100.448	2.0060	25.4721	.9904	
101.720	2.0050	25.4561	.9914	
102.991	2.0040	25.4401	.9924	
104.263	2.0030	25.4241	.9934	
105.534	2.0020	25.4081	.9944	
106.806	2.0010	25.3921	.9954	
108.077	2.0000	25.3761	.9964	
109.349	2.0000	25.3601	.9974	
110.620	2.0000	25.3441	.9984	
111.892	2.0000	25.3281	.9994	
113.163	2.0000	25.3121	1.0000	

3 3

OF / DE



TAND=21.90 PAMB= 735.0MM HG
 DIST BETWEEN PLATES=25.4000 MM
 TEND=22.70 PAMB= 735.0MM HG
 DIST BETWEEN PLATES=25.4000 MM
 TAND=21.90 PAMB= 735.0MM HG
 VEL=2.240M/S
 1C=5542487
 12.57500000 -19.6530740
 1.02248
 NON-DIAL DISTANCE = 1170 HZ = 6472E+05 PH = 709
 UNK = .3127E+06 RAX = .2641E+06 NUL=3.0033 NULCW=2.4106
 UNK = .3127E+06 RAX = .2641E+06 NUL=3.0033 NULCW=2.4106
 Initial Phase Shifts = 2.2573

SECTIONAL SCANS (15)

DIST (mm)	YLOC	YOFF	TEMP (C)	THEIA
0.000	0.000	0.000	29.970	1.000
1.000	0.000	0.000	29.970	1.000
2.000	0.000	0.000	29.970	1.000
3.000	0.000	0.000	29.970	1.000
4.000	0.000	0.000	29.970	1.000
5.000	0.000	0.000	29.970	1.000
6.000	0.000	0.000	29.970	1.000
7.000	0.000	0.000	29.970	1.000
8.000	0.000	0.000	29.970	1.000
9.000	0.000	0.000	29.970	1.000
10.000	0.000	0.000	29.970	1.000
11.000	0.000	0.000	29.970	1.000
12.000	0.000	0.000	29.970	1.000
13.000	0.000	0.000	29.970	1.000
14.000	0.000	0.000	29.970	1.000
15.000	0.000	0.000	29.970	1.000
16.000	0.000	0.000	29.970	1.000
17.000	0.000	0.000	29.970	1.000
18.000	0.000	0.000	29.970	1.000
19.000	0.000	0.000	29.970	1.000
20.000	0.000	0.000	29.970	1.000
21.000	0.000	0.000	29.970	1.000
22.000	0.000	0.000	29.970	1.000
23.000	0.000	0.000	29.970	1.000
24.000	0.000	0.000	29.970	1.000
25.000	0.000	0.000	29.970	1.000
26.000	0.000	0.000	29.970	1.000
27.000	0.000	0.000	29.970	1.000
28.000	0.000	0.000	29.970	1.000
29.000	0.000	0.000	29.970	1.000
30.000	0.000	0.000	29.970	1.000

.....

IMP: 7.9400 F: 12.4100 L: 24.100 I: 1000=21.90 PAMB= 735.0MM MM
 DIST BETWEEN PLATES=25.4000 MM
 DIST: 21.90 VAL: 2.210M/S MC: 6472E-05 PH: .709
 I: 1.000 L: 2.000 VAL: 1.000 MC: 1.000 RAA: .3765E+07 NULC=2.3392
 TOTAL FRINGE SHIFTS= 3.0000

SECTIONAL SCANS#2

YLOC	YUC	SHIF.	SLIP	DELTA
0.0000	0.0000	0.0000	0.0000	1.0000
1.0000	0.0000	0.0000	0.0000	0.0000
2.0000	0.0000	0.0000	0.0000	0.0000
3.0000	0.0000	0.0000	0.0000	0.0000
4.0000	0.0000	0.0000	0.0000	0.0000
5.0000	0.0000	0.0000	0.0000	0.0000
6.0000	0.0000	0.0000	0.0000	0.0000
7.0000	0.0000	0.0000	0.0000	0.0000
8.0000	0.0000	0.0000	0.0000	0.0000
9.0000	0.0000	0.0000	0.0000	0.0000
10.0000	0.0000	0.0000	0.0000	0.0000
11.0000	0.0000	0.0000	0.0000	0.0000
12.0000	0.0000	0.0000	0.0000	0.0000
13.0000	0.0000	0.0000	0.0000	0.0000
14.0000	0.0000	0.0000	0.0000	0.0000
15.0000	0.0000	0.0000	0.0000	0.0000
16.0000	0.0000	0.0000	0.0000	0.0000
17.0000	0.0000	0.0000	0.0000	0.0000
18.0000	0.0000	0.0000	0.0000	0.0000
19.0000	0.0000	0.0000	0.0000	0.0000
20.0000	0.0000	0.0000	0.0000	0.0000
21.0000	0.0000	0.0000	0.0000	0.0000
22.0000	0.0000	0.0000	0.0000	0.0000
23.0000	0.0000	0.0000	0.0000	0.0000
24.0000	0.0000	0.0000	0.0000	0.0000
25.0000	0.0000	0.0000	0.0000	0.0000
26.0000	0.0000	0.0000	0.0000	0.0000
27.0000	0.0000	0.0000	0.0000	0.0000
28.0000	0.0000	0.0000	0.0000	0.0000
29.0000	0.0000	0.0000	0.0000	0.0000
30.0000	0.0000	0.0000	0.0000	0.0000

.....

INP=9.940 T=1=23.700 ICUZC=1.000 TAMB=21.80 TWIND=22.60 PAMB= 735.0MM HB
 ASPECT RATIO=17.700 FILL ANGLE= 0.0 VEL=2.260M/S DISI BETWEEN PLATES=25.4000 MM
 17.700 15.2414/25 -10.0830631 11.8518752
 ALVE 75.01 MM FOR=14M DIS/ANGL= 508 REC =.6175E+05 PR= .709 NUL=2.9565 NULCM=2.3128
 GPM .114E+05 HALE .4352E+04 GMA= .1700E+08 MAX= .6505E+07
 TOTAL FRINGE SHIFTS 3.0000

SECTIONAL SCANS (1)

DIST (mm)	YLOC	SHIF	JUMP (C)	INTRA
0.000	0.0000	0.0000	29.9400	1.0000
1.070	.0500	.0700	29.1550	.8050
2.140	.1000	.1400	28.3122	.7555
3.210	.1500	.2100	27.5958	.6870
4.280	.2000	.2800	27.0000	.5974
5.350	.2500	.3500	26.5773	.5000
6.420	.3000	.4200	26.2800	.4000
7.490	.3500	.4900	26.0700	.3000
8.560	.4000	.5600	25.9200	.2000
9.630	.4500	.6300	25.8200	.1000
10.700	.5000	.7000	25.7700	.0000
11.770	.5500	.7700	25.7600	.0000
12.840	.6000	.8400	25.7800	.0000
13.910	.6500	.9100	25.8200	.0000
14.980	.7000	.9800	25.8800	.0000
16.050	.7500	1.0500	25.9500	.0000
17.120	.8000	1.1200	26.0300	.0000
18.190	.8500	1.1900	26.1200	.0000
19.260	.9000	1.2600	26.2200	.0000
20.330	.9500	1.3300	26.3300	.0000
21.400	1.0000	1.4000	26.4500	.0000
22.470	1.0500	1.4700	26.5800	.0000
23.540	1.1000	1.5400	26.7200	.0000
24.610	1.1500	1.6100	26.8700	.0000
25.680	1.2000	1.6800	27.0300	.0000

.....

THE 9.0449 FCIR 7.7600 ICOR 4.1000 TWIND=22.6U PAMB= 735.0MM HG
ASPLI MATIC=17.7000 Tilt Angle= 0.0 VEL=2.260M/S DIST BETWEEN PLATES=25.4000 MM
-1549792 14.2300000 011.2800490 12.3385748
ALUC= 30.0 MP LUM=010 RESFAC= 0.03 HE= 0.475E+05 PM= .709
ORZ= 11.000 HAZ= 0.37E+04 UNZ= 2.07E+08 HAX= .1479E+08 NUL=2.6979 NULCM=2.6882
-PIZL FRIQUE SHIFZ 3.0000

SECTIONAL SCANS

UPT (mm)	TLUC	SHIF	TEMP (C)	THETA
0.000	0.000	0.000	27.9400	1.0000
1.376	0.500	0.315	29.2276	0.786
2.752	1.000	0.630	30.6520	0.796
4.128	1.500	0.945	32.1996	0.794
5.504	2.000	1.260	33.8500	0.821
6.880	2.500	1.575	35.5901	0.976
8.256	3.000	1.890	37.4036	0.857
9.632	3.500	2.205	39.2756	0.930
11.008	4.000	2.520	41.1909	0.529
12.384	4.500	2.835	43.1361	0.195
13.760	5.000	3.150	45.1004	0.121
15.136	5.500	3.465	47.0847	0.042
16.512	6.000	3.780	49.0820	0.025
17.888	6.500	4.095	51.0874	0.073
19.264	7.000	4.410	53.1001	0.531
20.640	7.500	4.725	55.1241	0.163
22.016	8.000	5.040	57.1634	0.105
23.392	8.500	5.355	59.2139	0.077
24.768	9.000	5.670	61.2809	0.259
26.144	9.500	5.985	63.3587	0.124
27.520	10.000	6.300	65.4501	0.600

TANK=22.50 PANN= 735.0MM HG
 DIST BETWEEN PLATES=25.4000 MM
 TANK=21.70 VLL=2.260M/S
 13.232700
 PMS .709
 NULC=2.0851 NULC=2.9350
 NULC=2.0851 NULC=2.9350

SECTIONAL SCANS

DEPTH (mm)	TLUC	SHIF	TLUP (U)	TLUL
0.000	0.000	0.000	0.000	0.000
1.250	0.000	0.000	0.000	0.000
2.500	0.000	0.000	0.000	0.000
3.750	0.000	0.000	0.000	0.000
5.000	0.000	0.000	0.000	0.000
6.250	0.000	0.000	0.000	0.000
7.500	0.000	0.000	0.000	0.000
8.750	0.000	0.000	0.000	0.000
10.000	0.000	0.000	0.000	0.000
11.250	0.000	0.000	0.000	0.000
12.500	0.000	0.000	0.000	0.000
13.750	0.000	0.000	0.000	0.000
15.000	0.000	0.000	0.000	0.000
16.250	0.000	0.000	0.000	0.000
17.500	0.000	0.000	0.000	0.000
18.750	0.000	0.000	0.000	0.000
20.000	0.000	0.000	0.000	0.000
21.250	0.000	0.000	0.000	0.000
22.500	0.000	0.000	0.000	0.000
23.750	0.000	0.000	0.000	0.000
25.000	0.000	0.000	0.000	0.000

.....

TIME=21.000 TOL=23.7000 TOL=24.0200 TAMB=21.70 PAMB=735.0MM HG
 ASPICI=11.7000 TILT=0.0000 VCL=2.250M/S .DIST BETWEEN PLATES=25.4000 MM
 11.03499734 -17.7971631
 11.03499734 -17.7971631
 ALUM=11.03499734 MON-DIST=0.433 REA=6479E+05 PR= .709
 INCL=11.03499734 HAL=0.002E+04 GRA=5.31E+08 RAA=.3778E+08 NUL=2.4900 NULCM=2.9528
 INITIAL FRICTION SHIP=3.0000

SECTIONAL SCALING

YLOC	YLOC	SHIF	TEMP	THEIA
0.0000	0.0010	0.0000	29.9900	1.0000
1.071	.3475	0.1054	28.1054	.9079
2.042	.7150	0.2108	26.2108	.7900
3.013	1.0825	0.3162	24.3162	.6722
4.010	1.4500	0.4216	22.4216	.5604
5.000	1.8175	0.5270	20.5270	.4546
6.000	2.1850	0.6324	18.6324	.3548
7.026	2.5525	0.7378	16.7378	.2610
8.000	2.9200	0.8432	14.8432	.1742
9.000	3.2875	0.9486	12.9486	.0944
10.000	3.6550	1.0540	11.0540	.0216
11.000	4.0225	1.1594	9.1594	.0000
12.000	4.3900	1.2648	7.2648	.0000
13.000	4.7575	1.3702	5.3702	.0000
14.000	5.1250	1.4756	3.4756	.0000
15.000	5.4925	1.5810	1.5810	.0000
16.000	5.8600	1.6864	0.0000	.0000
17.000	6.2275	1.7918	0.0000	.0000
18.000	6.5950	1.8972	0.0000	.0000
19.000	6.9625	2.0026	0.0000	.0000
20.000	7.3300	2.1080	0.0000	.0000
21.000	7.6975	2.2134	0.0000	.0000
22.000	8.0650	2.3188	0.0000	.0000
23.000	8.4325	2.4242	0.0000	.0000
24.000	8.8000	2.5296	0.0000	.0000
25.000	9.1675	2.6350	0.0000	.0000
26.000	9.5350	2.7404	0.0000	.0000

.....

TRINU=2.50 PAMB= 735.0MM HG
 DIST BETWEEN PLATES=25.4000, MM
 TAMB=21.70
 VEL=2.240M/S
 10.855808

KE= .6479E+05 PRM 2709
 HMA= .4458E+08 NULC=2.6884 NULCM=2.1107

ICS=24.0201
 ILLI MULC= 0.6
 -17.4455010

ICS=23.000
 ILLI MULC= 0.6
 -17.4455010

TON=0.011111111111111111
 WAL= 0.000000000000000000
 TOTAL FRINGE STRESS 3.5079

SECTIONAL SUMMATED

DIST (MM)	TLOC	SHIFT	TEMP (C)	THEIA
0.000	0.0000	0.0000	29.0000	1.0000
1.270	0.0000	.4076	29.0000	.8002
2.540	0.0000	.8152	28.5035	.7592
3.810	0.0000	1.2228	27.9351	.6754
5.080	0.0000	1.6305	27.3260	.5594
6.350	0.0000	2.0380	27.1758	.5438
7.620	0.0000	2.4456	26.9970	.5012
8.890	0.0000	2.8532	26.7607	.4693
10.160	0.0000	3.2608	26.6234	.4458
11.430	0.0000	3.6684	26.5219	.4274
12.700	0.0000	4.0760	26.4490	.4134
13.970	0.0000	4.4836	26.3934	.4034
15.240	0.0000	4.8912	26.3501	.3964
16.510	0.0000	5.2988	26.3100	.3924
17.780	0.0000	5.7064	26.2709	.3894
19.050	0.0000	6.1140	26.2309	.3864
20.320	0.0000	6.5216	26.1909	.3834
21.590	0.0000	6.9292	26.1509	.3804
22.860	0.0000	7.3368	26.1109	.3774
24.130	0.0000	7.7444	26.0709	.3744
25.400	0.0000	8.1520	26.0309	.3714

INE=2.0000 INI=73.7000 - ILO=24.0200 TAMD=21.70 TIND=22.50 PAMB= 735.0MM HG
 ASPLI=11.1000 ILL=0.00 VLL=2.260M/S DIST BETWEEN PLATES=25.4000 MM
 2917000 29175000 -JL.5049500
 ALUM=23.00 MP. 400=016 DISTANCE= 97M ME= .6479E+05 MH= .709
 SALS=11.0000 MALS= .012104 UNKE= .01+0E+00 MAX= .4352E+08 NUL=3.6722 NULC=4.6533
 TOTAL PHASE SHIFTS=30079

SECTIONAL SKEW (1/4)

0951 (1/4)	YCC	SWIFT	PLAT	PLATE
0.000	0.0000	0.0000	2.0000	1.0000
1.070	0.500	5.704	2.0000	2.0007
2.050	1.000	9.599	2.0000	3.0015
3.016	1.500	12.790	2.0000	4.0031
4.000	2.000	15.400	2.0000	5.0053
5.000	2.500	17.600	2.0000	6.0080
6.000	3.000	19.400	2.0000	7.0110
7.000	3.500	20.800	2.0000	8.0140
8.000	4.000	21.900	2.0000	9.0170
9.000	4.500	22.700	2.0000	10.0200
10.000	5.000	23.300	2.0000	11.0230
11.000	5.500	23.700	2.0000	12.0260
12.000	6.000	24.000	2.0000	13.0290
13.000	6.500	24.200	2.0000	14.0320
14.000	7.000	24.300	2.0000	15.0350
15.000	7.500	24.400	2.0000	16.0380
16.000	8.000	24.500	2.0000	17.0410
17.000	8.500	24.600	2.0000	18.0440
18.000	9.000	24.700	2.0000	19.0470
19.000	9.500	24.800	2.0000	20.0500
20.000	10.000	24.900	2.0000	21.0530
21.000	10.500	25.000	2.0000	22.0560
22.000	11.000	25.100	2.0000	23.0590
23.000	11.500	25.200	2.0000	24.0620
24.000	12.000	25.300	2.0000	25.0650
25.000	12.500	25.400	2.0000	26.0680
26.000	13.000	25.500	2.0000	27.0710
27.000	13.500	25.600	2.0000	28.0740
28.000	14.000	25.700	2.0000	29.0770
29.000	14.500	25.800	2.0000	30.0800
30.000	15.000	25.900	2.0000	31.0830
31.000	15.500	26.000	2.0000	32.0860
32.000	16.000	26.100	2.0000	33.0890
33.000	16.500	26.200	2.0000	34.0920
34.000	17.000	26.300	2.0000	35.0950
35.000	17.500	26.400	2.0000	36.0980
36.000	18.000	26.500	2.0000	37.1010
37.000	18.500	26.600	2.0000	38.1040
38.000	19.000	26.700	2.0000	39.1070
39.000	19.500	26.800	2.0000	40.1100
40.000	20.000	26.900	2.0000	41.1130
41.000	20.500	27.000	2.0000	42.1160
42.000	21.000	27.100	2.0000	43.1190
43.000	21.500	27.200	2.0000	44.1220
44.000	22.000	27.300	2.0000	45.1250
45.000	22.500	27.400	2.0000	46.1280
46.000	23.000	27.500	2.0000	47.1310
47.000	23.500	27.600	2.0000	48.1340
48.000	24.000	27.700	2.0000	49.1370
49.000	24.500	27.800	2.0000	50.1400
50.000	25.000	27.900	2.0000	51.1430
51.000	25.500	28.000	2.0000	52.1460
52.000	26.000	28.100	2.0000	53.1490
53.000	26.500	28.200	2.0000	54.1520
54.000	27.000	28.300	2.0000	55.1550
55.000	27.500	28.400	2.0000	56.1580
56.000	28.000	28.500	2.0000	57.1610
57.000	28.500	28.600	2.0000	58.1640
58.000	29.000	28.700	2.0000	59.1670
59.000	29.500	28.800	2.0000	60.1700
60.000	30.000	28.900	2.0000	61.1730
61.000	30.500	29.000	2.0000	62.1760
62.000	31.000	29.100	2.0000	63.1790
63.000	31.500	29.200	2.0000	64.1820
64.000	32.000	29.300	2.0000	65.1850
65.000	32.500	29.400	2.0000	66.1880
66.000	33.000	29.500	2.0000	67.1910
67.000	33.500	29.600	2.0000	68.1940
68.000	34.000	29.700	2.0000	69.1970
69.000	34.500	29.800	2.0000	70.2000
70.000	35.000	29.900	2.0000	71.2030
71.000	35.500	30.000	2.0000	72.2060
72.000	36.000	30.100	2.0000	73.2090
73.000	36.500	30.200	2.0000	74.2120
74.000	37.000	30.300	2.0000	75.2150
75.000	37.500	30.400	2.0000	76.2180
76.000	38.000	30.500	2.0000	77.2210
77.000	38.500	30.600	2.0000	78.2240
78.000	39.000	30.700	2.0000	79.2270
79.000	39.500	30.800	2.0000	80.2300
80.000	40.000	30.900	2.0000	81.2330
81.000	40.500	31.000	2.0000	82.2360
82.000	41.000	31.100	2.0000	83.2390
83.000	41.500	31.200	2.0000	84.2420
84.000	42.000	31.300	2.0000	85.2450
85.000	42.500	31.400	2.0000	86.2480
86.000	43.000	31.500	2.0000	87.2510
87.000	43.500	31.600	2.0000	88.2540
88.000	44.000	31.700	2.0000	89.2570
89.000	44.500	31.800	2.0000	90.2600
90.000	45.000	31.900	2.0000	91.2630
91.000	45.500	32.000	2.0000	92.2660
92.000	46.000	32.100	2.0000	93.2690
93.000	46.500	32.200	2.0000	94.2720
94.000	47.000	32.300	2.0000	95.2750
95.000	47.500	32.400	2.0000	96.2780
96.000	48.000	32.500	2.0000	97.2810
97.000	48.500	32.600	2.0000	98.2840
98.000	49.000	32.700	2.0000	99.2870
99.000	49.500	32.800	2.0000	100.2900
100.000	50.000	32.900	2.0000	101.2930

INSPY=001
 ASPFL=11.700
 11.700
 16.000
 11.1854411
 TWINU=22.50
 DIST BETWEEN PLATES=25.4000 MM
 PAMB= 735.0MM HG
 JAMB=21.70
 VEL=C.260M/S
 11.1854411
 ALUCP=0000000
 ONCE=11.00000
 TOTAL PHASE SHIFTS=3.00000
 NON-OJM DISTANCE=.993
 MEZ=.6479E+05
 PR=.709
 ORCA=.0027E+08
 MAX=.4555E+08
 NUL=3.3113
 NULCW=1.7968

SECTIONAL SCANS#5

DIST (UM)	YLOC	SHIFT	ICMP	TNETA
10.000	0.0000	0.0000	19.0000	1.0000
10.100	0.0000	0.0000	19.0000	1.0000
10.200	0.0000	0.0000	19.0000	1.0000
10.300	0.0000	0.0000	19.0000	1.0000
10.400	0.0000	0.0000	19.0000	1.0000
10.500	0.0000	0.0000	19.0000	1.0000
10.600	0.0000	0.0000	19.0000	1.0000
10.700	0.0000	0.0000	19.0000	1.0000
10.800	0.0000	0.0000	19.0000	1.0000
10.900	0.0000	0.0000	19.0000	1.0000
11.000	0.0000	0.0000	19.0000	1.0000
11.100	0.0000	0.0000	19.0000	1.0000
11.200	0.0000	0.0000	19.0000	1.0000
11.300	0.0000	0.0000	19.0000	1.0000
11.400	0.0000	0.0000	19.0000	1.0000
11.500	0.0000	0.0000	19.0000	1.0000
11.600	0.0000	0.0000	19.0000	1.0000
11.700	0.0000	0.0000	19.0000	1.0000
11.800	0.0000	0.0000	19.0000	1.0000
11.900	0.0000	0.0000	19.0000	1.0000
12.000	0.0000	0.0000	19.0000	1.0000
12.100	0.0000	0.0000	19.0000	1.0000
12.200	0.0000	0.0000	19.0000	1.0000
12.300	0.0000	0.0000	19.0000	1.0000
12.400	0.0000	0.0000	19.0000	1.0000
12.500	0.0000	0.0000	19.0000	1.0000
12.600	0.0000	0.0000	19.0000	1.0000
12.700	0.0000	0.0000	19.0000	1.0000
12.800	0.0000	0.0000	19.0000	1.0000
12.900	0.0000	0.0000	19.0000	1.0000
13.000	0.0000	0.0000	19.0000	1.0000
13.100	0.0000	0.0000	19.0000	1.0000
13.200	0.0000	0.0000	19.0000	1.0000
13.300	0.0000	0.0000	19.0000	1.0000
13.400	0.0000	0.0000	19.0000	1.0000
13.500	0.0000	0.0000	19.0000	1.0000
13.600	0.0000	0.0000	19.0000	1.0000
13.700	0.0000	0.0000	19.0000	1.0000
13.800	0.0000	0.0000	19.0000	1.0000
13.900	0.0000	0.0000	19.0000	1.0000
14.000	0.0000	0.0000	19.0000	1.0000
14.100	0.0000	0.0000	19.0000	1.0000
14.200	0.0000	0.0000	19.0000	1.0000
14.300	0.0000	0.0000	19.0000	1.0000
14.400	0.0000	0.0000	19.0000	1.0000
14.500	0.0000	0.0000	19.0000	1.0000
14.600	0.0000	0.0000	19.0000	1.0000
14.700	0.0000	0.0000	19.0000	1.0000
14.800	0.0000	0.0000	19.0000	1.0000
14.900	0.0000	0.0000	19.0000	1.0000
15.000	0.0000	0.0000	19.0000	1.0000
15.100	0.0000	0.0000	19.0000	1.0000
15.200	0.0000	0.0000	19.0000	1.0000
15.300	0.0000	0.0000	19.0000	1.0000
15.400	0.0000	0.0000	19.0000	1.0000
15.500	0.0000	0.0000	19.0000	1.0000
15.600	0.0000	0.0000	19.0000	1.0000
15.700	0.0000	0.0000	19.0000	1.0000
15.800	0.0000	0.0000	19.0000	1.0000
15.900	0.0000	0.0000	19.0000	1.0000
16.000	0.0000	0.0000	19.0000	1.0000
16.100	0.0000	0.0000	19.0000	1.0000
16.200	0.0000	0.0000	19.0000	1.0000
16.300	0.0000	0.0000	19.0000	1.0000
16.400	0.0000	0.0000	19.0000	1.0000
16.500	0.0000	0.0000	19.0000	1.0000
16.600	0.0000	0.0000	19.0000	1.0000
16.700	0.0000	0.0000	19.0000	1.0000
16.800	0.0000	0.0000	19.0000	1.0000
16.900	0.0000	0.0000	19.0000	1.0000
17.000	0.0000	0.0000	19.0000	1.0000
17.100	0.0000	0.0000	19.0000	1.0000
17.200	0.0000	0.0000	19.0000	1.0000
17.300	0.0000	0.0000	19.0000	1.0000
17.400	0.0000	0.0000	19.0000	1.0000
17.500	0.0000	0.0000	19.0000	1.0000
17.600	0.0000	0.0000	19.0000	1.0000
17.700	0.0000	0.0000	19.0000	1.0000
17.800	0.0000	0.0000	19.0000	1.0000
17.900	0.0000	0.0000	19.0000	1.0000
18.000	0.0000	0.0000	19.0000	1.0000
18.100	0.0000	0.0000	19.0000	1.0000
18.200	0.0000	0.0000	19.0000	1.0000
18.300	0.0000	0.0000	19.0000	1.0000
18.400	0.0000	0.0000	19.0000	1.0000
18.500	0.0000	0.0000	19.0000	1.0000
18.600	0.0000	0.0000	19.0000	1.0000
18.700	0.0000	0.0000	19.0000	1.0000
18.800	0.0000	0.0000	19.0000	1.0000
18.900	0.0000	0.0000	19.0000	1.0000
19.000	0.0000	0.0000	19.0000	1.0000

PLOT SUMMARY
MAXIMUM X POSITION REQUESTED : 6.200
MINIMUM X POSITION REQUESTED : 6.200
MAXIMUM Y POSITION REQUESTED : 6.200
MINIMUM Y POSITION REQUESTED : 6.200
3 INVALID PARAMETERS
ESTIMATED TOTAL PLOTTING TIME 1 MIN. IN TRUNCATION POINT
OUTPUT IS PLOT NUMBER 031529.052

PLOT SUMMARY
MAXIMUM X POSITION REQUESTED : 6.629
MINIMUM X POSITION REQUESTED : 6.167
MAXIMUM Y POSITION REQUESTED : 6.250
MINIMUM Y POSITION REQUESTED : 6.662
ESTIMATED TOTAL PLOTTING TIME 5 MIN.
OUTPUT IS PLOT NUMBER 031529.054

PLOT SUMMARY
MAXIMUM X POSITION REQUESTED : 6.443
MINIMUM X POSITION REQUESTED : 6.167
MAXIMUM Y POSITION REQUESTED : 6.800
MINIMUM Y POSITION REQUESTED : 6.662
ESTIMATED TOTAL PLOTTING TIME 8 MIN.
OUTPUT IS PLOT NUMBER 031529.050

SUSSELT # HOT 3.11
SUSSELT # COLD 2.74

APPENDIX C
DATA REDUCTION

After the vertical temperature profiles between the horizontal hot and cold plates within the enclosure were plotted, the temperature gradients at each boundary were calculated. From these temperature gradients the local Nusselt numbers, which represent the local heat transfer, were found as follows:

$$Nu_L = \frac{hL}{K_m} \quad (C.1)$$

where h = local heat transfer coefficient

L = mean plate spacing between the hot and cold plate.

K_m = thermal conductivity of air evaluated at the bulk temperature of the enclosure.

The heat transfer by conduction at the wall is given by

$$q' \Big|_W = -K_W \frac{\partial T}{\partial Y} \Big|_W \quad (C.2)$$

where q' = local heat flux

K_W = thermal conductivity of the air evaluated at the wall

The local heat transfer by convection is given by Newton as

$$q' = h(T_h - T_c) \quad (C.3)$$

By equating Eqs. C.2 and C.3, the following equation will result:

$$-K_w \left. \frac{\partial T}{\partial Y} \right|_w = h(T_h - T_c) \quad (C.4)$$

Multiplying both sides by L and dividing by K_m , we will have

$$Nu_L = \frac{hL}{K_m} = - \frac{K_w}{K_m} \frac{L}{(T_h - T_c)} \left. \frac{\partial T}{\partial Y} \right|_w \quad (C.5)$$

The temperature within the enclosure can be represented by a non-dimensional form as

$$\theta = \frac{T - T_{CB}}{T_h - T_{CB}} \quad (C.6)$$

Thus, the temperature gradient at the wall can be expressed as

$$\left. \frac{\partial T}{\partial Y} \right|_w = (T_h - T_c) \left. \frac{\partial \theta}{\partial Y} \right|_w \quad (C.7)$$

Therefore, Eq. C.5 becomes

$$Nu_L = - \frac{K_w}{K_m} \left. \frac{\partial \theta}{\partial Y} \right|_w$$

The average Nusselt number can be calculated by mathematical integration of the local Nusselt number distribution over the surface as follows:

$$\overline{Nu}_L = \frac{1}{H} \int_0^H Nu_L dx \quad (C.8)$$

where H is enclosure length. The numerical integration technique by Simpson's rule, which is based on the use of parabolic arcs instead of straight lines, was employed for finding the average Nusselt numbers.

The average Nusselt numbers were also calculated near the bottom of the cold surface which provided information for the correlation of the heat loss through the top surface due to the exterior forced convection.

A typical sample calculation is given in Appendix D.

APPENDIX D

SAMPLE CALCULATIONS

A typical sample calculation is presented below. It was made from the following recorded data for the first section of the test model with respect to the leading edge at which forced convection occurred.

Average temperature of hot plate = 29.90°C

Average temperature of bottom cold plate = 23.98°C

Average temperature of top surface of cold plate = 23.67°C

Ambient temperature = 21.90°C

Wind tunnel temperature = 22.70°C

Ambient pressure = 735 mm Hg

Aspect ratio = 17.70/1.00 = 17.70

Average wind tunnel velocity = 2.26 m/s

Average distance between plates = 25.40 mm

Average bulk temperature within the enclosure = 26.94°C

D.1 INTERFEROGRAM ANALYSIS

The minimum fringe shift is zero at the hot plate and maximum at the cold plate which can be calculated from

$$F_{SH}(X, Y) = 75.69 (P_{amb.}) \left(\frac{1}{T_{CB}} - \frac{1}{T_H} \right)$$

$$F_{SH}(3.4 \text{ mm}, 25.40 \text{ mm}) = 75.69 \cdot (735.0) \left(\frac{1}{297.14} - \frac{1}{303.06} \right)$$

$$F_{SH}(3.4 \text{ mm}, 25.40 \text{ mm}) = 3.657 \text{ mm}$$

2. Density is given by

$$\rho = \frac{P}{RT}$$

$$\rho = \frac{(735.0) \left(\frac{101325}{760} \right)}{(287.097) (300.10)}$$

$$\rho = 1.137 \text{ kg/m}^3$$

3. Grashof number is given by

$$Gr = \frac{g\beta\Delta T L^3 \rho^2}{\mu^2}$$

$$= \frac{(9.8016) (1/300.10) (5.92) (0.0254)^3 (1.137)^2}{(1.847 \times 10^{-5})^2}$$

$$Gr = 12020$$

4. Specific heat at constant pressure

$$C_p = B_1 - B_2 T_M + B_3 T_M^2 + B_4 T_M^3$$

$$\text{where } B_1 = 1.02432748$$

$$B_2 = 1.39785579 \times 10^{-4}$$

$$B_3 = 2.06057349 \times 10^{-7}$$

$$B_4 = 2.00205 \times 10^{-10}$$

$$T_m = 300.10^\circ\text{K}$$

$$\text{Thus, } C_p = 1.001 \text{ kJ/kg}^\circ\text{K}$$

Therefore, the maximum fringe shift is 3.657 mm. Now, for example, the temperature at the midsection of the enclosure, where $X = 3.40$ mm and $Y = 12.70$ mm with a fringe shift of 2.125 mm (the procedure was discussed in Appendix B) can be calculated as follows:

$$T(X, Y) = \frac{3GWT_H P}{3GWP + 2F(X, Y) \lambda R_{TH}}$$

$$\text{or } T(X, Y) = \frac{T_H}{\frac{2F(X, Y) \lambda R_{TH}}{3GWP} + 1}$$

$$T(3.4\text{mm}, 12.70\text{mm}) = \frac{303.06}{\frac{2(2.125)(6.328 \times 10^{-7})(287.097)(303.06)}{2(0.4572)(0.1504 \times 10^{-3})(735.0)\left(\frac{101325}{760}\right)} + 1}$$

$$T(3.4\text{mm}, 12.70\text{mm}) = 299.592^\circ\text{K}$$

or

$$T(3.4\text{mm}, 12.70\text{mm}) = 26.432^\circ\text{C}$$

D.2 DATA REDUCTION

1. Viscosity is given by:

$$\mu = \frac{C_1 T_m^{1.5}}{C_2 + T_m}$$

where $C_1 = 1.4582 \times 10^{-6}$ and $C_2 = 110.39$

$$\text{Thus } \mu = \frac{1.4582 \times 10^{-6} (300.10)^{1.5}}{110.39 + 300.10}$$

$$\mu = 1.847 \times 10^{-5} \text{ Kg/ms}$$

5. Thermal conductivity is given by

$$K_m = 7.4960 \times 10^{-5} T_m + .024204$$

$$= 2.622 \times 10^{-2} \text{ W/m}^\circ\text{C}$$

6. Prandtl number is given by

$$Pr = \frac{\mu C_p}{K}$$

$$= \frac{(1.847 \times 10^{-5})(1.001 \times 10^3)}{2.622 \times 10^{-2}}$$

$$Pr = 0.705$$

7. Nusselt number is given by

$$Nu_L = - \frac{K_w}{K_m} \frac{\partial \theta}{\partial Y} \Big|_w$$

The average temperature profile was best described by a polynomial equation of the form found from a best fit least squares regression technique

$$T = A + BY + CY^2 + DY^3 + EY^4$$

The average axial temperature profile was found and the slope of the profile at the hot and cold plates were determined. From the slopes, the Nusselt numbers at both plates were calculated. The Simpson's Rule numerical integration technique was applied to find the average Nusselt numbers. The average Nusselt numbers are as follows:

At the hot plate

$$\overline{Nu}_L = 3.11$$

At the cold plate

$$\overline{Nu}_L = 2.74$$

8. Reynolds number is given by

$$Re_{L_c} = \frac{\rho U_{\infty} L_c}{\mu}$$

where L_c is the characteristic length and ρ and μ are evaluated at the wind tunnel temperature

$$Re_L = 6.29 \times 10^4$$

APPENDIX E
EXPERIMENTAL ERRORS

In experimental studies it is desirable to establish uncertainty levels associated with parameters affecting the final results. These uncertainty levels or errors are often due to equipment, evaluation of physical properties of medium and method of analysis.

In the present investigation, equipment errors were furnished by manufacturers' specifications which are tabulated in Table E.1.

The medium was air at atmospheric pressure at temperatures varying from 0°C to 95°C. The air properties were evaluated from the correlation equations given in Appendix A. The maximum deviation between the values given in properties of air tables from the correlations was about 0.1%.

The errors arising from use of the long path Mach-Zehnder interferometer which provided temperature fields and calculation of the Nusselt numbers were attributed to two major sources:

1. interferometer and alignment, and
2. interferogram analysis.

The uncertainty levels associated with the interferometer

are due to optical glass imperfection, effective optical path length through the test model, misalignment of the model and imperfection of the heated section. Similarly, the errors associated with the analysis of interferograms often arise from measurement of fringe location, establishing the boundaries and misalignment of the output optics. An account of each of the above factors is discussed below:

The long path Mach-Zehnder interferometer utilized in this study had negligible optical imperfections. The optical components were highly polished (to within one tenth of a wavelength) with minute irregularities which could not appreciably affect the results. This was verified by taking a finite fringe field interferogram with no temperature differential within the enclosure, which resulted in straight and parallel lines.

The errors arising from the effect of optical path length through the model were compensated for by the initial adjustment of the optical system. Also, the effective optical path length in the enclosure due to the outside thermal boundary layer on the optical glass was not significant. Randall [2] investigated this by assuming natural convection over a vertical flat plate in an infinite medium. The external boundary layer thickness was estimated for a typical experimental condition by

numerical integration and was found to have a maximum error of 1%, which affected only slightly the computed result of the Nusselt number. The same order of error can also be assumed for the change in the index of refraction.

2 A misalignment of the model from the direction of the light beam or imperfection of the horizontal boundaries causes reflection of light beam passing through the enclosure. This was estimated to be within 0.5° from the light beam which resulted in an error of 1% [113].

Error was introduced in measuring the distance from hot plate boundary to a particular fringe and spacing between fringes. These distances were first measured by an automatic interferogram scanning device which required perfectly defined boundaries. Thus, a travelling microscope was used with an accuracy of 0.025 mm.

The final results of the average Nusselt number correlations gave an average error of 2.4%. The computer results are included.

TABLE E.1 Instrument Specifications

Source of Error	Quantity Measured [units]	Error
Thermocouple Indicator (Digitrend 220)	Temperature [°C]	+ 0.4°C
Thermocouple (junction and leads)	Temperature [°C]	0.8°C below 90°C
Barometer	Pressure [kPa]	1.0% Pressure
Travelling Microscope	Distance [mm]	0.025 mm
Scanivalve and Barocel Pressure Transducer	Pressure [kPa]	0.5% Pressure

REFERENCES

1. Bird, R.B., Stewart, W.E. and Lightfoot, E.N.; "Transport Phenomena", John Wiley & Sons, New York; (1960).
2. Randall, K.R.J., "An Interferometric Study of Natural Convection Heat Transfer in Flat-Plate and Vee-Corrugated Enclosure", Ph.D. Dissertation, The University of Wisconsin, (1978).
3. Thompson, J.J., Proc. Glasgow Phil. Soc., 13, 464, (1882).
4. Bernard, H., "Les tourbillons cellulaires dans une nappe liquide transportant de la chaleur par convection en regime permanent", Ann. Chem. Phys., 23, 62, (1901).
5. Lord Rayleigh, "On Convective Currents in a Horizontal Layer of Fluid When the Higher Temperature is on the Underside", Phil. Mag., 32, 529, (1916).
6. Farhadih, R., "Interferometric Study of the Two-Dimensional Benard Convection Cells (Rolls) and Their Effects on Formation of Ice", Ph.D. Thesis, Northwestern University, (1974).
7. Jeffrey, S.H., "The Stability of a Layer of Fluid Heated Below", Phil. Mag., 2, 833, (1926).
8. Jeffrey, S.H., "Some Cases of Instability in Fluid Motion", Proc. Roy. Soc. (London), A, 118, (1928).
9. Pellew, A. and Southwell, R.V., "On Maintained Convective Motion in a Fluid Heated From Below", Proc. Roy. Soc. (London), A, 176, 312, (1940).
10. Currie, I.G., "The Effect of Heating Rate on the Stability of Stationary Fluids", J. Fluid Mech., Vol. 29, Pt 2, (Aug.1967) P337.
11. Pearson, J.R.A., "On Convection Cells Induced by Surface Tension", J. Fluid Mech., 4, 489, (1958).
12. Nield, D.A., "Surface Tension and Buoyancy Effects in Cellular Convection", J. Fluid Mech., 19, 341, (1964).

13. Malkus, W.V.R. and Veronis, G., "Finite Amplitude Cellular Convection", J. Fluid Mech., 4, 225, (1958).
14. Schuster, A., Lortz, D. and Busse, F.H., "On the Stability of Steady Finite Amplitude Convection", J. of Fluid Mech., 23, 129, (1967).
15. Busse, F.H., "On the Stability of Two-Dimensional Convection in a Layer Heated From Below", J. Math. and Phys., 46, 140, (1967a).
16. Chorin, A.J., "A Numerical Method for Solving Incompressible Viscous Flow Problems", J. Comp. Phys., 2, 12, (1967).
17. Schneck, P. and Vernois, G., "Comparison of Some Recent Experimental and Numerical Results in Benard Convection", Phys. Fluids, 10, 927, (1967).
18. Deardoff, J.W., "Examination of Numerically Calculated Heat Fluxes for Evidence of a Super Critical Transition", Phys. Fluids, 11, 1254, (1968).
19. Veronis, G., "Large-Amplitude Benard Convection", J. Fluid Mech., 26, 49, (1966).
20. Herring, J.R., "Investigation of Problems in Thermal Convection", J. of Atmos. Sci., 20, 325, (1963).
21. Samuels, M.R. and Churchill, S.W., "Stability of a Fluid in a Rectangular Region Heated From Below", A.I.Ch.E. J., 13, 77, (1967).
22. Sorokin, M.P., Inzh. Fiz. Zh., 4, No. 8, 107, (1961).
23. Schmidt, R.J. and Milverton, S.W., "On the Instability of a Fluid When Heated From Below", Proc. Roy. Soc. (London), A, 152, 594, (1935).
24. Schmidt, R.J. and Sanders, O.A., "On the Motion of a Fluid Heated From Below", Proc. Roy. Soc. (London), A, 165, 216, (1938).
25. Chandra, K., "Instability of Fluids Heated From Below", Proc. Roy. Soc. (London), A, 164, 23, (1938).

26. De Graaf, J.G.A. and Van der Held, E.F.M., "The Relation Between the Heat Transfer and the Convection Phenomenon in Enclosed Plane Air Layer", Appl. Sci. Res., 3, 393, (1952).
27. Van der Held, E.F.M., Warmtetechniek, 54, (1931).
28. Jacob, M., Trans. Amer. Soc. Mech. Engrs., 68, 189, (1946).
29. Mull, W. and Reiher, H., Beih. Z., Gesundheitstech.-Ing., Series 1, 28, (1930).
30. Schmidt, E. and Silveston, P.L., "Natural Convection in Horizontal Liquid Layers", American Inst. of Chemical Eng., Chem. Eng. Progress Symposium Series, No. 29, Vol. 55, (1959).
31. O'Toole, J.L. and Silveston, P.L., "Correlations of Convective Heat Transfer in Confined Horizontal Layers", Chemical Eng. Progr. Symp. Series, 57, 81, (1961).
32. Somerscales, E.F.C. and Dorpkin, D., "Experimental Investigation of the Temperature Distribution in a Horizontal Layer of Fluid Heated From Below", Int. J. of Heat Mass Transfer, 9, 1189, (1966).
33. Koschmieder, E.L., "On Convection on a Uniformly Heated Plane", Breit. z. Phys. d. Atoms., 39, 1, (1966).
34. Catton, L. and Edwards, D.K., "Effect of Side Walls on Natural Convection Between Horizontal Plates Heated From Below", J. Heat Transfer, ASME Trans., 89, 295, (1967).
35. Silveston, P.L., "Wärmedurchgang in Waagerechten Turbulent Flüssigkeitschichten", Forsch. Ing. Wes., 24, 29-32, 59-69, (1958).
36. Gille, J., "Interferometric Measurement of Temperature Gradient Reversal in a Layer of Convecting Air", J. Fluid Mech., 30, 371, (1967).
37. Farhadieh, R. and Tankin, R.S., "Interferometric Study of Two-Dimensional Benard Convection Cells", J. Fluid Mech., 66, 739, (1974).

38. Rossby, H.T., "A Study of Benard Convection With and Without Rotation", J. Fluid Mech., 36, 309, (1969).
39. Krishnamurti, R., "On the Transition to Turbulent Convection. Part 1. The Transition From Two- to Three-Dimensional Flow", J. Fluid Mech., 42, 295, (1970).
40. Busse, F.H. and Whitehead, J.A., "Instabilities of Convection Rolls in a High Prandtl Number Fluid", J. Fluid Mech., 47, 305, (1971).
41. Willis, G.E., Deardorff, J.W. and Somerville, R.C.J. "Roll-Diameter Dependence in Rayleigh Convection and Its Effect Upon the Heat Flux", J. Fluid Mech., 54, 351, (1972).
42. Tabor, H., "Radiation, Convection, and Conduction Coefficients in Solar Collectors", Bull. Res. Council of Israel, Vol. 6C, (1958).
43. Robinson and Powlitch, "The Thermal Insulation Valve of Airspace", Housing Research Paper #32, Housing and Home Finance Agency, Washington, D.C., (1954).
44. Globe, S. and Dropkin, D., "Natural Convection Heat Transfer in Liquids Confined by Two Horizontal Plates and Heated From Below", J. Heat Transfer, ASME Trans. 81, 24, (1959).
45. Dropkin, D. and Somerscale, E., "Heat Transfer by Natural Convection in Liquids Confined by Two Parallel Plates Which Are Inclined at Various Angles With Respect to the Horizontal", J. Heat Transfer, Trans. ASME, 87, 77, (1965).
46. McGregor, R.K. and Emery, A.F., "Free Convection Through Vertical Plane Layers - Moderate and High Prandtl Number Fluids", J. Heat Transfer, Trans. ASME, 91, 391, (1969).
47. Buchberg, H., Catton, I. and Edwards, D.K., "Natural Convection in Enclosed Spaces: A Review of Application to Solar Energy Collection", ASME Paper 74-WA/HT-12, (1974).
48. Elsherbiñy, S.M., "Heat Transfer by Natural Convection Across Vertical and Inclined Air Layers", Ph.D. Dissertation, The University of Waterloo, (1980).

49. Arnold, J.N., Edwards, D.K. and Catton, I., "Effect of Tilt and Horizontal Aspect Ratio on Natural Convection in a Rectangular Honeycomb", Journal of Heat Transfer, Trans. ASME, Series C, Vol. 99, 120-122, (Feb. 1977).
50. Buchberg, H., Lalude, O.A. and Edwards, D.K., "Performance Characteristics of Rectangular Honeycomb Solar-Thermal Converters", Solar Energy, 13, 193-224, (1971).
51. Cane, R.L.D., Hollands, K.G.T., Raithby, G.D. and Unny, T.E., "Free Convection Heat Transfer Across Inclined Honeycomb Panels", Journal of Heat Transfer, Trans. ASME, Series C, Vol. 99, 86-91, (1977).
52. Edwards, D.K., Arnold, J.N. and Catton, I., "End-Clearance Effects on Rectangular-Honeycomb Solar Collectors", Solar Energy, 18, 253-257, (1976).
53. Hollands, K.G.T., "Dimensional Relations for Free Convective Heat Transfer in Flat-Plate Collectors", Proceedings of the 1978 Annual Meeting of American Section of the ISES, Denver, Col., 207-213, (1978).
54. Hollands, K.G.T., "Honeycomb Devices in Flat-Plate Solar Collectors", Solar Energy, Vol. 18, No. 3, 159-164, (July-September 1965).
55. Hollands, K.G.T., "Natural Convection in Horizontal Thin-Walled Honeycomb Panels", Journal of Heat Transfer, Trans. ASME, Series C, Vol. 95, 439-444, (1973).
56. Hollands, K.G.T., "Studies on Methods of Reducing Heat Losses from Flat-Plate Solar Collectors", Annual Progress Report, ERDA, (1975).
57. Hollands, K.G.T., Raithby, G.D. and Unny, T.E., "Methods for Reducing Heat Losses from Flat-Plate Solar Collectors", Phase II, Final Report ERDA, (1978).
58. Kay, H.K. and Charters, W.W.S., "Convective Effects in Slat Collectors", Sun Mankind's Future Source of Energy, Proceedings of the ISES Congress, New Delhi, India, Vol. II, Pergamon Press, 965-970, (1978).

59. McMurrin, J.C., Djordjevic, N.A. and Buchberg, H., "Performance Measurements of a Cylindrical Glass Honeycomb Solar Collector Compared With Predictions", Journal of Heat Transfer, Trans. ASME, Series C, Vol. 99, 169-173, (1977).
60. Meyer, B.A., El-Wakil, M.M. and Mitchell, J.W., "An Interferometric Investigation of Heat Transfer in Honeycomb Solar Collector Cells", Sun Mankind's Future Source of Energy, Proceedings of the ISES Congress, New Delhi, India, 956-959, (1978).
61. Meyer, B.A., Mitchell, J.W. and El-Wakil, M.M., "Natural Convection Heat Transfer in Moderate Aspect Ratio Enclosures", Journal of Heat Transfer, Trans. ASME, 101, 655-659, (1979).
62. Sayigh, A.A.M., "A Comparison Among Various Flat-Plate Collectors With Honeycomb Structures", Sun Mankind's Future Source of Energy, Proceedings of the ISES Congress, New Delhi, India, Vol. II, 924-929, (1978).
63. Smart, P.R., Hollands, K.G.T. and Raithby, G.D., "Free Convection Heat Transfer Across Rectangular-Celled Diathermanous Honeycombs", Journal of Heat Transfer, 102, 75-80, (1980).
64. Watt, P.W., Edwards, D.K. and Arnold, J.N., "Effect of Tilt and Lateral Clearance on Natural Convection in Sinusoidal Honeycomb", Proceedings of Annual Meeting of American Section of the ISES, 202-205, (1978).
65. Wu, P.S. and Edwards, D.K., "Effect of Combined Tilt and Clearance Upon Natural Convection in High L/D Rectangular Honeycomb", Solar Energy, 25, 471-473, (1980).
66. Chinnappa, J.C.V., "Free Convection in Air Between a 60° Vee-Corrugated Plate and a Flat Plate", Int. J. Heat Transfer, 13, 117, (1970).
67. Elsharbiny, S.M., Hollands, K.G.T. and Raithby, G.D., "Free Convection Across Inclined Air Layers With One Surface Vee-Corrugated", J. Heat Transfer, Trans. ASME, 100, 410, (1978).

68. Raithby, G.D. and Hollands, K.G.T., "A General Method of Obtaining Approximate Solutions to Laminar and Turbulent Free Convection Problems", Advances in Heat Transfer, Vol. 11, Academic Press, (1974).
69. Raithby, G.D. and Hollands, K.G.T., "Laminar and Turbulent Heat Transfer by Natural Convection", Int. J. Heat Mass Transfer, 17, 1620, (1974).
70. Randall, K.R., Mitchell, J.W. and El-Wakil, M., "Natural Convection Characteristics of Flat Plate Collectors", Heat Transfer in Solar Energy Systems - The Winter Annual Meeting of the ASME, Atlanta, Georgia, November 27-December 2, (1977).
71. Brooks, R.G. and Probert, S.D., "Heat Transfer Between Parallel Walls: An Interferometric Investigation", J. of Mech. Eng. Science, 14, No. 2, (1972).
72. Hart, J.E., "Stability of the Flow in a Differentially Heated Inclined Box", J. Fluid Mech., 47, 547, (1971).
73. Clever, R.M., "Finite Amplitude Longitudinal Convection Rolls in an Inclined Layer", J. Heat Transfer, Trans. ASME, 95, 407, (1973).
74. Arnold, J.N., Catton, I. and Edwards, D.K., "Experimental Investigation of Natural Convection in Inclined Rectangular Regions of Differing Aspect Ratios", J. Heat Transfer, 98, 67, (1976).
75. Hollands, K.G.T., Unny, T.E., Raithby, G. and Konicek, L., "Free Convection Heat Transfer Across Inclined Air Layers", J. Heat Transfer, Trans. ASME, 98, 189, (1976).
76. McAdams, W.A., "Heat Transmission", Third Ed., McGraw-Hill, New York, 249, (1954).
77. Duffie, J.A. and Beckman, W.A., "Solar Energy Thermal Processes", Wiley-Interscience, New York, 120, (1974).
78. Kreith, F. and Kreider, J.F., "Principles of Solar Engineering", McGraw-Hill, New York, 203, (1978).
79. Lunde, P.J., "Solar Thermal Engineering", John Wiley, New York, 120, (1980).

80. Willier, A., "Design Factors Influencing Solar Collector Performance, Low Temp. Engineering Application of Solar Energy", Chapter 3, Technical Committee on Solar Energy Utilization of the ASHRAE, 35, (1966).
81. Watmuff, J.H., Charters, W.W.S. and Proctor, D., "Solar and Wind Induced External Coefficients for Solar Collectors", Comptes Rendus, 2, (1977).
82. Duffie, J.A. and Beckman, W.A., "Solar Engineering of Thermal Processes", John Wiley & Sons, New York, (1980).
83. Mitchell, J.W., "Heat Transfer From Spheres and Other Animal Forms", Biophysical J., 16, 561, (1976).
84. Lloyd, J.R. and Moran, W.P., "Natural Convection Adjacent to Horizontal Surface of Various Planforms", Trans. ASME; J. of Heat Transfer, 96, 443, (1974).
85. Ramsey, J.W. and Charmchi, M., "Variances in Solar Collector Performance Predictions Due to Different Methods of Evaluating Wind Heat Transfer Coefficients", J. Heat Transfer, Trans. ASME, 102, 766, (1980).
86. Sparrow, E.M. and Tien, K.K., "Forced Convection Heat Transfer at an Inclined Rectangular Plate", J. Heat Transfer, Trans. ASME, 99, 507, (1977).
87. Sparrow, E.M., Ramsey, J.W. and Mass, E.A., "Effect of Finite Width on Heat Transfer and Fluid Flow About An Inclined Rectangular Plate", J. Heat Transfer, Trans. ASME, 101, 199, (1979).
88. Tien, K.K., "Heat/Mass Transfer Characteristics and Fluid Flow Patterns for Air Flow About an Inclined and Yawed Flat Plate", Ph.D. Dissertation, University of Minnesota, (1978).
89. Stathopoulos, T., "Wind Pressure Loads on Flat Roofs", Master of Engineering Thesis, The University of Western Ontario, (1975).
90. Allen, P.L., "An Interferometric Technique for Studying the Coupling Between Free Convection Inside a Heated Enclosure and External Forced Convection", Master of Engineering Thesis, The University of Western Ontario, (1978).

91. Craze, P.J., "The Near Wake Behind a Circular Disc in a Smooth and Turbulent Airstream", Ph.D. Thesis, The University of Western Ontario, (1974).
92. Jenkins, F.A. and White, H.E., "Fundamentals of Optics", McGraw-Hill Book Company Inc., New York, (1957).
93. Eckert, E.R.G. and Goldstein, R.J., "Measurements in Heat Transfer", Hemisphere Publishing Co., (1976).
94. Tarasuk, J.D., "An Interferometric Study of Natural Convection During the Interaction of Surfaces of a Long Rectangular Block", Ph.D. Thesis in Mechanical Engineering, University of Saskatchewan, (1969).
95. Brown, D.R. and Tarasuk, J.D., "Design of an Inexpensive, 30 cm Diameter, Long Path Difference Interferometer", The Review of Scientific Instruments, Vol. 43, No. 7, (1972).
96. Brown, D.R., "An Inexpensive Long Path Difference Mach-Zehnder Interferometer", Master of Engineering, The University of Western Ontario, (1970).
97. Tarasuk, J.D., Snoek, C., Base, T.E. and Graham, L.E., "Heat Transfer from Air Supported Structure and the Associated Flow", IASS World Congress on Space Enclosures, Montreal, (July 1976).
98. Tarasuk, J.D., Base, T.E. and Snoek, C.W., "Heat Transfer Studies on Inflatable Structures", Engineering Institute of Canada, 87th Annual Congress, Montreal, (1973).
99. Tarasuk, J.D. and Snoek, C.W., "Heat Transfer Measurements on Inflatable Hemispherical Structure", Fifth Canadian Conference of Applied Mechanics, Fredericton, (1975).
100. Tarasuk, J.D., Snoek, C.W. and Graham, L.E., "Heat Transfer Studies on Inflatable Hemispherical Structure", SES Inc., 12th Annual Meeting, Austin, Texas, (1975).
101. Tarasuk, J.D., Snoek, C.D., "Heat Transfer from Inflatable Structure", ASME, Winter Annual Meeting, Houston, (ASME 75-WA-HT-97), (1975).

102. Snoek, C.D., "Heat Transfer from Inflatable Structures", Ph.D. Thesis, The University of Western Ontario, (1977).
103. Saidi, N.N., Tarasuk, J.D. and Base, T.E., "The Coupling Effect Between Natural Heat Convection, Inside the Cavity of a Solar Collector and External Forced Convection Heat Convection", ENERGEX 82, Canada's International Energy Exposition and Conference, Regina, (1982).
104. Graham, L., "Experimental and Analytical Studies of Thermally Coupled Flows", Ph.D. Thesis, The University of Western Ontario, (1982).
105. Hollands, K.G.T. and Konicek, L., "Experimental Study of the Stability of Differentially Heated Inclined Air Layers", Int. J. Heat Mass Transfer, 16, (1973).
106. Elsharbiny, S.M., "Heat Transfer by Natural Convection Across Vertical and Inclined Air Layers", Ph.D. Dissertation, The University of Waterloo, (1980).
107. Theory of Laminar Flows, Vol. 4, High Speed Aerodynamics and Jet Propulsions, (1964).
108. Table of Thermal Properties of Gases, U.S. Department of Commerce, National Bureau of Standards, Circular 564, (1955).
109. Handbook of Supersonic Aerodynamics, Bureau of Ordnance, Department of the Navy, Washington, D.C., Vol. 5, (1953).
110. Hauf, W. and Grigull, U., "Optical Methods in Heat Transfer", in Hartnett, J.P. and Irvine, T.F., Jr. (Eds.), "Advances in Heat Transfer", Academic Press, New York, Vol. 6, (1970).
111. International Critical Tables, McGraw-Hill Book Company, First Edition, New York, Vol. 7, (1930).
112. Carlson, W.D., "Interferometric Studies of Convective Flow Phenomena in Vertical, Plane Enclosed Air Layers", Ph.D. Thesis, University of Minnesota, (1956).
113. Flack, R.D., Jr., "Mach-Zehnder Interferometer Errors Resulting From Test Section Misalignment", Applied Optics, Vol. 17, No. 7, (1978).

END

1 | 6 | 0 | 9 | 8 | 3

FIN